Technische Universität München
TUM School of Engineering and Design

Optimization of Automotive Composite Structures for Crashworthiness

Simon Henk Hesse

Vollständiger Abdruck der von der TUM School of Engineering and Design der Technischen Universität München zur Erlangung des akademischen Grades eines

Doktors der Ingenieurwissenschaften (Dr.-Ing.)

genehmigten Dissertation.

Vorsitz: Prof. Dr.-Ing. Kai-Uwe Bletzinger

Prüfer*innen der Dissertation:

1. Prof. Dr.-Ing. habil. Fabian Duddeck
2. Prof. Dr. Chiara Bisagni

Die Dissertation wurde am 07.07.2021 bei der Technischen Universität München eingereicht und durch die TUM School of Engineering and Design am 10.11.2021 angenommen.

Optimization of Automotive Composite Structures for Crashworthiness

By

SIMON HENK HESSE

School of Engineering and Design
TECHNICAL UNIVERSITY OF MUNICH

A dissertation submitted to the Technical University of Munich in accordance with the requirements of the degree of DOKTORS DER INGENIEURWISSENSCHAFTEN (DR.-ING.) in the School of Engineering and Design

7TH JULY 2021

Abstract

Crashworthiness is one of the most important functions of a vehicle structure. It directly impacts the occupant safety and is therefore thoroughly tested by various governmental and independent institutions worldwide. A crashworthy vehicle means the structure needs to absorb the impact energy, therefore reducing the deceleration load on the occupants. Furthermore, due to environmental considerations and stringent emission legislation, vehicle emissions are becoming increasingly important. Vehicles need to get more economical by using less fuel and because of that the automotive industry currently prioritizes the development of Battery Electric Vehicles (BEVs). Batteries, however, take up permanent space and weight and require significant structural strength for safety reasons, which in turn requires more structural mass. Currently it is common to use metals for Body In White (BIW) and crash absorbing vehicle architectures. The increasing need for weight reduction and the importance of crash performance are a major design driver for using advanced composite materials. This material has shown to be lightweight, more robust an may have superior crash performance. However, the introduction of laminated composites into the design process of vehicle architectures, also introduces greater design complexity. Especially concerning the field of passive safety and the optimization for crash-worthiness.

This dissertation introduces a novel method to methodically handle different issues concerning the optimization of the crashworthiness of the structure. The proposed novel design work-flow addresses different aspect of the optimization process; shape optimization and complexity reduction. A two part method is introduced. The first part is concerned with the optimization of load paths, taking crash loads and composite crush behavior into consideration. Also the translation from 3D crash scenarios to 2D shape optimization domains and back is researched and a solution is presented. The second part introduces a complexity reduction work-flow that can be applied to the design from the first part.

The presented methods are applied on two distinct problems, relevant in the field of automotive crashworthiness. First is the optimization of the Carbon Fiber Reinforced Plastic (CFRP) composite support structure for the impact loaded front architecture of a novel vehicle design. Second is the optimization of a S-Rail before and after the complexity reduction. The results are promising. The results of the first application validate the proposed methods by generating functioning crashworthy composite structures. The second application example shows a significant increase in computational efficiency when optimizing the benchmark example after the complexity reduction is performed.

Dedication and Acknowledgments

I am indebted to my professor, Prof. Dr.-ing. habil Fabian Duddeck, who never lost faith and interest in me or my research. Our valuable discussions, his constructive criticisms, suggestions and guidance made this possible.

I am very thankful for my committee members Prof. Dr. Chiara Bisagni and Prof. Dr.-Ing. Kai-Uwe Bletzinger who saw the potential in my research, I am honored that they agreed to review my work.

I would also like to give my sincerest thanks to my supervisor, Dr. Dirk Lukaszewicz, who has always supported my work and provided me with direction and structure. Also, Dirk initiated this project and the research position at BMW and hired me for this position in the first place. So it is safe to say that Dirk is for a large part responsible for where I am today.

Of course I cannot forget to thank my colleagues from the Composites team in the Passive Safety department; Christian Boegle, Dr. Balaz Fodor, Jyrki Majamaeki and Lennart Keuthage. They provided me with vast amounts of insights and knowledge and helped close the gaps I had within the field of Crashworthiness and Composites.

Furthermore, I would like to sincerely thank Lukas Leidinger and Johannes Kremheller, who, during their internships, provided valuable help to bring essential methods within my research to practice.

A PhD Research without critical and helpful peers is impossible, therefore I owe my thanks to my PhD Colleagues at the time; Gerhard Steber, Marco Oxenbauer, Lailong Song, Volker Lange, Johannes Fender and Lavinia Graff.

A special thanks is reserved for Rainer Wuensch, my first chef and the person who hired me for my first position as engineer at BMW. In the final stages of my research, he was able to push me to finish. For the people who do not know me; this is not an easy feat.

Not to be underestimated is the support of my parents, Henny Hesse and Gemma Schrever. They where there for me every step of the way and always believed I could and would finish. Thank you mom and dad for always being there.

Many people supported my endeavor to undertake this research and stuck with me to its completion. Unfortunately I am bound to forget to name some of you. Know, however, that I am forever grateful.

Finally and most importantly I thank you, Mariam, for making this adventure possible. Without you I would not have achieved a fraction of where I am now. Your unending patience, support and love is what made this work, and so much more, possible.

Table of Contents

List of Tables

List of Figures

Figure **Page**

Acronyms

ANOVA Analysis of Variance.

BEM Boundary Element Method.

BEV Battery Electric Vehicle.

BIW Body In White.

CAD Computer-Aided Design.

CDM Continuum Damage Mechanics.

CFE Crush Force Efficiency.

CFL Courant-Friedrichs-Lewy.

CFRP Carbon Fiber Reinforced Plastic.

CLT Classical Laminate Theory.

CSRBF Compactly Supported Radial Basis Function.

CV Cross Validation.

CZM Cohesive Zone Modeling.

DE Differential Evolution.

DMS Direct Multi-Search.

DoE Design of Experiments.

ESL Equivalent Static Load.

FD Finite Difference.

FE Finite Element.

FEA Finite Element Analysis.

FEM Finite Element Method.

FRP Fiber Reinforced Plastic.

GA Genetic Algorithm.

HCA Hybrid Cellular Automaton.

ICE Internal Combustion Engine.

KKT Karush-Kuhn-Tucker.

LiSF Limit State Function.

LP Lamination Parameter.

LSE Level Set Equation.

LSF Level Set Function.

LSM Level Set Method.

MC Monte Carlo.

MCS Monte Carlo Sampling.

MMA Method of Moving Asymptotes.

MOPSO Multi-objective Particle Swarm Optimization.

NCAP New Car Assessment Program.

NHTSA National Highway Traffic Safety Administration.

OC Optimality Criteria.

ODE Ordinary Differential Equation.

PDE Partial Differential Equation.

PSM Physical Surrogate Model.

RBF Radial Basis Function.

RSA Response Surface Approximation.

RSM Response Surface Model.

RTF Random Tree Forest.

SA Sensitivity Analysis.

SDF Signed Distance Function.

SEA Specific Energy Absorption.

SIMP Solid Isotropic Material with Penalization.

SQP Sequential Quadratic Programming.

SSI Solution Space Identification.

SVM Support Vector Machine.

TDF Topology Description Function.

UNECE United Nations Economic Commission for Europe.

VCCT Virtual Crack Growth Technique.

X-FEM Extended-FEM.

CHAPTER 1

INTRODUCTION

It is well known that non-linear dynamic response optimization using a conventional optimization algorithm is fairly difficult and expensive for the gradient or non-gradient based optimization methods because many non-linear dynamic analyses are required. Therefore, it is quite difficult to find practical large scale examples with many design variables and constraints for non-linear dynamic response structural optimization. (Kim & Park, page 1 [61])

The quotation above points out a major challenge in many real world optimization problems. Take the design of crashworthy vehicle structures as an example [8, 41, 46, 92]. Designing for crashworthiness implies non-linear (geometric, contact, and material non-linearity) transient structural behavior subject to multiple load-cases and restricted by many implicit and explicit constraints, both geometrical and dynamic. Furthermore, optimization of non-linear and dynamic problems is computationally expensive, because of the time dependent properties and small time-increments needed to solve them. That is why these problems are rarely presented in their entirety in scientific literature. Crash problems are often broken down in manageable isolated tasks and solved for single or already less often for two load-cases.

This thesis does the same; a crash problem is significantly simplified and a work-flow is developed to methodically handle different issues concerning the optimization of the crash-worthiness of the structure. However, an added complexity is the introduction of advanced composite laminates as the main structural material. Also, the proposed work-

flow addresses different aspects of the optimization process, in particular complexity reduction and topology optimization.

This chapter starts with an introduction to the optimization of vehicle structures for crash-worthiness using advanced composites materials. Then, an overview of topology optimization using the Level Set Method is given. It is followed by an introduction to methods that are concerned with the reduction of problem complexity. The chapter is concluded with outlining the motivation for this research, defining the problem and proposing a novel set of methods and work-flow to solve it.

1.1 Optimization of advanced composite vehicle architectures

Due to environmental considerations and stringent emission legislation, vehicle emissions are becoming increasingly important. Vehicles need to get more economical by using less fuel and weight reduction of the BIW is one of the most efficient ways of doing that. For the same environmental reasons, the Battery Electric Vehicle (BEV) is rapidly becoming a popular alternative to its Internal Combustion Engine (ICE) counterpart. This causes the automotive industry to prioritize the development of BEVs. Batteries, however, take up permanent space and weight. The power density of batteries is significantly lower than that of the commonly used fossil fuels such as gasoline. Lithium-ion battery packs typically achieve around 0.864 MJ/kg (≈240 Wh/kg) [112], gasoline around 48 MJ/kg. Even when an ICE only achieves around 15% efficiency, and an electric motor 80%, the ICE is still a little over 10 times more efficient in terms of energy per kg. The consequence is that BEVs are significantly heavier compared to their ICE counterpart. Achieving an acceptable driving range with a BEV requires a significant increase in battery mass. This in turn requires a further increase in weight of the auxiliary BIW, due to increased requirements on stiffness and strength. This parasitic weight cycle is a major challenge and it directly increases the cost of the vehicle and reduces its efficiency. Therefore, reducing the weight of the BIW can significantly impact the total mass of a BEV, making it a worthwhile design driver.

Another important function of the BIW is to absorb the energy of the impact during a crash. Because occupant safety is regarded as one of the most important design drivers, it is extensively tested and assessed by various governmental and independent institutions world wide, such as the National Highway Traffic Safety Administration (NHTSA) and United Nations Economic Commission for Europe (UNECE), two major test programs are the Euro- and US-New Car Assessment Program (NCAP).

Currently it is common to use metals for BIW and crash absorbing vehicle architectures in the automotive industry. Their more or less isotropic nature, available extensive material databases and thoroughly researched elastic, plastic, and failure behavior make it a well understood material to design with [11]. Because metal components have been used in the automotive industry for more than 100 years, design methodologies, optimization work-flows and concept development are focused around the use of metallic (sub)structures.

The increasing need for weight reduction and the importance of crash performance

drive the research into new materials for vehicle design, such as, advanced laminated composite materials, specifically advanced Carbon Fiber Reinforced Plastics (CFRP). In automotive structures, these materials have a high potential; they have been shown to be lightweight, more robust and may have superior crash performance [21, 33]. Advanced CFRP composites that are being used today show typical Specific Energy Absorption (SEA) values between 60 to 70 kJ/kg [69], see Section 1.2 for a detailed explanation. Compared to commonly used metals, these values are two to three times higher. The high SEA together with the high specific strength and specific stiffness of advanced composites may have a significant influence on the overall weight reduction in automotive structures. However, the introduction of laminated composite materials into the design process of vehicle architectures, also generates greater design complexity. Especially concerning the fields of passive safety and optimization for crash-worthiness.

The optimization for crash-worthiness is a well-know and relatively broad topic in literature. Topics go from full vehicle optimization to research focused on local effects and optimization. Furthermore, topics present a variety of different methods; size optimization of structural members or shape or topology optimization of rough vehicle architectures or dynamically loaded sub-structures.

In contrast to crash-worthiness optimization with isotropic materials, such as several common types of metal, the optimization of advanced composite structures for crash-worthiness is a relatively rare topic. In the following some examples are given found in this research field.

Recently, Fang et al. [32] did a relatively extensive literature review on the state of the art on design optimization for structural crash-worthiness. They clustered their findings based on different topics; design criteria, crash-worthiness criteria, optimization strategies for size, shape and topology (single- & multi-objective, with/without uncertainties), and area of industrial application. They concluded based on their findings, among other aspects, that:

1. In most cases, surrogate modeling is the method of choice to approximate the response of a crash-worthiness problem. The main reason for this choice is to reduce the significant computational effort it requires to accurately calculate this response.

2. When optimizing a single component, its individual role as an integrated component within the vehicle architecture should be addressed and included into the optimization process. This will increase the overall performance of the component.

3. Novel structures and materials, such as advanced composites have been studied. However, only limited research is available. The existing literature only considers geometrical parameters as design parameters. It remains unclear if crashworthiness optimization can be used for problems with other material and process parameters; and from this viewpoint, composite structures have considerable room for advancement.

The available literature on optimization of advanced composite vehicle architectures is limited. The research focuses either on the shape optimization of crush or energy absorption performance of a single component or optimization of the laminate composition itself.

Lanzi et al. [66] used a Genetic Algorithm (GA) on a combination of explicit Finite Element Analysis (FEA) and a system of Radial Basis Functions (RBFs) to optimize the shape of a conical fiber-composite cylinder. The cylinder was subjected to vertical, 20° and 30° impacts, with three shape variables. The optimization objectives were to minimize cylinder weight and maximize the energy absorption. In essence, this means that Lanzi et al. optimized the SEA.

Zarei et al. [120] optimized the SEA of a square CFRP composite tube, using a sequential Response Surface Model (RSM) method work-flow. As variables the tube thickness, width and length were chosen.

Belingardi et al. [13] optimized the cross-sectional shape, wall thickness and transverse curvature of a bumper made of pultruded E-Glass. They achieved energy absorption comparable with steel components, however with better progressive failure mode and a reduced peak load.

Duan et al. [27] researched the influences of the thickness and radius on crashworthiness of a CFRP composite tape sinusoidal specimen. They considered the maximization of the SEA and minimization of the initial impact peak force as criteria for their optimization scheme.

More recently, Castro et al. and Fontana et al. [22, 35] optimized a CFRP composite impact attenuator for a formula student car. The attenuator is impacted perfectly axially by a rigid surface being perfectly clamped at the other end. After comparing it to different alternatives, they decided to use the FEA software Abaqus [2] in combination with CZONE [12] to calculate the structural response and simulate the progressive crushing of the specimen. They analyzed that this simulation set-up provides better and more robust results than other alternatives, such as Cohesive Zone Modeling (CZM). They split the attenuator into different zones, where every zone was allowed a different

layup design. Castro et al. optimized the layup for each zone for two objectives; minimize attenuator weight and maximize deceleration. Fontana et al. improved upon this by introducing a work-flow script that allowed for geometrical changes, such as variable curved walls and different zone lengths, as well as a variable layup design. They both used the Direct Multi-Search (DMS) optimization algorithm to handle the multi-objective design problem. They found designs that performed significantly better in terms of weight and acceleration than the previously implemented aluminum impact attenuator. The use of curved walls was concluded to be very import for both, better SEA and more robust designs.

All the research presented above regards examples of component optimization that represent either size or material optimization or a combination thereof. When looking for research that aims to optimize the overall shape or even topology of simple vehicle architectures with isotropic materials for crash-worthiness, less is found. Indeed, research containing the shape or topology optimization of composite vehicle architectures under crash loading conditions is even more scarce. Some examples of topology optimization for crash-worthiness with isotropic materials follow.

Early advances were made by Mayer et al. [72]. He and his colleagues devised a method using optimality criteria optimization method together with the homogenization technique to optimize the distribution of material in a 3D FE structure, in order to maximize the internal energy of the component. Non-linear elasto-plastic material was applied with an explicit Finite Element Method (FEM) to calculate the sensitivities and response of the structure. In order to constrain the solution, a maximum volume was defined. The idea is that by maximizing the internal energy, the energy absorption of the structure is improved as well. Energy absorption in an impact scenario is a time dependent problem. Mayer et al. incorporated this time dependency by modifying the objective function to a summation of weighted objective functions at specified times. They applied the method on a rear S-Rail of a typical car and found that they could improve the energy absorption of the initial design. A downside of the proposed method is that the final structure is very similar to the initial structure in shape and size, with the addition of 'holes'.

Pedersen [86] went a different route to solve topology optimization for non-linear time dependent problems. He first proposed a method to optimize a certain initial two-dimensional frame structures, called ground structure. He used beam elements with plastic hinges with a formulation that allowed for large rotations. The objective was to minimize the error between a prescribed single nodal force-displacement diagram

and the actual response at that node. A quasi-static FEA was developed to calculate the response of the frame structure. The height of each element was considered as the variable, which is similarly done in the element material density method. By using this setup, the sensitivity could be calculated analytically and a mathematical programming method could be used as the optimization algorithm, in this case the Method of Moving Asymptotes (MMA). Results showed frame structures that came close to the desired load-displacement requirement, although measures needed to be implemented to mitigate collapse modes. Pedersen improved on this method in further research [87, 88]. He implemented for example methods to optimize crash-worthiness, by defining an acceleration over displacement or time as the objective, constrained by structure weight and optionally maximum displacement. An example of a largely simplified 2-D vehicle front-end showed the ability of the method to match the required deceleration over displacement very accurately. One downside of the method proposed by Pedersen is that only his developed beam elements can be used, meaning only isotropic materials can be modeled. A positive aspect is the ability of the method to actually do full-scale topology optimization of non-linear problems, thereby finding possible new and better optimal load paths.

Ortmann et al. [77] devised a graph and heuristic based approach to optimize the topology of crash loaded structures. Their method is comprised of two different optimization loops. The outer loop controls the design space, defined by the outer topology and shape of the structure. The inner loop performs the shape and size optimization. The method is a frame-work, allowing for the connection to commercially available FEA and optimization software. Heuristic rules derived from expert knowledge use the results of FE simulations like velocities or energies to alter the topology of the structure. Currently, their method can only optimize a 2-D topological design of cross-sections, although the structural response to be optimized can come from a 3-D structure. Their method is therefore an interesting example of a method where the topology optimization takes place in 2-D, to increase the performance of the 3-D representation. Thereby decreasing the problem complexity.

Patel et al. [84, 85] based their method for topology optimization for crash loaded structures on the Hybrid Cellular Automaton (HCA) method. They introduced a heuristic and non-gradient method for continuum-based topology optimization method. The HCA method is used to generate 3-D solid structural design concepts. Their goal was to maximize the energy absorption of the structure whilst constraining the maximum intrusion of the impacting element. They achieved this by using the material update

rule within the HCA framework to distribute the internal energy throughout the entire structure. Therefore, the result is in a certain way similar to a fully-stressed design. The method starts with an explicit FEA to get the stress-strain states of all elements in a crash scenario. The HCA method is used to update the material distribution by changing the element densities. Convergence is tested and if not reached, the loop starts again at the FEA. Their method has the benefit of being able to do 3-D continuous topology optimization for crash-worthiness. However, only solid structures can be designed by the current implementation. Furthermore, the method only works for material that dissipates energy by plastic deformation and strain hardening. To the knowledge of the author of this thesis, failure criteria were not yet considered for this approach.

Duddeck et al., Hunkeler and Zeng et al. [28, 50, 121, 122] improved on the research by Patel et al. They proposed an approach based on HCA for crashworthiness topology optimization with a special focus on thin-walled structures. First, they developed a two stage method for the optimization of cross-sections for thin-walled beam-like super structures. In further research by Zeng et al. [122] they extended the method to 3D thin-walled beam-like structures. To validate their method, they optimized well-known 3D bending problems for minimal intrusion.

The shape and topology optimization methods proposed above for crash-worthiness, introduced approaches that should overcome some of the difficulties that are intrinsic to this field of problems. Examples being the complicated deformation conditions, large number of design variables, bifurcations within the structure and complex sensitivity calculation. Most methods however rely on the dissipation of energy by plastic deformation and thus require metallic materials. The method proposed by Ortmann et al. could in theory be applied to other materials, however this is not yet pursued. A method to optimize the load-paths of a structure to increase crash-worthiness via topology optimization using composite materials could not be found in literature. Furthermore, what is not discussed in these papers but what can be considered a downside of the ‘classic’ topology optimization, is that often thin-membered ‘truss’ structures are generated. For metallic structures this may be a plausible and desired design direction. For composite structures however, this is not optimal. The ability to have a larger control over the shape evolution can be considered beneficial.

Another approach besides the commonly used homogenization or Solid Isotropic Material with Penalization (SIMP) method is the Level Set Method (LSM). The LSM allows for larger control over the design evolution during optimization. The LSM is a relatively unknown concept in comparison to SIMP method, therefore an introduction to

the method and its benefits is given in Section 1.3.

Research on the LSM for shape & topology optimization is plentiful. However, the implementation of the LSM within a optimization work-flow for crash-worthiness is not plentiful. Bujny et al. [18, 19, 90, 119] did various research on solving dynamic crash problems with the LSM. They proposed a topology optimization approach based on evolutionary algorithms and a low-dimensional level-set representation; EA-LSM. This method allows for an optimization of arbitrary quantifiable criteria using high-fidelity explicit crash simulations. They solved various well known linear elastic static problems, showing the potential of the method. However, the main goal was to use EA-LSM to solve nonlinear crash cases. To validate the usefulness of their methods, they applied it to optimize the frequently studied 2D and 3D bending problem for minimization of the intrusion. The method proved to be as good or slightly better than HCA. Finally they applied their optimization work-flow to optimize a 3D-printed metal joint in a hybrid S-rail structure, with good results. In theory, this method can be applied to all problems including highly non-linear crash load cases. One of the practical difficulties is the handling of higher number of variables, which is especially for composite optimization important.

1.2 Mechanics of advanced composites under impact

The primary reason of choosing advanced composite materials for use in crash-absorbing structures is the relatively low weight with respect to the amount of energy that can be absorbed from an impact. Therefore, before the theory behind the energy absorption mechanics of composites is explained, the method of measure for energy absorption efficiency should be explained. With these metrics the performance can be objectively compared between different structures and materials.

There are two popular metrics available; Specific Energy Absorption (SEA) and Crush Force Efficiency (CFE) [69]. The SEA is calculated as follows:

$$\mathrm{SEA} = \frac{W}{\rho A s} = \frac{\int_0^s F \mathrm{d}\delta}{\rho A s} \tag{1.1}$$

where W is the total absorbed energy by the specimen, ρ is the mass density of the material, A is the cross-sectional area, s is the total displacement of the impactor into the specimen or crush distance, δ the crush distance variable and F is the crush force. Commonly, the mean force during the crushing phase is taken as the crush force F, shown in Figure 1.1 as $\overline{P}$.

The CFE is the ratio of the maximum force, or peak force, F_{peak}, and the mean force F. An example of the peak force F_{peak} is shown in Figure 1.1 as P_{max}. The CFE is calculated as follows:

$$\mathrm{CFE} = \frac{F_{\mathrm{mean}}}{F_{\mathrm{peak}}}. \tag{1.2}$$

The CFE gives a measure of the efficiency of the structure to go into its main energy absorption mode. The initiation phase as shown in Figure 1.1 shows the initial force required by the structure before the absorption phase can occur. If the force peak is equal to or only slightly higher than F_{mean}, the CFE equals 1. This is a desirable property, as it means the auxiliary or supporting structures behind the crush-members do not be overly strong, requiring more material and thus mass. It also means the crash-member itself needs less material or has a lower risk of going into a undesired buckling mode. The peak force is in most cases the result of the elastic properties of the structure before fracture and can be influenced by implementing a crush-trigger in the design of the member. The next part will explain this further.

The mechanics behind energy absorption with advanced composites is significantly different than that of metals. Metals dissipate a large part of the impact energy by plastic deformation. Take for example a steel cylinder, or a similar closed cross-sectional tubular structure, that is impacted in axial direction by a flat rigid surface. With sufficient

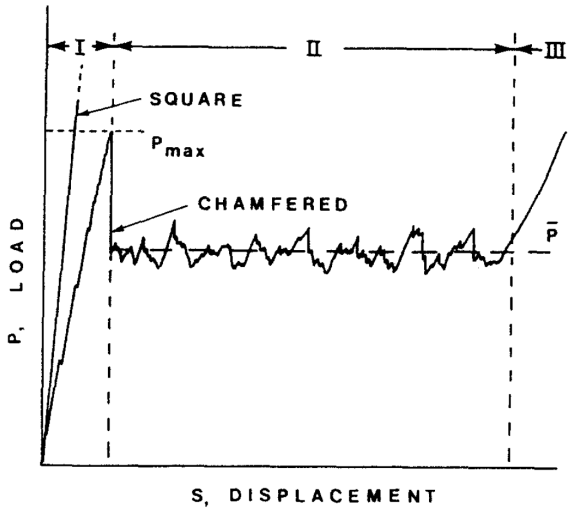

FIGURE 1.1. Typical load-displacement curve of a CFRP composite tube undergoing progressive crushing under impact. I: Crush initiation and formation of the crush-zone, II: Absorption or progressive crushing phase, III: End of material or compaction of debris. [49]

load and under ideal conditions, the cylinder will buckle and fold unto itself, see Figure 1.2. The formation of these folds requires local plastic deformation of the steel, thereby dissipating the impact energy. More specifically, the energy is dissipated through plastic folding, work hardening and adiabatic losses during heating [69]. In stark contrast to metallic structures, advanced composite materials dissipate the impact energy through extra- and intra-laminar friction, fiber bending and fragmentation of the laminate [57, 69]. The process behind the energy absorption mechanics of metals and advanced composite structures can be divided into four categories [49]:

- Global buckling
- Progressive folding
- Progressive crushing
  - Progressive splaying
  - Progressive fragmentation

Generally, the first mode of deformation, global buckling, absorbs very little energy and is therefore unwanted for energy absorption purposes. This mode of deformation can also be

FIGURE 1.2. Typical example of progressive plastic folding in a metallic specimen [69].

easily avoided by choosing appropriate structural dimensions. Progressive folding is the common mode of deformation for metallic structures with crash application, as described above. However, it can also occur in structures made of ductile Fiber Reinforced Plastic (FRP) and metal/FRP hybrid materials. The SEA of crash-members that primarily show progressive folding can reach intermediate values; SEA average between 15 and 30 kJ/kg. They do not, however, reach the higher levels that progressive crushing can achieve, because they lack the extra mechanisms for energy dissipation [69]. Progressive crushing shows the highest values for SEA and is commonly seen in advanced composite materials such as CFRP. This mode of deformation consists of a “front” of individual layers in a laminate that permanently deform in crushing. During the progressive crushing a stable crush zone is formed that initiates at the point of contact and progresses down the structure with the impacting element, away from the point of initial contact.

Progressive crushing can consist of splaying or fragmentation or a combination of both modes. Splaying is generated by a wedge made of debris from the initial impact. This wedge is pushed through the layers of the laminate of the specimen, causing a combination of failure modes, one of which is intralaminar shear cracking. The separate layers that have a mainly longitudinal fiber direction splay in- and outward. The dominant

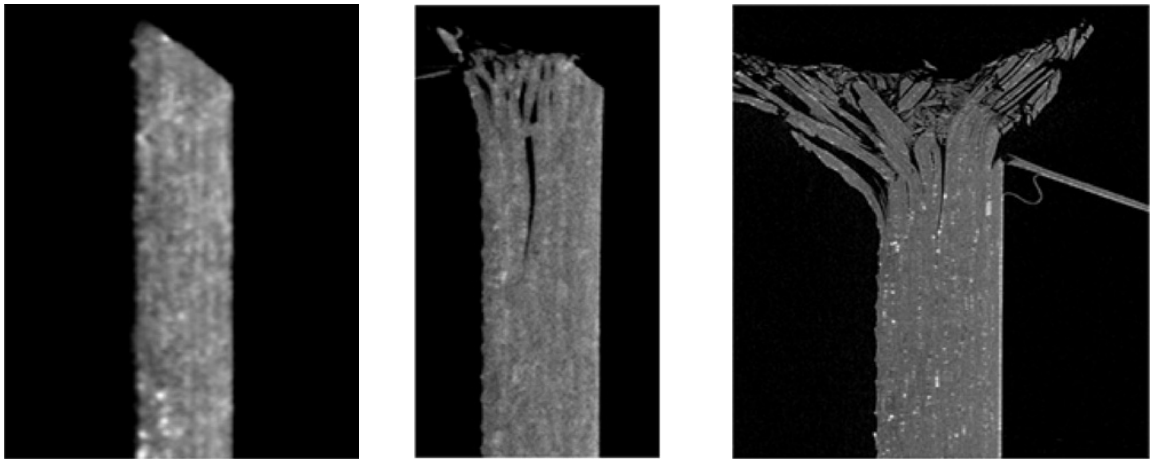

(a) Crush initiation and forming of initial cracks and material debris.

(b) Material debris forms a wedge, initiating laminae bending and fracture in the front.

(c) Fully established crush zone, propagating downward.

FIGURE 1.3. Example of the forming of a crush zone in an advanced composite specimen [57].

failure modes are laminar tension, compression and shear fraction, and interlaminar fracture in tension and shear. The precise combination of these failure modes is highly dependent on the design and composition of the composite laminate.

Progressive fragmentation is recognizable by the forming of fragments in the crush zone that are forced inside and outside of the specimen. These fragments are relatively small and have typical shapes. Hull [49] showed that the formation of either splaying or fragmentation in the crush zone is a result of the competition between different microfracture mechanisms. Fragmentation is critically dependent on the shear failure process, thus if splaying does not occur the stresses in the crush zone build up. If a certain critical shear fracture stress value is reached, fragmentation occurs. This means the crush load depends on laminate configuration, elastic properties and failure strengths of the individual laminae. Figure 1.3 shows an example of the initiation and progression of a crush zone in a composite specimen with a dominant fragmentation mode.

The combination of several failure modes in a relatively large percentage of the specimen's volume is the reason that progressive crushing can consume such a high amount of energy per unit weight. An overview of SEA from literature for typical advanced composite specimens with different fiber materials is given in Figure 1.4.

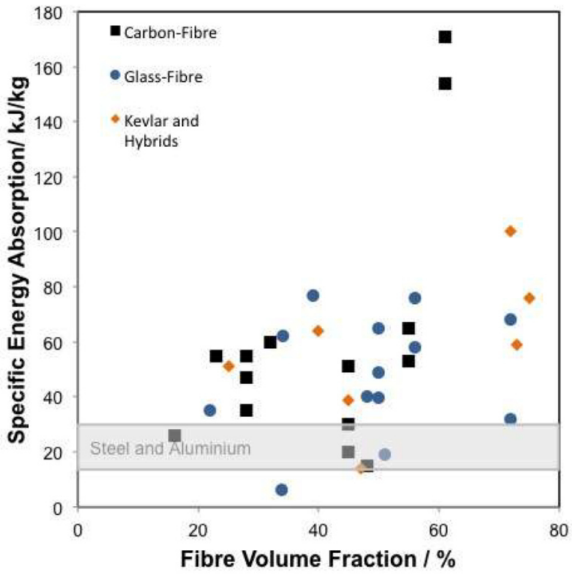

FIGURE 1.4. An overview of SEA values from literature for typical advanced composite specimens with different fiber materials. The typical range of SEA for metallic structures is given for comparison [69].

1.3 Level Set Method for Topology Optimization

It was explained in Section 1.1 that in the field of topology optimization, the density based methods, like the SIMP method, are the popular choice. However, recently the LSM was adapted to use as a method in topology optimization. Sethian and Wiegmann [94] first did research in this direction. They used the versatility of the LSM and developed a structural optimization method based on the LSM. In their approach they combined level set and finite difference techniques for constructing designs subject to certain design constraints. Using ad-hoc criteria based on the von-Mises stress, an initial design is evolutionarily updated by adding material at high stress areas around the boundary and removing material al low stress areas. The boundaries in the design domain, described by the Level Set Equation (LSE), are moved by a velocity function based on these ad-hoc criteria. This method does not rely on shape sensitivity analysis.

The Level Set Method (LSM) is a method for describing an $N-1$ dimensional surface in an N dimensional space. The zero level contour of a Level Set Function defines the boundary of the surface. The inside and outside definitions of the surface are defined by the sign of the LSF. Osher and Sethian [78] first developed this method to follow surface boundaries propagating with curvature-dependent speed. The surface boundary can be moved over time by solving a variant of the Hamilton-Jacobi Partial Differential Equation (PDE). In this context, this equation is also called the LSE. By using an appropriate normal velocity, the boundary is moved normal to the interface. One of the advantages of the LSM is the ability to depict all variety of shapes in all dimensions with large control over the geometrical properties during the surface chance over time, such as the amount of curvature. Secondly the LSM allows for natural topological merging and breaking of surface boundaries. The LSM found a broad application in different areas, because of its versatility and computational efficiency. Areas of application are among others, fluid mechanics, phase transitions, image processing and solid modeling in Computer-Aided Design (CAD).

Level set based topology optimization using sensitivity analysis was first introduced by Osher and Santosa [79]. They used the LSM to optimize a two-phase mass distribution over a drum with constant tension. The shape sensitivity of this two-phase mass distribution was used as the normal velocity of the boundary. The LSF was updated by solving the LSE with an upwind numerical Finite Difference (FD) scheme.

Both Allaire et al. [6, 7] and Wang et al. [109] independently developed a generalized structural optimization method based on the level-set framework and classical shape

sensitivity analysis. Their method is considered a combination of the developments mentioned before and made the LSM more generally applicable to a wider range of structural optimization problems by coupling the method with FEM. Wang et al. and Allaire et al. used the upwind scheme to solve the LSE and move the boundary. The velocity field was determined by deriving the shape derivatives of a Lagrangian, used to transform the constrained into an unconstrained optimization problem. The structural performance of the intermediate solutions was assessed by the FEM. They both used the "ersatz material" approach to map the level set domains onto an FE based discretization. However Wang et al. used a relaxed Heaviside approach, whereas Allaire et al. interpolated the boundary to determine the element volume fraction occupied by the level set material domain. They both solved a selection of typical optimization problems, for example compliance minimization, confirming the potential of the LSM for structural optimization.

The LSM based structural topology optimization as presented by Allaire and Wang shows in essence a significant similarity to other, more common, density based methods, such as the SIMP method. Both depend heavily on the FE discretization and FEM for the calculation of the shape sensitivities and the level of geometrical detail for numerical simulation of the structure. However, whereas for the SIMP method the geometrical detail is based on the FE grid, the LSM can describe the geometry continuously. Furthermore, because of the LSE, more properties of the surface boundary and geometry can be controlled, such as the level of curvature and the (for 2D) nucleation of topological changes. The moving boundary property of the LSM therefore provides interesting control possibilities. Downside of the method in comparison to SIMP, is the larger number of problem specific parameters involved with the optimization. Curvature control is necessary to avoid artifacts in boundary shape, but can reduce convergence speed and optimality. The solution of the second order PDE LSE is an extra complicating step.

Another property that can be considered a downside, is that the choice of optimization algorithms is limited. Almost always a variant of the indirect search method with the steepest-descent approach based on the Optimality Criteria (OC) is used [7, 109, 114]. The direct search method starts with an estimate and searches the design space for optimum points, iteratively improving the design until the OC are satisfied [8], where the OC are the conditions a function must satisfy at its minimum point [8] (e.g. Karush-Kuhn-Tucker (KKT) conditions). Algorithms that try to find solutions to these conditions are often called OC or indirect methods.

The LSMs introduced above rely on solving the Hamilton-Jacobi equation, or LSE,

to advance the level set boundary. Computationally expensive numerical techniques, such as the upwind scheme, are necessary to accomplish this task. Without modification, this application is unable to nucleate new material boundaries, which many consider a downside. The latter problem was solved by Allaire et al. [4] with the introduction of a topological derivative, based on previous research by Eschenauer and Schumacher [31, 93]. In principle, their method operates by nucleating very small new boundaries if the topological gradient for decreasing an objective function matches certain minimal requirements.

Direct search methods, such as Sequential Quadratic Programming (SQP) and MMA [80], work well when the response functions are explicit functions of the design variables, such as the element densities in the SIMP method. However, the behavior of the response functions as a function of the level set variables is often very different. The reason is the non-linear relation between the LSF and the material domain [106]. The Hamilton-Jacobi PDE or LSE are both space and time dependent, with a velocity component driving the evolution of the equation. By introducing a pseudo-time component, the normal velocity of the level set boundary can be related to the shape derivative of the material domain. However, this relation is implicit in nature and leaves indirect search methods as the favorable method for conventional LSMs.

A significant downside of the indirect OC method is the difficulty to include multiple design constraints. The sensitivities collected in the sensitivity field over the design domain can be used directly to construct the Hamilton-Jacobi velocity field. If design constraints are introduced, the constrained optimization problem needs to be transformed into an unconstrained one. The popular choices are penalty or augmented Lagrange multiplier formulations. Classically, the use of these methods has difficulty handling a large number of design constraints. The penalty method was implemented by Allaire et al. [4, 7]. They referred to the penalty factor as a fixed Lagrange multiplier. However, this method is unable to enforce the constraints exactly and therefore requires trial and error for setting the desired penalty factor. The augmented Lagrange multiplier method is considerably more popular, mainly due to its ability to converge to good optima while matching constraints values exactly. Furthermore, it can be shown that the augmented Lagrange method converges faster than commonly used penalty methods [8]. It is well-known for its numerical stability. Different variants of the method were used by Challis [23], Luo et al. [70], van Dijk et al. [106] and Otomori et al. [81].

An alternative to solving the Hamilton-Jacobi equation for boundary propagation, is available by using a so-called parameterized LSM. Early developments on this idea were

done by Ruiter and van Keulen [25]. They used a Topology Description Function (TDF) with a cut-off plane to describe the geometry within a design domain, very similar to the LSF description. The design variables of the TDF are parameters that determine a function on the design domain, the performance of the design is determined by applying the FEM. The difference with the common LSM is that with the parameterized approach, the geometry description is entirely decoupled from the finite element discretization. To update the LSF with the conventional LSMs, the Hamilton-Jacobi equation is solved. Parameterization of the LSF allows the Hamilton-Jacobi equation to be discretized into a system of mathematically more convenient coupled Ordinary Differential Equations (ODEs). This means, the sensitivities can be determined explicitly and a larger variety of optimization algorithms can be applied, e.g., stochastic methods such as genetic algorithms [24] or mathematical programming such as the MMA method [80]. Appropriate basis functions for the TDF are required. Popular choices are RBFs [25, 110] and Compactly Supported Radial Basis Functions (CSRBFs) [70]. The parameterized approach to the level set based topology optimization shows promising results. However, the type of parameterization and the number of parameters influence the maximum level of detail of the material boundary that can be represented.

1.4 Complexity Reduction Methods

The introduction of advanced composite materials into the design of automotive structures increases the complexity of the already complex design development. This section focuses on three major factors increasing this design complexity; parameters, mechanical behavior and computational cost, listed below.

Parameters The number of design parameters plays a large role in the complexity of structural design. They can describe both the geometry and material configuration of a component or structure. Typical geometry parameters are for example: size and shape of the cross-section and length of structural members. Material parameters can be: thickness of certain composite laminates, material properties such as Young's modulus and mass density of matrix and fiber materials, composite laminate layup design and stacking sequence. For real structures, the amount of design parameters can increase rapidly. This is especially the case when advanced or laminated composites are used.

Mechanical behavior Stiffness, deformation modes and complex structural interaction of a design are examples of mechanical behavior. The energy absorbing characteristics of a vehicle structure and the required deformation resistance of the safety cell are primarily defined by the stiffness and failure modes of a structure. Together with the geometric design of the structure, they form the basis of the crash performance. Metallic crash structures absorb energy in crash principally by plastic deformation, work hardening and partially by failure. The primary energy absorption mechanism in advanced composite structures is by fragmentation of the material in the impact zone [57]. Ideally the composite material is completely destroyed for maximum impact energy dissipation. In addition and in contrast to metals, laminated composites go through a higher number of often more distinctive failure modes than metals [21, 53, 71]. The nonlinear and discontinuous character of the failure mechanisms and process contributes to the functional complexity of the structure. Due to the failure properties of laminated composites and significant lack of plasticity, the failure and collapse of the structure can happen suddenly. The result is that for small variations in design parameter values, the change of the structural response can be relatively large. This is especially the case when compared to metallic structures. This failure behavior of advanced laminated composites can be described as not robust and increases the complexity of designing CFRP components and structures.

Computational cost Transient dynamic analysis methods are often used for the accurate simulation of impact or crash events, for example with the explicit FEM.

However, these methods are notably computationally expensive. This is limiting the efficiency when evaluating different design concepts. The introduction of laminated composite materials increases the material complexity and can therefore increase the computational effort required even more. The increase in simulation time will reduce the number of design concepts that can be evaluated and therefore restricts the number of possible iterations.

The goal is to increase the efficiency in the design process for vehicle crash-worthiness with advanced composite materials. In order to achieve this, some of the complexity increasing factors discussed above should be reduced. In the following sections some of the methods that are proposed to achieve this are introduced.

1.4.1 Sensitivity Analysis & Parameter Importance Hierarchy

In the previous section, the great amount of parameters in the design process was established as one of the main complexing factors. And indeed, to limit the complexity of the problem, commonly a choice is made to limit the number of parameters at the start of the design. Complexity increases with more design parameters. Especially with strong non-linear crash problems, engineers often choose to limit the design parameter count [27, 48, 66]. A downside of limiting the design variables at the start is that the engineer can lose a significant part of the design space, where interesting and relevant design optima could present themselves. One approach to methodically limit the design parameters, is to apply a Sensitivity Analysis (SA). The SA of the output of a model aims to quantify the relative importance of each model input parameter in determining the value of an assigned output variable [47]. With this information, a parameter importance hierarchy can be established by deriving the parameter importance factors. This hierarchy can help the engineer to make a calculated choice in variables out of a larger set of parameters, while arguably keeping the loss of valuable design space to a minimum.

Customarily methods of SA are classified into two categories [102]; local and global SA. Local SA focuses on the local influence of a parameter value change on the system. This sensitivity is calculated by taking the gradient of the response with respect to its parameter around a nominal value. This gradient can be derived in different manners, among others; finite difference schemes, direct differentiation or adjoint methods [20]. Local sensitivities are often used for mathematical optimization. An example of this are the shape sensitivities for structural optimization methods, such as shape and topology optimization [7, 96, 109].

Global SA aims to derive the influence of the input parameters (independently or in combination) on the output for the entire design space. Therefore, it is more suited in the derivation of a parameter hierarchy. Methods for performing a global SA can generally be divided into two groups [102]:

1. regression-based methods, such as the Pearson or Spearman correlation coefficient;

2. variance-based methods, such as the linear or quadratic Analysis of Variance (ANOVA) and Sobol indices [97].

Regression-based methods only provide accurate importance information when the model is linear (Pearson) or monotonic (Spearman). In case of non-linearity and non-monotonicity, they fail to represent the response sensitivities; then variance-based methods are a better choice. Yet, the variance-based methods require a relative large sample count to compute. In case of computationally expensive models, an RSM is usually derived on which the variances are computed [27, 48, 66, 102].

An interesting implementation of sensitivity analysis on a vehicle crash scenario can be found in Bojanowski et al. [15]. They investigated two impact scenarios on a transit bus; side impact and roll-over. They applied two different sensitivity analysis methods, Analysis of Variance (ANOVA) and Sobol analysis, to identify the most relevant structural elements that contributed to the strength of the bus frame. These identified parameters were used in an optimization using multi-objective GA. The goal was to find an optimum configuration and increase the crash-worthiness of the bus while minimizing its weight. Bojanowski et al. used sequentially updated RSMs with Radial Basis Function (RBF) in the GA approach. The RSMs were also used for the sensitivity analysis. Results showed that the sensitivity analysis was capable of clearly identifying the most influential parameters. Unfortunately, no conclusion was given on which type of sensitivity analysis performed better.

In a research by Reuter et al. [91], they compared three different sensitivity analysis techniques on a non-linear structure model; Pearson, linear ANOVA and Sobol. They conclude that only the Sobol indices are able to identify the relevant input variables for non-linear and non-monotonic problems.

It seems that the Sobol indices provide a robust method for the derivation of the influence factors in non-linear models, taking into account the effect of parameter combinations or higher order effects on the response [9, 47].

1.4.2 Surrogate Modeling

Surrogate models are techniques to approximate the outcomes of interest of certain systems. Often an outcome of interest cannot be easily measured, so a surrogate model is used instead. As explained before, in the case of determining the crash response of a structure, simulation methods such as Explicit FEM are used. However, depending on the problem, a single purpose built vehicle crash simulation can take more than 24 hours to complete on an advanced processing cluster. A method to alleviate this efficiency problem is by making a surrogate model. This model then approximates selected outcomes as closely as possible, but is computationally significantly cheaper. Surrogate models are constructed using data from the system or simulation of interest. They are based on modeling the response of the detailed FE model to a limited number of intelligently chosen data points, determined by some Design of Experiments (DoE). This method of construction is a bottom-up approach. The inner workings of the system or simulation of interest does not need to be known, it is considered a so-called Black-Box, only the input/output behavior is assessed.

Surrogate models are sometimes also referred to as meta-models or RSM. There are different approaches to construct an RSM. Among the large field of approaches, three popular techniques are [36]:

1. polynomial regression analysis (such as linear or quadratic regression);
2. interpolative methods (such as Kriging);
3. supervised learning models, such as RBF networks, Random Tree Forest (RTF), SVM and artificial neural networks.

Not every technique is suitable for accurately modeling the response of a crash simulation. The transient dynamic, non-linear and discontinuous property of a structural impact is hard to approximate. Techniques, such as the regression based analysis, make prognosis based on continuous and often linear approximation between sample points and cannot capture the complete behavior of the simulation. However, by choosing an adequate approximation technique, the RSM method is suitable for modeling non-linear problems.

The Response Surface Approximation (RSA) is derived from the RSM technique and is computationally inexpensive to evaluate and usable for non-linear design problems. Therefore, this is often used in structural optimization for crash [10, 37, 43, 113]. Optimization is applied either directly on the RSA or done by successively updating the RSA [98].

The RSM technique is also a popular method for crash performance optimization of composite structures. Hou et al. [48] used the RSM with quadratic polynomials as basis functions to approximate the SEA and peak force of axial impacted FRP composite tape sinusoidal specimens. In their research two input variables are applied; the ply and wave count. With these they change the laminate thickness and segment radius of the specimen. They then used multi-objective genetic algorithms to minimize the peak force and maximize the SEA. The results showed that their applied method was able to produce good results. Duan et al. [27] proposed a resembling approach to optimize the SEA and peak force of tapered composite tubes. However, instead they used the Multi-objective Particle Swarm Optimization (MOPSO) method for their optimization algorithm. Lanzi et al. [66] performed a study on tapered composite cylinders under axial impact. They optimized the structure for high energy absorption and minimal weight. As input variables they chose three shape parameters: lower edge major axis, lower edge eccentricity and taper ratio. They used a combination of RSM with RBF and a multi-objective GA to approach the optimization problem. They also considered different impact angles.

The biggest benefit of the surrogate modeling technique with RSM is the increased computational efficiency and, with the right approach, its capability to approximate non-linear responses. However, a significant downside is the large dependency on the type of DoE and the amount of samples used to construct the RSM. It is clear that other researchers have used surrogate modeling to simplify the structural design problems for crash, especially in an optimization framework. For composite structures, the surrogate modeling technique proved useful, but no design problems were assessed where the structural stability was part of the problem design space. It can be concluded that it is common to only use a limited number of design variables in crash optimization. Furthermore the variables are bounded such that structural instability is mitigated, simplifying the design optimization problem.

1.5 Motivation

This chapter describes that, because of increased environmental concerns and higher safety standards from both social and governmental perspectives, vehicles need to lose weight and at the same time provide increasing safety standards for the occupants. Towards that goal, this chapter showed the methods and theories from literature that give an overview of the state-of-the-art on the crash-worthiness optimization of vehicles components, structures and architecture, the optimization of fiber composite components under impact and the energy absorption mechanics of composite materials. Many authors in this field indicated the increased complexity in terms of design variables and computational requirements as a significant challenge. This complexity only increases further when including fiber composites as a material choice. The introduction therefore also summarized state-of-the-art methods to address the issue of complexity.

It can be concluded that many advances in this field have been made, however no methods on the shape or topology optimization of crash-worthy composite structures could be found. This is a relatively empty research field and the author believes progress can be made here.

In the case of optimization problems where the crash performance is considered as the objective, the preferred method is a selection of RSM techniques, used to approximate the responses. Nonetheless, the parameter space is significantly limited in these cases. At present the larger part of research goes into solving specific optimization problems, mitigating a large part of the design complexity by simplifying the problem at the start. Furthermore, the derived RSM is only accurate if the structure is assumed stable, i.e. no collapse. As a consequence the RSM technique becomes less useful when the structural stability is part of the problem's design space.

Generally, global sensitivity methods are applied to collect information on the parameter space and to reduce the number of parameters. Still, also here, no attempt is made to differentiate between the structure's failure modes, i.e. stable or unstable behaviors. This raises the question whether there is a more efficient manner to reduce complexity for the design of composite components with respect to crash, one which can be used in an industrial product development.

This dissertation presents novel methods to handle the specific issues of shape optimization with relevance to 3-D composite designs and the reduction of optimization problem complexity. Thereby adding new insights in this new field of optimization of crash-worthy composite vehicle architectures. A design optimization work-flow using

shape optimization is suggested for 3-D early phase composite architectures subjected to multiple load-cases. Furthermore, a method is presented that reduces the complexity of the subsequent size optimization problem.

CHAPTER 2

BACKGROUND THEORY

This chapter explains some of the methods, theories and algorithms that are used in this research. First, the algorithm of the Level Set Method (LSM) as it is implemented in this research is explained. Then, the Classical Laminate Theory (CLT) is summarized and used to introduce the theory behind Lamination Parameters (LPs). Finally, the methods used to simulate advanced composites in crash are introduced.

2.1 Level Set Method for Topology Optimization

The content of this section was partially published by the author in the journal Structural and Multidisciplinary Optimization [45]

In this section, the principles behind the Level Set Method (LSM) are explained. For a more thorough explanation of the method, the reader is referred to works by [7, 107, 109].

Let D be a bounded reference domain and ∂D is the corresponding boundary of D. Then, Ω is a domain filled with solid material within D, such that $\Omega \subset D$. The complementary domain representing a void that exists, i.e. a void domain is then expressed as $D \backslash \Omega$. In the level set framework, the material domain or design boundary $\partial\Omega$ is embedded implicitly as the zero level set of a one-dimensional-higher level set function $\phi(\vec{x})$, where $\vec{x}$ stands for a position within D. Each part in the design domain is then defined as follows:

$$\begin{aligned} \phi(\vec{x}) < 0 \quad \forall \quad \vec{x} \in \Omega \backslash (\partial\Omega \backslash \partial D); \\ \phi(\vec{x}) = 0 \quad \forall \quad \vec{x} \in \partial\Omega \backslash \partial D; \\ \phi(\vec{x}) > 0 \quad \forall \quad \vec{x} \in D \backslash \Omega. \end{aligned} \tag{2.1}$$

With the level set function as presented in Equation (2.1), any design of any topology of any dimension of the material domain Ω can be represented within the reference domain D. Commonly only two- and three-dimensional designs are considered when applying the LSM, for clarification the two-dimensional case is considered here to explain the method. In the definition from Equation (2.1); $\phi > 0$, represents a void domain, $\phi < 0$ represents a material domain and $\phi = 0$ represents the design boundary. The different material states are depicted in Figures 2.1 and 2.2a. It is possible to reverse the relation in Equation (2.1) and have the domain description such that $\phi > 0$ represents the material domain. This choice has no influence on the LSM as a whole and is left up to the developer. However, it does require some changes in the geometric mapping scheme and derivation of the shape sensitivities, so careful consideration should be made to ensure consistency. In this dissertation the relations such as explained in Equation (2.1) are used.

To represent shape and topology changes in the material domain Ω a fictitious time t is introduced. It is assumed that the level set function is also implicitly a function of t. That is, as time t is advanced, the boundary $\partial\Omega$ on $\phi(\vec{x}) = 0$ is updated and a new design generated. In the LSM framework, the moving boundary can be updated by solving the

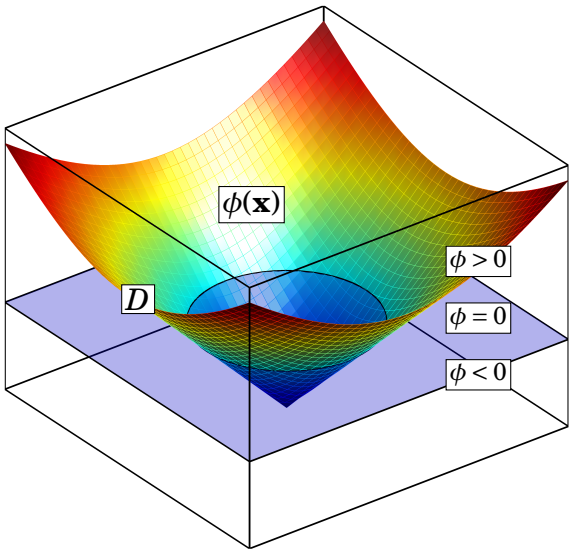

FIGURE 2.1. An LSF with a level-set representing the material domain D [45].

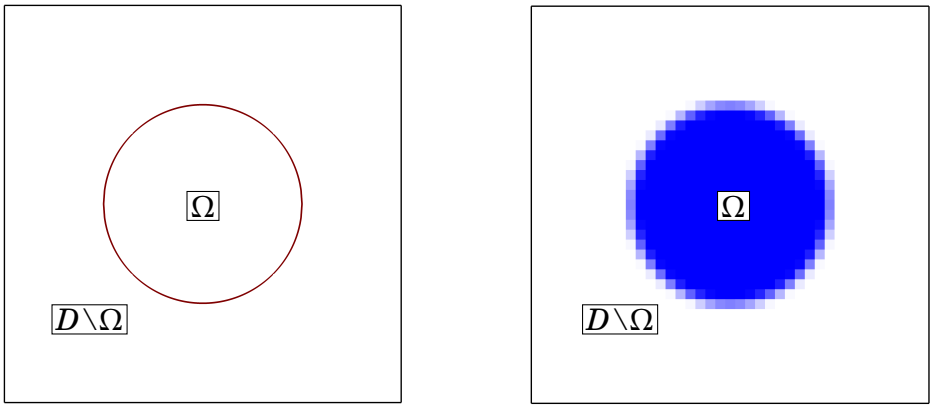

(a) The geometry boundary in the 2D level set domain corresponding to the LSF.

(b) The FE representation after density-based mapping.

FIGURE 2.2. Example of a material domain description with the LSM (figure a) and the FE description of the material domain (figure b) [45].

Hamilton-Jacobi PDE, also called the Level Set Equation (LSE):

$$\frac{\partial \phi(\vec{x},t)}{\partial t} + \nabla\phi(\vec{x},t)\frac{\mathrm{d}\vec{x}}{\mathrm{d}t} = 0 \tag{2.2}$$

where $\phi(\vec{x},t)$ is the time dependent LSF. This equation is somewhat abstract, it is helpful to rewrite the equation and introduce the normal velocity of the boundary. The boundary normal velocity $V_N(\vec{x},t)$ of the material boundary can be derived as follows:

$$\begin{aligned} V_N(\vec{x},t) = \quad & \vec{V}(\vec{x},t)\frac{\nabla\phi(\vec{x},t)}{\left|\nabla\phi(\vec{x},t)\right|} \\ \text{with:} \qquad & \vec{V}(\vec{x},t) = \frac{\mathrm{d}\vec{x}}{\mathrm{d}t}. \end{aligned} \tag{2.3}$$

The normal velocity V_N from equation (2.3) is substituted into the LSE from equation (2.2) to produce:

$$\frac{\partial \phi(\vec{x},t)}{\partial t} + V_N(\vec{x},t)\left|\nabla\phi(\vec{x},t)\right| = 0. \tag{2.4}$$

The normal velocity is a function of the location vector $\vec{x}$, meaning the boundary can be updated locally. The normal velocity is related to the sensitivity of the objective function with respect to the boundary variation. Hence, updating the LSF $\phi(\vec{x})$ by solving the LSE is equivalent to moving the material boundary along the normal direction.

The LSM was developed to track propagating boundaries. To use it for structural optimization, appropriate velocity function values $V_N(\vec{x},t)$ for use in equation (2.4) should be provided.

2.1.1 Procedure & Signed Distance Function

It was mentioned in the introduction that solving the LSE for the LSM requires computationally expensive numerical techniques. Different approaches for solving this PDE are currently being researched; popular and commonly used is the upwind-scheme [7, 23, 109]. This scheme solves the LSE from equation (2.4) both temporally and spatially. Conventionally the LSF is updated by providing appropriate values for V_N and numerically solving the LSE in equation (2.4).

First, the Signed Distance Function (SDF) and its property is introduced. This property can significantly reduce the complexity of solving the LSE. The SDF is written as in Equation (2.5):

$$\left|\nabla\phi(\vec{x})\right| = 1 \quad \forall \quad \vec{x} \in D. \tag{2.5}$$

This means the norm of the gradient of the LSF is equal to 1 everywhere on the design domain. This is a very useful property as will be shown in the implementation of the

up-wind scheme. The SDF does require initialization of the LSF, which will be further discussed in a separate section.

Assume the SDF from Equation (2.5) holds true at all times t, then the LSE from Equation (2.4) can be rewritten as follows:

$$\frac{\partial \phi(\vec{x},t)}{\partial t} + V_N(\vec{x},t) = 0. \tag{2.6}$$

Now the Hamilton-Jacobi equation or LSE is transformed into a set of ODEs. This means that instead of solving the LSE both in time and spatially, the LSE needs only to be solved in time. This useful observation was first applied by Yamasaki et al. [114]. The explicit method can be used to do the following update step for the LSF:

$$\begin{aligned} &\frac{\phi(\vec{x},t+\Delta t) - \phi(\vec{x},t)}{\Delta t} + V_N(\vec{x},t) = 0; \\ &\phi(\vec{x},t+\Delta t) = -V_N(\vec{x},t)\,\Delta t + \phi(\vec{x},t). \end{aligned} \tag{2.7}$$

This is an explicit, forward in time, solving scheme. Therefore a maximum time step, Δt_{crit}, is introduced to ensure numerical stability. This condition is known as the Courant-Friedrichs-Lewy (CFL) condition and described as follows:

$$\Delta t_{\text{crit}} \leq \frac{l_{\text{crit}}}{\max(V_N)} \tag{2.8}$$

where l_{crit} is the critical element side length, e.g. the minimal side length in the design domain. To further increase the stability of the overall optimization, the critical time step determined by the CFL condition is multiplied with a positive factor, $t_{\text{fac}} \leq 1$. The minimal time step explicitly controls the speed of the Level Set boundary moving through the design domain. Depending on the initial design, the convergence speed is therefore in part controlled by this time step from Equation (2.8).

2.1.2 Structural Performance & Geometry Mapping

With the LSM as a changing mathematical entity, the structural shape and topology can be described. However, in order to optimize the structure, structural performance criteria need to be calculated. A common way to do this is with the FEM. Therefore a way to transfer the geometry description is needed; from the LSM to the FE discretization needed for the numerical simulation. This is called mapping and there are many different methods to achieve this.

Here, we regard two distinct mapping methods necessary for use within the LSM:

- **Geometry mapping** is concerned with mapping the evolving geometry to the mechanical model. Multiple mapping techniques are common with LSM for structural optimization, among others: Conforming discretization, Immersed boundary techniques and Density-based approaches [107]. In this research, the FEM technique is used for the mechanical model, as common choice for the type of problem presented here. The Extended-FEM or X-FEM technique is a popular choice for the Immersed boundary approach, largely due to its capacity to accurately model the continuous surface boundary produced by the LSM [63, 111]. With the standard linear implicit FEM, the mesh remains unchanged when solving for structural problems. As a result, the FE mesh is unable to accurately model the evolving zero-level set boundary. This means this LSM surface boundary practically flows through the elements during the update procedure and needs to be interpolated to the numerical model.

- **LSF discretization** is commonly done with a Finite Difference (FD)-based approach, meaning a FD-grid is required. In principle both, the FD-grid and FE-grid, can have different designs. However, for simplicity and ease of implementation, the FD-grid for the LSF discretization is equal to the FE-grid for the structural simulation. This means, the LSF discretization has its nodes coincide with the FE-mesh nodes.

As explained, the surface boundary described by the LSM is not limited to the FE-grid and therefore crosses the elements. To adequately assess the structural performance of the design, an accurate interpolation of the design to the discretization for the FEM is required. In this research, the surface boundary is interpolated onto the FE-grid by an intermediate density field, i.e. ersatz material, indicating the amount of material at each point of the design domain. This approach is similar to the approach by the Solid Isotropic Material with Penalization (SIMP) method [14]. However, the surface boundary from the LSM allows for adjusting the element density only around the surface boundary. This means the material density is either one or zero everywhere except within a predefined bandwidth around the domain boundary. Benefits of this approach are explained in a later section.

The function used to determine the material density should be differentiable in order to derive the shape sensitivities consistently. The Heaviside function provides that capability and is therefore often used in LSMs. The Heaviside function can be used to

determine the material density $\rho(\phi)$ as follows:

$$\rho(\phi) = H\left(\phi(\vec{x})\right) \tag{2.9}$$

where H is defined as the exact Heaviside function:

$$H\left(\phi(\vec{x})\right) = \begin{cases} 1 & \forall \quad \phi \leq 0 \\ 0 & \forall \quad \phi > 0 \end{cases}. \tag{2.10}$$

The derivative of the Heaviside function is the Dirac delta function:

$$\delta\left(\phi(\vec{x})\right) = \begin{cases} \delta \to \infty & \forall \quad \phi = 0 \\ 0 & \forall \quad \phi \neq 0 \end{cases}. \tag{2.11}$$

However, the exact definition of the Heaviside function in Equation (2.10) is discontinuous and can lead to numerical issues during optimization. The binary definition of the material density reduces the accuracy of the LSF update procedure. In order to solve this problem, a relaxed Heaviside function definition, based on the work by [109], is introduced:

$$\tilde{H}\left(\phi(\vec{x})\right) = \begin{cases} 1 & \forall \quad \phi < -h \\ \frac{1}{4}\left(\frac{\phi}{h}\right)^3 - \frac{3}{4}\left(\frac{\phi}{h}\right) + \frac{1}{2} & \forall \quad -h \leq \phi \leq h \\ 0 & \forall \quad \phi > h \end{cases} \tag{2.12}$$

The derivative of $\tilde{H}\left(\phi(\vec{x})\right)$ in Equation (2.12) is the relaxed Dirac delta function $\tilde{\delta}\left(\phi(\vec{x})\right)$:

$$\tilde{\delta}\left(\phi(\vec{x})\right) = \begin{cases} \frac{3}{4}\left(\frac{\phi^2}{h^3}\right) - \frac{3}{4h} & \forall \quad -h \leq \phi \leq h \\ 0 & \forall \quad \phi < -h, \quad \phi > h \end{cases} \tag{2.13}$$

It should be noted that the definition in Equation (2.9) can result in an element density of zero. This leads to singularities in solving the mechanical problem during the FE-analysis. A commonly used solution to this issue is to rewrite the definition in Equation (2.9) as follows:

$$\rho(\phi) = \epsilon + (1-\epsilon)H\left(\phi(\vec{x})\right) \tag{2.14}$$

where ϵ is a small number representing a minimum density. Another solution which can be used with the LSM and not with SIMP is to delete the element definitions in the FE-grid with a zero density. Elements can be created again as soon as the surface boundary crosses into the corresponding FD-grid element. This goes naturally if the interpolation scheme is correctly applied. This way no singularities can arise and no minimal material density is required. Artifacts due to the presence of low density 'void' elements are avoided as well.

2.1.3 Calculating the volume fraction

With the mapping methods described in the previous section, a problem becomes apparent. The LSF is discretized on the FE-grid with the LSF values on the nodes. Consequently the relaxed Heaviside values, $\tilde{H}\left(\phi(\vec{x})\right)$, are also given on the nodes. Yet, for the element volume fraction we need to calculate $\rho(\phi)$ on an element level. Because of this, it is necessary to calculate $\tilde{H}\left(\phi(\vec{x})\right)$ on element level. This necessity is unfortunately often left out in literature and left up to the user to realize, although van Dijk et al. [106] mention this issue shortly in their paper.

A good way of solving this issue is to average the nodal Heaviside values to the element level. Care has to be taken, because while $\phi(\vec{x})$ might be linearly interpolated on the element (with use of the element shape functions $\vec{N}$), the Heaviside function, $\tilde{H}\left(\phi(\vec{x})\right)$, is and cannot. This is because the relation between $\tilde{H}$ and ϕ is not linear. For small values of the bandwidth, h, large areas of the element might have a constant value for $\tilde{H}$ of 1 or 0. This could mean that while the boundary is moving over the element, nodal values of $\tilde{H}\left(\phi(\vec{x})\right)$ of that element do not change. Simply taking the average can lead to an unchanging element density, while the change in nodal LSF values, ϕ, should suggest a change in density. To ensure a consistent sensitivity calculation, the element volume fraction should be calculated by integrating $\tilde{H}\left(\phi(\vec{x})\right)$ over the element and dividing by the total element volume:

$$\tilde{H}\left(\phi(\vec{x})\right)\Big|_e = \frac{\int_{D_e} \tilde{H}\left(\phi(\vec{x})\right) \mathrm{d}D_e}{\int_{D_e} \mathrm{d}D_e}. \tag{2.15}$$

This is unfortunately a computationally intensive procedure, often solved with FEM, and slows the optimization process considerably. With a sufficiently large bandwidth h, the averaging method will provide results with a relatively small error compared to the integration method. The bandwidth should be at least larger than the critical element side length.

2.1.4 Reinitialization

In order to ensure the property from Equation (2.5), the LSF needs to be transformed, however without changing the shape of the surface boundary or zero level set contour. The goal of the LSM is to be able to track and control a moving boundary shape, enforcing an SDF property of the LSF does not interfere with the shape results. The process of transforming the LSF into an SDF is often called reinitialization.

Conventionally, in the field of LSMs, this process is applied, because the convergence of an LSM can deteriorate when the magnitude of the spatial gradient of the LSF strongly varies along the surface boundary or zero-level contour [107]. Imagine a steep LSF, i.e. the spatial gradient $\nabla\phi(\vec{x})$ is high, around the boundary, an update of the LSF would result in a small boundary displacement. For a flat LSF, i.e. low spatial gradient, around the boundary, the opposite is true. In order to avoid this problem, the LSF is reinitialized as an SDF where the zero-level contour or material boundary is maintained.

During the update procedure of the LSE, the LSF is changed to allow for a movement of the zero-level contour, i.e. the material boundary. The challenge lies in reinitializing the LSF into an SDF while maintaining the zero-level contour as accurately as possible. Different reinitialization schemes have been proposed over the years, but the calculation is often complex and computationally expensive.

The reinitialization in this dissertation fulfils another important function; it ensures the signed distance property of the LSF in order to reliably use the explicit update method from Equation (2.7). The method used for reinitialization should therefore provide very accurate results. To avoid inaccuracy, a computationally expensive but very accurate novel geometry-based reinitialization scheme, developed by Yamasaki et al. [114], is introduced here.

This schemes takes the LSF values on the FE grid nodes and interpolates, using the element shape functions $\vec{N}$, N_P points on the zero-level contour inside and on the edges of the element. These interpolated points are collected in set P. The points in P form the surface boundary created by the zero level set contour. In the next step, each LSF value on each node on the FE grid is compared with all the interpolated points in set P. The value of the shortest distance between the node and a point is used as the new value for the LSF at that node. The sign of the new LSF is equal to that of the old one. This way an LSF is created with a slope very close or equal to 45° on all points. This method can be summarized as follows:

$$\phi_i^{\text{new}} = \text{sgn}(\phi_i^{\text{old}}) \times \inf_{\vec{p}\in P} d(\vec{x}_i, \vec{p}) \tag{2.16}$$

where the superscripts 'old' and 'new' denote ϕ before and after reinitialization, the subscript i denotes the i-th node, $\vec{x}_i$ are the coordinates of the i-th node. The operator $d(\vec{x}_i, \vec{p})$ gives the Euclidean distances between $\vec{x}_i$ and $\vec{p}$, where $\vec{p}$ are the coordinates of the interpolated points in set P. This reinitialization method creates interpolated points inside each element and can thus be expected to provide very accurate computation of the LSF values. Naturally, the method is shown to perform better than other commonly used

schemes based on the PDE in Equation (2.4) [114], since these other methods use only the nodal LSF values. For an in-depth discussion on the method, the reader is referred to the work by Yamasaki et al. in [114].

The reinitialization technique described above is computationally expensive, since every grid point is compared to all points in set P. Previously the relaxed Heaviside method was described, see section 2.1.2, which is used for the geometrical mapping of the LSF. Consequently only LSF values in the vicinity of the surface boundary described by $\phi = 0$ are updated. This is because of the Dirac delta function within the shape sensitivity, where the value for bandwidth h determines the area of influence around the boundary. Knowing this, the computational effort required for the reinitialization method can be substantially reduced. Instead of comparing the nodal LSF values on all grid points, only the grid points located within the bandwidth h of the material boundary $\phi = 0$ have to be reinitialized. The method is described below and depicted in Algorithm 1.

Firstly, all elements that are intersected by the material boundary are collected in set E_{bound}. Secondly, for element $e \in E_{\text{bound}}$, the connected elements are collected and the nodes that define these elements are put in a set. Then, the unique nodes from this set are collected in set N_e. The nodes n in N_e are compared to the points p in P_e, where P_e is a subset of P containing all interpolated points from the boundary element e. The smallest Euclidean distance is taken as the new LSF value for node n and multiplied with the sign of the LSF value. This process is repeated for all $e \in E_{\text{bound}}$. As some nodes will be compared more than once, the smallest distance has to be taken for the LSF value. The process described here works when the bandwidth parameter h is smaller than the critical element side length, otherwise relevant nodes, with non-zero velocity values, are disregarded. The algorithm can be extended to include a larger band of elements around the boundary, depending on the size of h. This of course has a negative influence on the required computational effort.

For the remainder of the research presented in this dissertation, it is recommended to perform a total domain reinitialization at least every 10 iterations. This is to ensure a consistent material boundary description over the design domain.

2.1.5 Regularization

Regularization is often employed during the update procedure of the LSF to remove numerical artifacts, simplify the problem, improve the convergence behavior and avoid convergence to local minima with poor performance [107].

for $e \leftarrow e \in$ *all elements on boundary, called* E_{bound} **do**
  create set of nodes connected to e, called N_{el};
  for $n \leftarrow n \in N_{el}$ **do**
    create set of element connected to n, called E_{node};
    for $el \leftarrow el \in E_{node}$ **do**
      add nodes of el to set N_e
    end
  end
  $N_e \leftarrow \text{unique}(N_e)$;
  P_e *are the points inside element e, a subset of* P;
  for $n \leftarrow n \in N_e$ **do**
    $\phi_n^{\text{tmp}} = \text{sgn}(\phi_n^{\text{old}}) \times \inf_{\vec{p} \in P_e} d(\vec{x}_n, \vec{p})$;
    $\phi_n^{\text{new}} = \min\left[\phi_n^{\text{new}}, \phi_n^{\text{tmp}}\right]$
  end
end

Algorithm 1: Narrow band algorithm for SDF reinitialization.

Here, two different approaches of regularization are presented. The first method is designed to smooth the sensitivities before updating the LSE and is based on the Helmholtz-type PDE [60, 115]. The second type adds a penalty function based on the zero level-set perimeter. Both approaches are discussed in the following:

Helmholtz-type regularization This approach is based on the Helmholtz equation and functions as a convolution filter. In other words, it diffuses or smoothens the velocity field on and around the zero level-set interface. The Helmholtz equation derived below is based on the work by Yamasaki et al. [115]:

$$(\vec{L} + \vec{H})\tilde{\vec{V}}_N = \vec{L}\vec{V}_N \tag{2.17}$$

where $\vec{V}_N$ is the nodal value vector of boundary normal velocities, i.e. the shape sensitivities. The variable $\tilde{\vec{V}}_N$ is the nodal value vector of the smoothed velocities. The matrices $\vec{L}$ and $\vec{H}$ in Equation (2.17) are defined as follows:

$$\vec{L} = \bigcup_{e=1}^{N_e} \int_{D_e} \vec{N}\vec{N}^{\mathrm{T}} \mathrm{d}D_e; \tag{2.18}$$

$$\vec{H} = \bigcup_{e=1}^{N_e} \int_{D_e} R^2 \left(\vec{N}_x \vec{N}_x^{\mathrm{T}} + \vec{N}_y \vec{N}_y^{\mathrm{T}}\right) \mathrm{d}D_e \tag{2.19}$$

$$\text{with:} \quad \vec{N}_x = \frac{\partial \vec{N}}{\partial \vec{x}}, \quad \vec{N}_y = \frac{\partial \vec{N}}{\partial \vec{y}} \tag{2.20}$$

where N_e is the total number of elements in the FE-discretization, D_e the element domain and R the regularization coefficient. For $R = 0$ no smoothing takes place and $\tilde{\vec{V}}_N = \vec{V}_N$, for $R \to \infty$ the Equation (2.17) becomes the Poisson's equation, i.e. the velocities are perfectly smoothed and equal. Equation (2.17) can be easily solved using the FEM, taking care that a four point Gaussian integration scheme is used.

Parameter penalty regularization This approach is based on penalizing shape updates that increase the total perimeter of the geometry. It is a common method of regularization and found for example in the works by Allaire et al. and Luo et al. [7, 70]. The perimeter is defined as:

$$P(\Omega) = \int_{\partial\Omega} \mathrm{d}S. \tag{2.21}$$

The perimeter $P(\Omega)$ is constrained by including it in the Lagrange formulation of the optimization problem as a penalty constraint. The shape sensitivity of the perimeter is equal to the mean curvature of the boundary, which is equal to the divergence of the boundary normal:

$$\kappa = \mathrm{div}\left(\frac{\nabla\phi(\vec{x})}{\left|\nabla\phi(\vec{x})\right|}\right). \tag{2.22}$$

The total shape sensitivity is then formed by extending the current velocity field with the mean curvature field, $\vec{\kappa}$, multiplied by a certain penalty constant, β:

$$\vec{V}_N^{\text{new}} = \vec{V}_N^{\text{old}} + \beta\vec{\kappa}. \tag{2.23}$$

The sharper a curve, the higher the curvature value is at that point. The sign of the curvature is positive in the direction of the curve center, hence by adding this parameter to the shape sensitivity, the boundary local velocity will be reduced depending on the amount of curve. This effectively smoothens the boundary and the parameter β dictates how much.

2.2 Classical Lamination Theory and Lamination Parameters

In this section the derivation of the stiffness parameters of a composite material will be explained. The method of determining the stiffness properties is commonly done using the Classical Laminate Theory (CLT). The theory assumes that the plies that make up the composite laminate are perfectly bonded by an infinitely thin adhesive layer. Furthermore the plies are either isotropic or orthotropic and thus have constant stiffness properties.

2.2.1 Classical Lamination Theory

The stresses in a single ply, loaded along its principal axes, can be related to ply strains via the following constitutive relation:

$$\begin{Bmatrix} \sigma_1 \\ \sigma_2 \\ \tau_{12} \end{Bmatrix} = \begin{bmatrix} Q_{11} & Q_{12} & 0 \\ Q_{12} & Q_{22} & 0 \\ 0 & 0 & Q_{66} \end{bmatrix} \begin{Bmatrix} \epsilon_1 \\ \epsilon_2 \\ \gamma_{12} \end{Bmatrix} \tag{2.24}$$

with σ_i and ϵ_i are the plane stresses and strains and where the Q_{ij}'s are defined as:

$$Q_{11} = \frac{E_1}{1-\nu_{12}\nu_{21}}, \quad Q_{12} = \frac{\nu_{21}E_1}{1-\nu_{12}\nu_{21}}, \quad Q_{22} = \frac{E_2}{1-\nu_{12}\nu_{21}}, \quad Q_{66} = G_{12}. \tag{2.25}$$

The relations given in Equations (2.24) and (2.25) describe the stiffness properties of a single ply in its principal directions. In Equation (2.25), E_1, E_2, G_{12} and ν_{12} are the constitutional material properties: principal Young Moduli and Poisson ratios. During stacking of plies into a laminate, the plies can be rotated from their principal direction, changing the stiffness properties in the global laminate directions; x and y. This gives rise to the following ply stress-strain relation in the global laminate x, y coordinate system:

$$\begin{Bmatrix} \sigma_x \\ \sigma_y \\ \tau_{xy} \end{Bmatrix} = \begin{bmatrix} \overline{Q}_{11} & \overline{Q}_{12} & \overline{Q}_{16} \\ \overline{Q}_{12} & \overline{Q}_{22} & \overline{Q}_{26} \\ \overline{Q}_{16} & \overline{Q}_{26} & \overline{Q}_{66} \end{bmatrix}_k \begin{Bmatrix} \epsilon_x^\circ + z\kappa_x \\ \epsilon_y^\circ + z\kappa_y \\ \gamma_{xy}^\circ + z\kappa_{xy} \end{Bmatrix}. \tag{2.26}$$

In Equation (2.26) k denotes the k^{th} ply in the laminate starting from the bottom most layer, z denotes the distance of a ply edge from the mid-plane of the laminate, see Figure 2.3 for a description. In Equation (2.26), the $\overline{Q}_{ij}$'s are the ply stiffness components, in

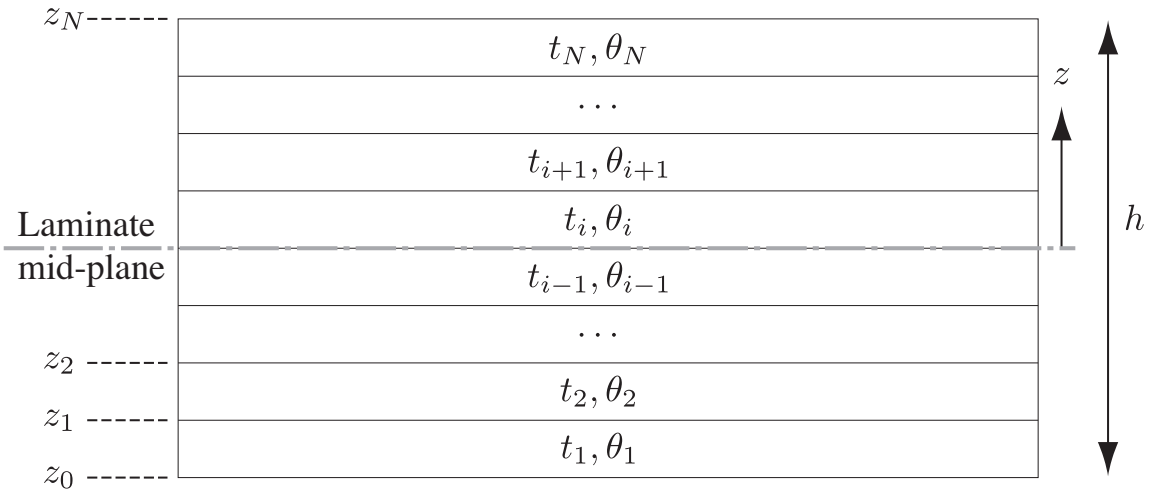

Figure 2.3: schematic view of a composite laminate consisting of N plies with orientations θ_k, thickness t_k and located at distance z_k from the mid-plane. (source: Ijsselmuiden [51])

the global coordinate system, they are defined as:

$$\begin{aligned}
\overline{Q}_{11} &= U_1 + U_2\cos 2\theta_k + U_3\cos 4\theta_k; \\
\overline{Q}_{12} &= U_4 - U_3\cos 4\theta_k; \\
\overline{Q}_{22} &= U_1 - U_2\cos 2\theta_k + U_3\cos 4\theta_k; \\
\overline{Q}_{66} &= U_5 - U_3\cos 4\theta_k; \\
\overline{Q}_{16} &= (U_2\sin 2\theta_k + 2U_3\sin 4\theta_k)/2; \\
\overline{Q}_{26} &= (U_2\sin 2\theta_k - 2U_3\sin 4\theta_k)/2.
\end{aligned} \tag{2.27}$$

In Equation (2.27) use is made of laminate invariants U. This set of five invariants completely describe the material properties of the laminate and are invariants with respect to the orientation angle. They are defined as:

$$\begin{aligned}
U_1 &= (3Q_{11} + 3Q_{22} + 2Q_{12} + 4Q_{66})/8; \\
U_2 &= (Q_{11} - Q_{22})/2; \\
U_3 &= (Q_{11} + Q_{22} - 2Q_{12} - 4Q_{66})/8; \\
U_4 &= (Q_{11} + Q_{22} + 6Q_{12} - 4Q_{66})/8; \\
U_5 &= (Q_{11} + Q_{22} - 2Q_{12} + 4Q_{66})/8.
\end{aligned} \tag{2.28}$$

To describe the stress resultants through the thickness, the stresses from Equation (2.26) are integrated over the thickness:

$$N_i = \int_{-\frac{h}{2}}^{\frac{h}{2}} \sigma_i dz, \quad M_i = \int_{-\frac{h}{2}}^{\frac{h}{2}} \sigma_i z dz. \tag{2.29}$$

In Equation (2.29) we have for the subscript $i = x, y$ or xy. N_i are the in-plane stress resultants of the laminate and M_i are the moment resultants. When the relations from Equation (2.26) are substituted into Equation (2.29) the following relations are derived:

$$\begin{aligned} \mathbf{N} &= \mathbf{A}\cdot\epsilon + \mathbf{B}\cdot\kappa; \\ \mathbf{M} &= \mathbf{B}\cdot\epsilon + \mathbf{D}\cdot\kappa. \end{aligned} \tag{2.30}$$

In Equation (2.30) the following relations are derived:

$$\begin{aligned} A_{ij} &= \sum_{k=1}^{N} \left(Q_{ij}\right)_k (z_k - z_{k-1}); \\ B_{ij} &= \tfrac{1}{2} \sum_{k=1}^{N} \left(Q_{ij}\right)_k \left(z_k^2 - z_{k-1}^2\right); \\ D_{ij} &= \tfrac{1}{3} \sum_{k=1}^{N} \left(Q_{ij}\right)_k \left(z_k^3 - z_{k-1}^3\right). \end{aligned} \tag{2.31}$$

The **A**, **B** and **D** matrices are the symmetrical stiffness matrices of the fully stacked laminate that describe the stress/strain relations in the global coordinates. The **A** matrix describes the in-plane ore membrane stiffness, the **D** matrix describes the out-of-plane or bending stiffness and the **B** matrix describes the coupling between the out-of-plane and in-plane strains to the in-plane and out-of-plane stresses, respectively.

2.2.2 Lamination Parameters

The Classical Laminate Theory (CLT), as presented in section 2.2.1, is commonly used to describe the stiffness behavior of an advanced composite laminate. There is however a different way to describe a laminate; Lamination Parameters (LPs). The LPs describe the stiffness properties invariantly of the ply orientation angles and thicknesses, which significantly reduces the amount of design variables. The LPs were first introduced by Tsai and Hahn [42].

The LPs are defined in Equation (2.32):

$$\begin{aligned} (V_{1\mathbf{A}}, V_{1\mathbf{A}}, V_{1\mathbf{A}}, V_{1\mathbf{A}}) &= \int_{-\frac{1}{2}}^{\frac{1}{2}} (\cos 2\theta, \sin 2\theta, \cos 4\theta, \sin 4\theta)\, d\overline{z}; \\ (V_{1\mathbf{B}}, V_{1\mathbf{B}}, V_{1\mathbf{B}}, V_{1\mathbf{B}}) &= 4\int_{-\frac{1}{2}}^{\frac{1}{2}} \overline{z}\,(\cos 2\theta, \sin 2\theta, \cos 4\theta, \sin 4\theta)\, d\overline{z}; \\ (W_1, W_2, W_3, W_4) &= 12\int_{-\frac{1}{2}}^{\frac{1}{2}} \overline{z}^2\,(\cos 2\theta, \sin 2\theta, \cos 4\theta, \sin 4\theta)\, d\overline{z}. \end{aligned} \tag{2.32}$$

In Equation (2.32), $V_{\mathbf{A}}$, $V_{\mathbf{B}}$ and W are the in-plane, coupling and bending LPs and $\overline{z}$ is the dimension normalized through the thickness.

The **A**, **B** and **D** matrices can be derived from the LPs with the following relation:

$$\begin{aligned}\mathbf{A} &= h(\mathbf{\Gamma}_0+\mathbf{\Gamma}_1V_{1\mathbf{A}}+\mathbf{\Gamma}_2V_{2\mathbf{A}}+\mathbf{\Gamma}_3V_{3\mathbf{A}}+\mathbf{\Gamma}_4V_{4\mathbf{A}});\\ \mathbf{B} &= \tfrac{h^2}{4}(\mathbf{\Gamma}_0+\mathbf{\Gamma}_1V_{1\mathbf{B}}+\mathbf{\Gamma}_2V_{2\mathbf{B}}+\mathbf{\Gamma}_3V_{3\mathbf{B}}+\mathbf{\Gamma}_4V_{4\mathbf{B}});\\ \mathbf{D} &= \tfrac{h^3}{12}(\mathbf{\Gamma}_0+\mathbf{\Gamma}_1W_1+\mathbf{\Gamma}_2W_2+\mathbf{\Gamma}_3W_3+\mathbf{\Gamma}_4W_4).\end{aligned} \tag{2.33}$$

The $\mathbf{\Gamma}$ matrices in Equation (2.33) are composed of only the laminate invariants and are formulated in Equation (2.34).

$$\begin{aligned}\mathbf{\Gamma}_0=\begin{bmatrix}U_1 & U_4 & 0\\ U_4 & U_1 & 0\\ 0 & 0 & U_5\end{bmatrix};\mathbf{\Gamma}_1=\begin{bmatrix}U_2 & 0 & 0\\ 0 & -U_2 & 0\\ 0 & 0 & 0\end{bmatrix};\mathbf{\Gamma}_2=\begin{bmatrix}0 & 0 & U_2/2\\ 0 & 0 & U_2/2\\ U_2/2 & U_2/2 & 0\end{bmatrix};\\ \mathbf{\Gamma}_3=\begin{bmatrix}U_3 & -U_3 & 0\\ -U_3 & U_3 & 0\\ 0 & 0 & -U_3\end{bmatrix};\mathbf{\Gamma}_4=\begin{bmatrix}0 & 0 & U_3\\ 0 & 0 & -U_3\\ U_3 & -U_3 & 0\end{bmatrix}.\end{aligned} \tag{2.34}$$

Now, the **A**, **B** and **D** matrices are completely described by the LPs V and W. For balanced and symmetric laminates, the LPs required to describe to stiffness properties reduce to: V_1, V_3, W_1 and W_3. Due to the invariant nature of the LPs, the stiffness matrices can be derived for any laminate with an arbitrary amount of plies and arbitrary thicknesses. This means a great computational advantage concerning the optimization of advanced composites for stiffness.

In this document, parameters for stiffness (or layup & stacking sequence) of the composite laminate(s) are based on the LPs [51, 104]. LPs considerably simplify the modeling of FRP composites and assist in decreasing the complexity of the whole design process. The answer of an FRP composite structure or laminate is a function of the stiffness matrices of the laminates, usually derived with the CLT. Typically, layer thicknesses, orientations and stacking order are regarded as design variables in the optimization of such laminates. The difficulty of this process of the description of a laminate is the high number of variables that have a partially discrete character. Alternatively, the LPs can be used as the design variables that entirely define the stiffness of the laminate properties.

As is customary for composite engineering, the laminates are supposed to be balanced and symmetrical in this research, resulting in a decrease of a maximum of twelve to four LPs to characterize all stiffness characteristics. This leaves the LPs $V_{i\boldsymbol{A}}$ and $V_{i\boldsymbol{D}}$ with $i = 1,3$, for membrane and bending stiffness respectively. The LPs $V_{i\boldsymbol{D}}$ are omitted as laminates in a traditional vehicle design, designed for crash absorption, are predominantly loaded in the plane. The comparatively large closed cross-sections from

the normally used tubular construction provides the bending resistance. For future applications, where the bending stiffness of the laminate has a greater influence on the structural reaction, LP $V_{i\boldsymbol{D}}$ should be included. In addition, due to manufacturing constraints, the number of available ply orientations are constrained to ±45°, 0° and 90°. This decreases the achievable range of the LPs space to [51, 75]:

$$\begin{aligned} 2V_{1\boldsymbol{A}} - 1 &\leq V_{3\boldsymbol{A}}; \\ -1 \leq V_{i\boldsymbol{A}} &\leq 1 \quad (i = 1,3). \end{aligned} \tag{2.35}$$

See Figure 3.24 for a visualization of the feasible area.

2.3 Simulation of Fiber Reinforced Composites in Crash

Non-linear transient dynamic analysis is an important method for the assessment of crash-worthiness. Often, numerical simulation tools such as FEM are used to apply this method and indeed, all research work presented in the introduction apply numerical simulation in one form or another. The same methods are used to simulate crash mechanics on fiber reinforced composites, however the modeling of the damage mechanics with composite materials is especially complex and different methods than for example with metals are needed. There are numerous publications on such simulations methods, for example [12, 16, 73]. Yet, none of them provides the accuracy and flexibility that are currently achieved for metals.

Two types of simulation methods are generally used for solving fiber reinforced composite problems with damage mechanics: Micro- and macro-mechanical simulations. With micro-mechanical simulation, details on the level of fiber/matrix interactions are simulated. Usually, micro-mechanical simulation focuses on fracture analysis and crack growth simulation, for example with the Extended-FEM (X-FEM) [55], phantom node method [74] and the Boundary Element Method (BEM) [103]. These simulations are generally carried out with implicit time step schemes and address mainly small scale problems on meso-scale up to the scale of coupon-like components. Other simulation types, such as the Virtual Crack Growth Technique (VCCT) [64], are suited for explicit FEM. The method requires predefined crack growth areas with a very fine mesh, which increases the computational effort significantly. Because of these reasons, micro-mechanical simulation methods are usually not used for crash analysis.

Macro-mechanical simulation generalizes the micro-mechanical material behavior into simplified constitutive models and material parameters, i.e. plies are modeled as one homogenized material. This type of simulation is often used in crash analysis of composite structures. A distinction of four general simulation types is proposed here:

1. The first type is using composite failure criteria in combination with explicit FEA, such as Tsai-Wu, Hashin and Puck [44, 89, 105].

2. The second type is using constitutive models based on Continuum Damage Mechanics (CDM) [56]. This method can be used together with the composite failure criteria.

3. The third type is CZM [52, 82], where inter-laminar behavior, for example delaminations, can be modeled. It should be noted that CZM can also be used in micro-mechanical simulations of crack growth [116], but also here a very fine mesh is required and simulation is computationally expensive.

4. The fourth type is CZONE [12, 68], which may be considered as a combination of CDM and an extra analysis step especially for the crush type failure.

CZONE uses crush stress parameters, which are determined by running carefully designed crush experiments on material coupons. The method is then able to interpolate the crush behavior for different layup designs. The advantage of CZONE is the computational efficiency, which allows for early phase and rough concept assessments. The downside is that extra material data is needed, which might not be available in the early design phase.

In this dissertation, a CDM damage model called Abq_Ply_Fabric with CZONE is used for modeling the damage behavior of carbon fiber composite materials.

An important consideration is that the responses should be chosen to adequately assess the crash performance of a structure. Some are maximum deflection, energy absorbed, acceleration on key locations (e.g. B-pillar) and minimal mass criteria. Maximum deflection can also be described by maximum intrusion of the impacting barrier and energy absorption is often quantified by the Specific Energy Absorption (SEA).

CHAPTER 3

METHODS

In this chapter, a novel design work-flow for advanced composite crash structures is presented. The proposed methods are divided into two main parts. The first part concerns the optimization of load paths taking crash loads and composite crush behavior into consideration. The second part introduces a complexity reduction work-flow that can be applied to the design from the first part.

The first part is based on a Level Set type shape optimization for crash. Here, shape optimization is used to improve the structural stability of crash loaded composite structures in the early phase development. The method uses shape and topology optimization to create structural solutions with clear and smooth material boundaries. An early stage composite vehicle concept is assessed using non-linear explicit simulation. This vehicle model and the simulation results are used in a multi-stage optimization work-flow to create load cases for optimization in the 2-D domain. The method provides control over shape development using a novel local volume constraint method. Some of the properties of the method are a novel coupling of explicit crash model and implicit LSM model using novel mapping methods and using a variation of the Equivalent Static Load (ESL) method to transform impact behavior into corresponding load cases. The resulting optimized material boundaries are described in terms of finite elements and continuous splines.

The second part is called design complexity reduction for automotive composite structures with respect to crashworthiness. Here, a combination of a novel physical surrogate model and sensitivity analysis are used to reduce the number of design parameters with-

out compromising the possible solution space. The Lamination Parameter (LP) method is used to efficiently characterize composite laminates. The Solution Space Identification (SSI) methodology is used to identify optimal boundaries for the remaining parameters.

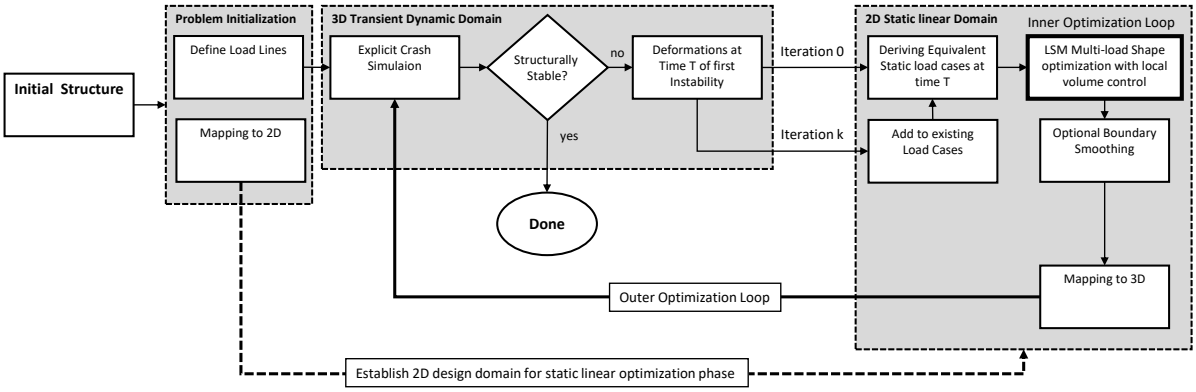

FIGURE 3.1. Overview of the proposed work-flow for crashworthiness shape optimization.

3.1 Work-flow for Crashworthiness Shape Optimization

In this section, the implementation of the LSM is explained, which is used to find optimal load paths for an initial composite vehicle structure. The background theory of the LSM for shape optimization is described in detail in Section 2.1. Now, this method is used for the optimization of load paths in a new framework.

The starting point of the optimization is some basic initial vehicle design with some essential structural components integral for the crashworthiness of the vehicle. These components are necessary components to absorb crash energy, for example longitudinal front rails, fire wall, which are pre-specified from prior decisions and knowledge. Normally, they are initially structurally unstable in crash and therefore do not fulfill their function as energy absorbing components. In section 1.2, the mechanics of composite crush and energy absorption are explained in detail. In order to have stable and progressive crush behavior, the components have to have a high level of structural stability. The novel framework presented in this section serves to find an optimal structural support system (load paths) to support these primary components in their optimal crash function for the duration of the crash and for multiple crash load cases.

This section is structured as follows. First, a method to map a 3D structure to a 2D representation of the design space is explained. This enables the identification of optimal orientations of the basic structures. Second, we explain how a new variant of the equivalent static load method [61] is used to transfer the 3D transient dynamic load case

to a linear elastic 2D representation. Third, we show how the LSM is used to optimize the load paths for composite structures. Finally, the method to map the 2D optimization results back to the 3D vehicle structure is explained. See Figure 3.1 for an overview of the work-flow.

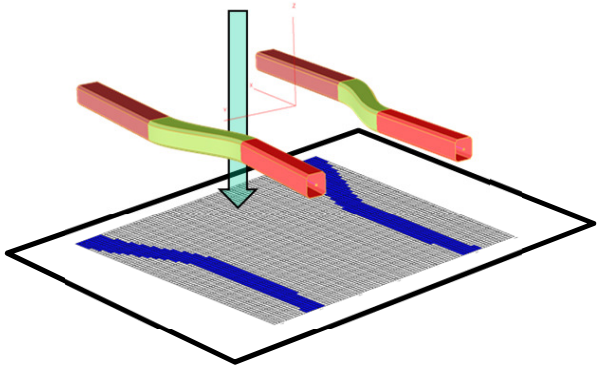

FIGURE 3.2. Basic 3D shell structure as example for the proposed mapping to 2D design domains.

3.2 Mapping Approach from 3D to 2D

In this section, the proposed method to map the components from a 3D vehicle structure representing the principal load paths to a 2D design domain is explained. Take for example the 3D shell structure as shown in Figure 3.2. The first step is to select a plane to project the component on. Convenient planes are the orthogonal planes in a Cartesian coordinate system. Then, a mesh is specified on the projection plane. This mesh will function later as part of the design space. A regular, quadrilateral mesh is a convenient choice, as many shape optimization methods only allow regular grids. Looking in the direction of the projection, through the component and onto the 2D grid, the result could be something like the image shown in Figure 3.3a.

A method is needed to check which elements in the structured grid should be filled. To do this, the center point of each element in the structured grid is taken and compared with the elements from the component's projected irregular mesh.

Take a point $p(x,y)$, which is the midpoint of a regular quadrilateral element from a predefined structured grid, see Figure 3.4. The triangles T_1, T_2 are formed by dividing the irregular quadrilaterals from the projected mesh into two triangles. To check if point $p(x,y)$ is inside triangle $T_{1,2}(p_1,p_2,p_3)$, a method based on the Barycentric coordinate system is used, see Equation (3.1).

$$\begin{aligned} x &= ax_1 + bx_2 + cx_3; \\ y &= ay_1 + by_2 + cy_3; \\ 1 &= a + b + c \end{aligned} \tag{3.1}$$

where x and y are the coordinates of point $p(x,y)$. The triangle T_i is defined by three

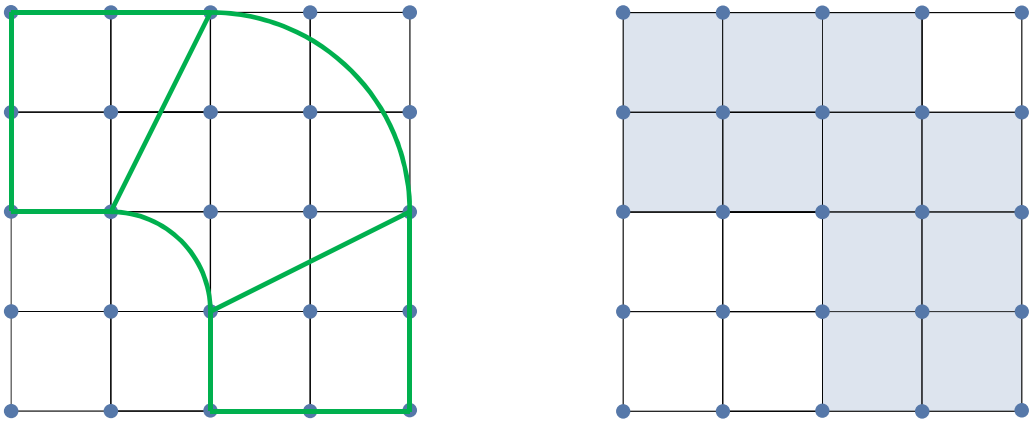

(a) Projected mesh on structured grid.

(b) Result after mapping.

FIGURE 3.3. Example of a projection of a 3D irregular mesh onto a structured grid.

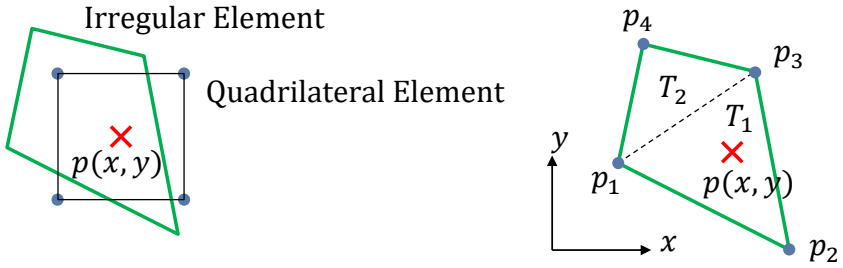

FIGURE 3.4. Irregular element projection on square element; illustration on how to find out if point $p(x, y)$ is in triangle T. The irregular quadrilateral is divided into two triangles, the element belonging to p is considered filled.

points $p_i(x,y)$ with $i = 1,2,3$, with coordinates x_i, y_i. The coefficients a, b and c are derived as follows:

$$\begin{aligned} a &= \frac{(y_2-y_3)(x-x_3)+(x_3-x_2)(y-y_3)}{(y_2-y_3)(x_1-x_3)+(x_3-x_2)(y_1-y_3)}; \\ b &= \frac{(y_3-y_1)(x-x_3)+(x_1-x_3)(y-y_3)}{(y_2-y_3)(x_1-x_3)+(x_3-x_2)(y_1-y_3)}; \\ c &= 1-a-b. \end{aligned} \tag{3.2}$$

The point $p(x,y)$ is in Triangle $T_{1,2}$ if the relation in Equation (3.3) holds true.

$$p \in T_{1,2} \quad \text{if:} \quad 0 \le a \le 1, \quad 0 \le b \le 1, \quad 0 \le c \le 1. \tag{3.3}$$

This check for midpoint $p(x,y)$ is performed for all elements in the structured grid. The result for the situation illustrated in Figure 3.3a is shown in Figure 3.3b.

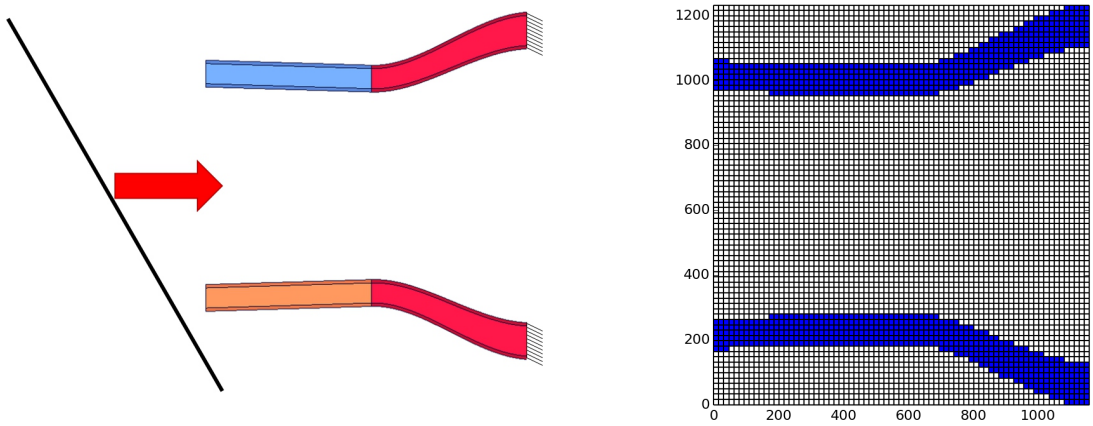

(a) Two composite beams impacted at 30°. The beams are clamped at their right ends.

(b) The structures mapped onto a 2D design domain.

FIGURE 3.5. Two composite beams impacted at 30°. Both, the 3D structure and 2D representation are shown.

3.3 Defining the Load Case

In this section, the method to derive a load case for the LSM optimization is explained. A 3D basic composite structure is subjected to one or more impact scenarios. These impacts generate deformation and failure behavior. The goal of the proposed load path optimization is to find a basic structure that stiffens the impacted structure to increase its crashworthiness. To explain the method, let us look at the scenario in Figure 3.5. Here two hollow composite beams are shown. The exact properties of these beams are not considered at this moment, only the behavior of the 3D structure after impact is considered. The beams are clamped at their right ends and impacted with a 30° rigid barrier. The resulting deformations of this impact are shown in Figure 3.6. The deformations due to the impact are non-linear, both the material and geometry show discontinuous, transient dynamic behavior over time. To translate the load case to a static linear environment, a snapshot is made at a certain time after impact. This snapshot represents the first moment the structure shows undesirable behavior. This snapshot is the main result that is transported in the outer optimization loop, see Figure 3.1. The assumption is made that in subsequent loops the structure remains stable for a longer period of time, generating a next snapshot at a later time point.

What is considered undesirable structural behavior needs to be assessed by the engineer and is not considered part of this research. In the situation presented in Figure 3.6, at 10 ms, the beam shows significant deflection away from the rigid barrier; the

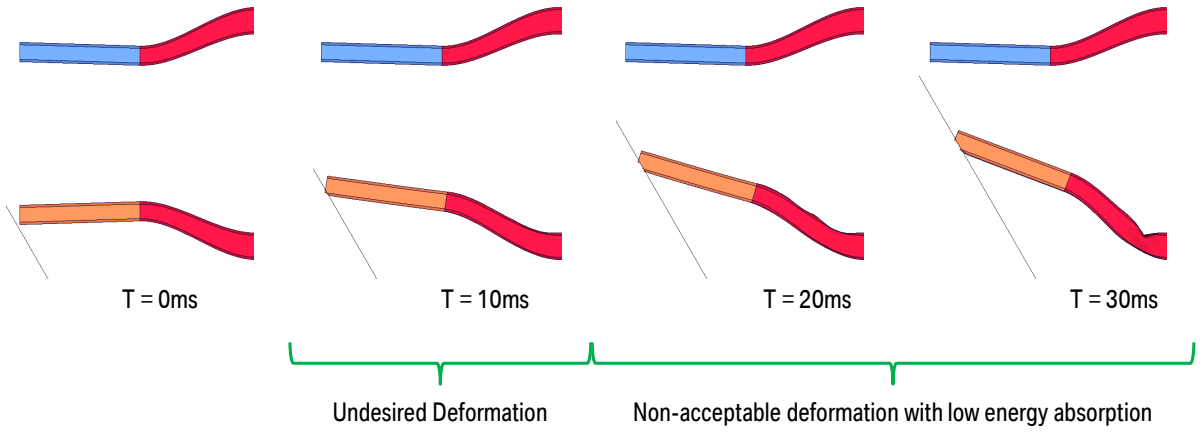

FIGURE 3.6. Non-linear impact analysis result of the initial basic structure in 3D; deformation result at 0, 10, 20 and 30 ms after impact.

structural rigidity is severely compromised. The preferable behavior would be that the beam remains stiff and absorbs the impact energy through progressive crushing. Therefore, this time point, 10 ms, is taken as the first snapshot.

The deformation state at the chosen time point is translated to a linear elastic and static load case via a modified ESL method. ESL is used, because it can relate the non-linear deformation of a structure to its equivalent load distribution on that structure in a linear system. The equivalent static loads are defined as the linear static load sets which generate the same response field in linear static analysis as that from non-linear dynamic analysis [61]. The ESLs are made from the results of non-linear dynamic analysis and used as external forces in linear static response optimization. The load distribution results in the exact same response field, or deformations as in the example load case, when solved. This way, a load case can be defined for a shape optimization based on static linear simulation that minimizes the compliance, such that the represented deformation is minimized as well. More on this method can be found in Kang & Park et al. [58, 59] and Kim & Park et al. [61]. However, commonly this method is applied such that the design domain and FEM mesh are the same between the dynamic and static analysis. The response field is taken from all nodes in the design domain and ESL are generated for all those nodes. This approach is not suitable for the presented example, where there are two distinct design spaces and a change from a 3D to 2D domain is realized. Here, a variation of the common ESL method is introduced.

Instead of using the complete response field, only a part of it is used. The load case is

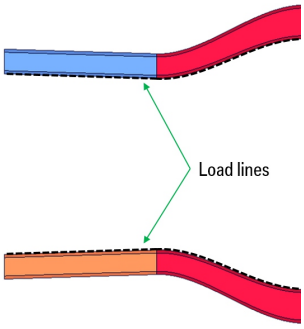

FIGURE 3.7. Example of load lines for transferring the displacements onto the 2D design domain.

derived for the 2D representation of these beams in the 2D design domain. Therefore, only a part of the response field from the 3D dynamic analysis can be used for calculating the ESLs. Furthermore, the crash structure that is assessed in the dynamic analysis, is part of the boundary of the design space for the shape optimization and not part of the shape optimization itself. The objective is to optimize a support structure changing in time for the main crash structure, therefore the behavior of the crash structure to be optimized should be related to by other means.

Here, a method is proposed that pre-defines certain regions on the 3D structure from which the deformations are taken; they are then mapped to the equivalent regions in the 2D representation. These regions are called 'load-lines'; for this example, they are defined as shown in Figure 3.7.

The load line should be chosen such that the same line can be represented in the 2D design domain. The load lines in Figure 3.7 are chosen on an edge that runs parallel to the projection plane. The in-plane and only the in-plane displacements of each node on this line are collected and mapped onto the 2D design domain. The displacements have to be interpolated because the 3D and 2D mesh are not identical. The mesh of the 2D design domain is significantly finer than the mesh of the 3D structure, therefore the interpolation of the displacements onto their counterpart load line in the 2D design domain is possible without making significant errors.

The displacements are normalized and applied on the beams in the 2D representation. The normalization is necessary to mitigate numerical error in the static linear optimization. Normalization is possible, because it will not affect the deformation distribution and subsequent optimum in the static linear domain. The modified ESL method works by solving this mechanical system to calculate the reaction forces on the nodes where

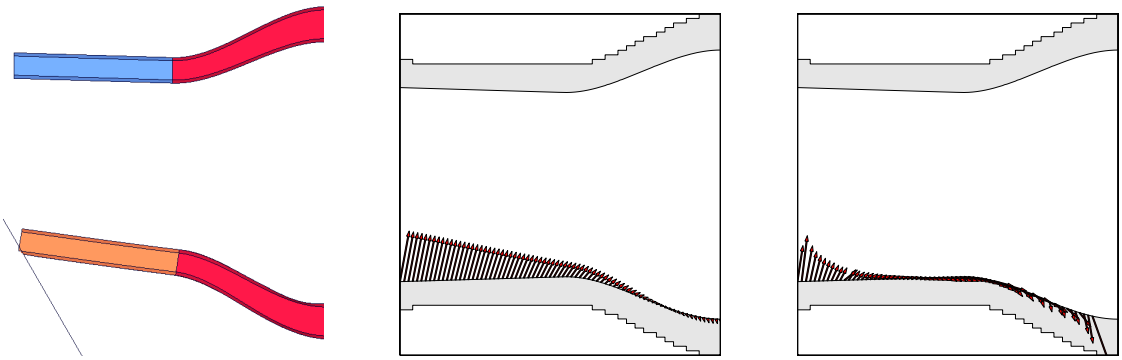

(a) Original deformed beam in the 3D space.

(b) Displacements normalized and mapped on LSM design space with initialized 2D design domain.

(c) Resulting equivalent static loads in the 2D domain.

FIGURE 3.8. Displacements and the ESL based on the impact case shown in Figure 3.6 at 10 ms.

the displacements are applied. These reaction forces are the equivalent static loads corresponding to the displacements; i.e. applying these loads to the linear system and solving for the nodal displacements, will result in the same displacements obtained in the original non-linear system. The result is shown in Figure 3.8.

Commonly, the design domain in between the beams, where the optimized load paths should be calculated, is left empty in the process of calculating the ESLs. However, doing this would mean that the two beams do not 'see' each other. There is no mechanical connection between the two beams. Therefore, when loads are applied to only one of them, the other will not react. More important, if the ESL is calculated with an empty design domain, the initial design with applied ESL for optimization will show a significantly different displacement behavior. Therefore, the ESLs are calculated with the same initial geometry design as is used to initialize the shape optimization, i.e. with initial material in the optimization domain. Two examples are shown in Figure 3.9.

At this stage a design domain for the shape optimization is defined and the load case or load cases are derived for the first snapshot and therefore first iteration of the outer optimization loop (see Figure 3.1).

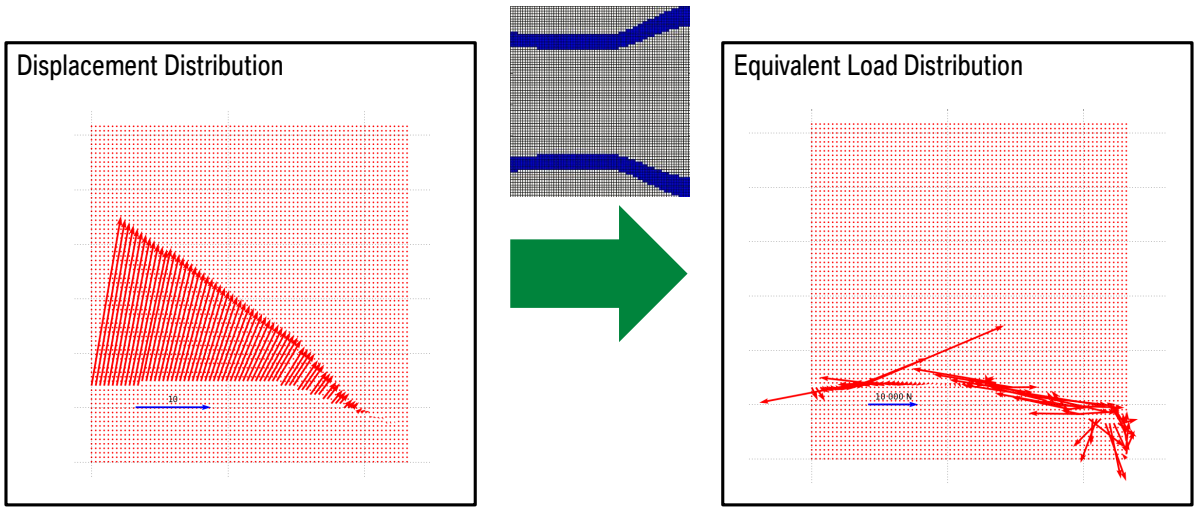

(a) The ESL distribution without initial material in optimization domain.

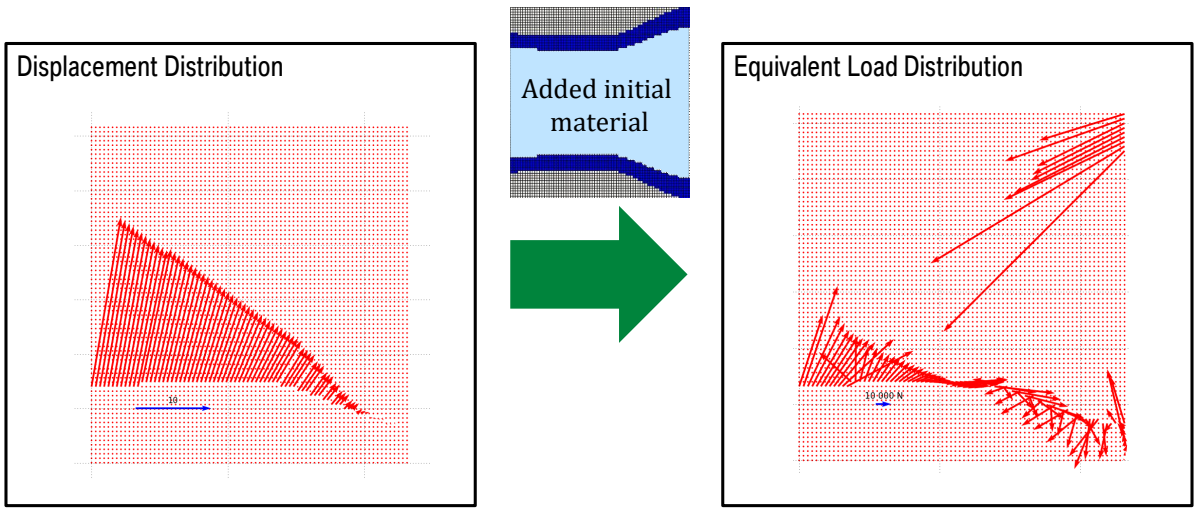

(b) The ESL distribution with initial material in optimization domain.

FIGURE 3.9. Different ESL distributions for two initial design domains; without and with initial material.

3.4 Level Set Method with Crush Constraints

The content of this section was partially published by the author in the journal Structural and Multidisciplinary Optimization [45]

Over the past decade the LSM has gained a broader interest. Yet relatively little research was done on including multiple constraints, especially when it concerns the conventional implementation of structural optimization with the LSM. The majority of the multi-constrained optimization problems in topology optimization are concerned with stress or strength constraints, where the strength is maximized by limiting local stresses. For the density based SIMP method, different examples can be found that solve a structural optimization problem with local stress constraints [17, 30, 67, 83, 117]. For the LSM however, the research is limited and involves a different variant of the problem. In many cases a stress-minimization problem is solved to achieve a similar effect; mitigating the difficulties due to the introduction of many stress-based design constraints by reformulating the objective function and deriving new sensitivities [5, 54, 108]. To transfer the standard ideas to the problem of crush optimization of composites several modifications are necessary which are presented in the following.

3.4.1 Definition of the Optimization Problem

In this section, a modified definition of the structural optimization problem is introduced. Here, we consider a standard objective, the minimization of the compliance of a design, with a novel set of constraints controlling local volumes. This is especially important for composite design where the crushing force measured in the complete area relates to a crush stress, a material constant, and the current area undergoing the crushing process at a certain time.

Single, Global Volume Constraint The standard optimization problem of minimizing the structural compliance subject to a single volume constraint is defined as follows:

$$\begin{aligned} \text{Minimize:} \quad & c(\phi(\vec{x})) \\ \text{Subject to:} \quad & g(\phi(\vec{x})) = V(\phi(\vec{x})) - V_{\max} \leq 0; \\ & \vec{\vec{K}} \cdot \vec{u} - \vec{f}^{\text{ext}} = \vec{0}; \\ & \phi \in \Psi. \end{aligned} \tag{3.4}$$

In Equation (3.4) c is the compliance, V equals the normalized volume fraction of the material domain Ω on D and $V_{\max}$ equals the maximum allowed normalized volume fraction of Ω on the design domain D. The global stiffness matrix is denoted by $\vec{\vec{K}}$, $\vec{u}$ is the nodal displacement vector and Ψ is the space of allowable LSF values ϕ. The structural problem is only subjected to traction forces $\vec{f}^{\text{ext}}$ at the boundaries and is not subjected to body forces. The inequality constrained optimization problem from Equation (3.4) needs to be transformed into an unconstrained problem. This transformation is achieved by deriving the Lagrangian $\mathscr{L}$:

$$\mathscr{L}(\phi(\vec{x})) = c(\phi(\vec{x})) + \lambda \left(g(\phi(\vec{x})) + s^2 \right) \tag{3.5}$$

where s is a slack variable which converts the inequality into an equality constraint. The Karush-Kuhn-Tucker (KKT) optimality conditions using shape derivatives, can be summed as follows:

- Gradient conditions:
$$\frac{\partial \mathscr{L}}{\partial \Omega} = 0, \quad \frac{\partial \mathscr{L}}{\partial \lambda} = 0; \tag{3.6}$$
- Feasibility check for inequalities:
$$s^2 \geq 0, \quad \text{or equivalently: } g(\phi(\vec{x})) \leq 0; \tag{3.7}$$
- Switching conditions:
$$\frac{\partial \mathscr{L}}{\partial s} = 2\lambda s = 0; \tag{3.8}$$
- Non-negativity of the Lagrange multiplier for the inequality constraint:
$$\lambda \geq 0. \tag{3.9}$$

Next, the formulation for the shape sensitivity can be derived. We set the compliance equal to the total strain energy:

$$c = \vec{u}^T \cdot \vec{\vec{K}} \cdot \vec{u}. \tag{3.10}$$

The stiffness matrix $\vec{\vec{K}}(\vec{\rho})$ is determined as follows:

$$\vec{\vec{K}}(\vec{\rho}) = \bigcup_{e=1}^{N_e} \rho_e(\phi) \vec{\vec{K}}_e \tag{3.11}$$

where $\bigcup$ denotes the assembly of element components, N_e is the total number of elements, $\vec{\vec{K}}_e$ is the element stiffness matrix and ρ_e is the element mass density determined by the

LSF values. The strain energy density is determined as follows:

$$\begin{aligned} c &= \sum_{e=1}^{N_e} \rho_e(\phi) \vec{u}_e^T \cdot \vec{K}_e \cdot \vec{u}_e \\ &= \sum_{e=1}^{N_e} \tilde{H}\left(\phi(\vec{x})\right) \vec{u}_e^T \cdot \vec{K}_e \cdot \vec{u}_e \end{aligned} \tag{3.12}$$

where $\tilde{H}\left(\phi(\vec{x})\right)$ is the relaxed Heaviside function, see the part on Structural Performance & Geometry Mapping 2.1.2 in the methods background chapter.

The shape derivative of the Lagrangian $\mathscr{L}$ is derived as the Fréchet derivative with respect to ϕ as follows:

$$\frac{\mathrm{d}\mathscr{L}}{\mathrm{d}\Omega} = \left\langle \frac{\mathrm{d}\mathscr{L}}{\mathrm{d}\phi}, \psi \right\rangle \tag{3.13}$$

where ψ is the variation of the level set function such that $\psi \in \Psi$. Combining Equations (3.5) and (3.13), the following is derived:

$$\frac{\mathrm{d}\mathscr{L}}{\mathrm{d}\Omega} = \frac{\mathrm{d}c}{\mathrm{d}\Omega} + \lambda \frac{\mathrm{d}g}{\mathrm{d}\Omega}. \tag{3.14}$$

For a more detailed derivation of the shape derivatives of the objective and constraints, see Appendix A. The final formulation of the sensitivities are as follows. For the shape sensitivity of the compliance, we get:

$$\frac{\mathrm{d}c}{\mathrm{d}\Omega} = -\sum_{e=1}^{N_e} \tilde{\delta}\left(\phi(\vec{x})\right) \vec{u}_e^T \cdot \vec{K}_e \cdot \vec{u}_e \psi. \tag{3.15}$$

For the shape sensitivity of the inequality constraint g:

$$\frac{\mathrm{d}g}{\mathrm{d}\Omega} = \sum_{e=1}^{N_e} \tilde{\delta}\left(\phi(\vec{x})\right) \psi. \tag{3.16}$$

Based on the discussion in a paper by Wang et al. [109], the normal velocity V_N from the LSE (Equation (2.4)) is expressed as follows:

$$V_N(\vec{x}, t) = \frac{\mathrm{d}\mathscr{L}}{\mathrm{d}\phi}. \tag{3.17}$$

The shape derivative of the Lagrangian can now be defined by substituting the results from Equations (3.15) and (3.16) into Equation (3.14) and taking the derivative with respect to the LSF values:

$$\frac{\mathrm{d}\mathscr{L}}{\mathrm{d}\phi} = \sum_{e=1}^{N_e} \tilde{\delta}\left(\phi(\vec{x})\right) \left[-\vec{u}_e^T \cdot \vec{K}_e \cdot \vec{u}_e + \lambda \right]. \tag{3.18}$$

The Lagrangian formulation of the optimization problem contains a slack variable s to account for the inequality constraint. The switching condition from Equation (3.8) can be satisfied in two ways:

- $\lambda = 0$: This implies that the inequality condition is inactive, meaning that the suggested optimum features a lower volume fraction than $V_{\max}$. However, for problems with fixed boundary conditions and fixed loads, not considering body forces, the compliance is minimized when the design domain is completely filled with material. This fact makes this case physically irrelevant.
- $s = 0$: Zero slack implies an active inequality constraint, $g(\phi) = 0$, indicating that $V(\phi) = V_{\max}$ for the optimum solution.

These cases show that the optimum will always lie at $V(\phi) = V_{\max}$. As a result of this, one could define the volume constraint in Equation (3.4) as an equality constraint. The slack variable s is now redundant and omitted.

Multi-domain or Local Volume Constraints We introduce a method to constrain multiple local volume domains. With this method the user can assert more control over the topological development during optimization. By restraining the volume in sub-domains, the optimization algorithm is forced to find different solutions. This extended control can be used to create optimal topology, which better fit the intended application of the user. In this case constant volume areas can be created which allow for control over the crush force of the entire structure. Also, by controlling the local volume, slender members can be enforced, which can benefit the crashworthiness of the structure.

For this method, three possible domain descriptions are introduced:

1. $D_{\text{loc, eq}}$: This is the combined domain of all local volume domains, $D_j^{\text{loc, eq}}$, that are controlled via equality volume fraction constraints.
2. $D_{\text{loc, ineq}}$: This is the combined domain of all local volume domains, $D_h^{\text{loc, ineq}}$, that are controlled via inequality volume fraction constraints.
3. D_{glob}: This is the domain that is left after all local domains are established.

The volume fraction of the entire design domain is still controlled by the previously introduced Lagrange multiplier λ, which will now be denoted λ^{glob}. Extra multipliers λ_i^{loc} for $i = 1 \dots N_{\text{dom}}$ are introduced for N_{dom} volume domains. The local volume domains are controlled in much the same way as the global volume constraint; the multiplier belonging to a volume domain is updated with the same update method as the global multiplier, with the difference that the update is based on the difference between the local volume fraction V_i^{loc} and a local required $V_i^{\text{loc, req}}$ or allowed maximum volume fraction $V_i^{\text{loc, max}}$ for $i = 1 \dots N_{\text{dom}}$.

Two scenarios are possible; we can define local volume domains with equality or with inequality constraints. The local equality constraint is handled much the same way as the global constraint, as the same physical relation between volume fraction and compliance is true. The equality and inequality constraints are defined as follows:

$$h_j(\phi(\vec{x})) = V_j^{\text{loc}} - V_j^{\text{loc, req}} = 0; \tag{3.19}$$

$$g_l(\phi(\vec{x})) = V_l^{\text{loc}} - V_l^{\text{loc, max}} \leq 0. \tag{3.20}$$

Contrary to the global inequality constraint, which behaves like an equality constraint, local inequality volume constraints are now physically sensible. This is due to the fact that each local volume domain also contributes to the global volume fraction, which is constrained as well. It is therefore possible that a local domain with low strain energy reduces in volume in favor of an area where the strain energy is higher, as long as the global volume constraint is met. This could result in local volume domains having a lower than maximum volume fraction at optimum. This behavior might be preferable and therefore a method is introduced to allow for local inequality volume constraints. The method works by comparing the local multiplier with the global one and taking the maximum, which allows to drive the local volume fraction further down if required.

Now the Lagrangian formulation of the optimization problem is described as follows:

$$\begin{aligned} \mathscr{L}(\phi(\vec{x})) = \quad & c(\phi(\vec{x})) + \lambda^{\text{glob}} g(\phi(\vec{x})) \\ & \ldots + \sum_{j=1}^{N_{\text{dom}}^{eq}} \lambda_j^{\text{loc}} h_j(\phi(\vec{x})) \\ & \ldots + \sum_{l=1}^{N_{\text{dom}}^{ineq}} \max\left[\lambda_l^{\text{loc}}, \lambda^{\text{glob}}\right] g_l(\phi(\vec{x})) \end{aligned} \tag{3.21}$$

where λ_j^{loc} and λ_l^{loc} are the local Lagrange multipliers for N_{dom}^{eq} equality and N_{dom}^{ineq} inequality constrained local volume domains. This optimization problem can be interpreted as finding a configuration, which exhibits a stationary Lagrangian $\mathscr{L}(\phi(\vec{x}))$ with respect to shape Ω and Lagrange multipliers λ^{glob}, λ_j^{loc} and λ_l^{loc}. In order to find such a configuration, the KKT optimality conditions must hold. The boundary normal velocity V_N can now be derived as:

$$\begin{aligned} & V_N = \tilde{\delta}\left(\phi(\vec{x})\right)\left[-\vec{u}^{\mathrm{T}}\vec{K}\vec{u} + \Lambda\right] \\ & \text{with: } \Lambda = \begin{cases} \lambda^{\text{glob}} & \forall\, \vec{x} \in D_{\text{glob}} \\ \lambda^{\text{loc, eq}} & \forall\, \vec{x} \in D_{\text{loc, eq}} \\ \max\left(\lambda^{\text{glob}}, \lambda^{\text{loc, ineq}}\right) & \forall\, \vec{x} \in D_{\text{loc, ineq}} \end{cases} \end{aligned} \tag{3.22}$$

Equation (3.22) shows three distinct cases.

- D_{glob}: Only the multiplier λ^{glob} is applied in this domain.
- $D_{\text{loc, eq}}$: Only the multipliers λ_j^{loc} are applied in these sub-domains. The volume of sub-domain j at optimum will be equal to $V_j^{\text{loc,req}}$.
- $D_{\text{loc, ineq}}$: Both, the multipliers λ_l^{loc} and λ^{glob} are applied in these sub-domains. The volume of sub-domain l at optimum will be equal to or lower than $V_l^{\text{loc,max}}$. The inequality is handled by the interaction between both multipliers.

3.4.2 Proposed Optimization Methods

In this section, two different methods are explained for optimizing the problems stated in the previous section 3.4.1.

First, a normalization parameter C is introduced, based on research by Otomori et al. [81]. This parameter normalizes the sensitivities, such that it makes the proposed LSM framework largely problem independent:

$$V_N = \tilde{\delta}\left(\phi(\vec{x})\right)\left[-C(\vec{u}^{\mathrm{T}}\vec{K}\vec{u}) + \Lambda\right]. \tag{3.23}$$

The normalization parameter C is defined as:

$$C = \frac{N_n}{\sum_{e=1}^{N_e} \rho_e \vec{u}_e^{\mathrm{T}} \vec{K}_e \vec{u}_e} \tag{3.24}$$

where N_n is the number of nodes in the LSF discretization and N_e the number of elements.

The sub-domain volumes are all normalized by their respective total sub-domain volume to form local volume fractions.

$$V_i^{\text{loc}} = \frac{\int_{D_i} \rho(\phi)\mathrm{d}D}{\int_{D_i} \mathrm{d}D} \tag{3.25}$$

where D_i defines a sub-domain of D. This makes all volume constraints, local and global, directly comparable and therefore their sensitivities as well. Hence, no further normalization is necessary for the constraints.

This research uses two separate update procedures for the Lagrange multipliers: Method one is used for the optimization case where only the global volume inequality constraint is active and method two when the local constraints (both equality and inequality) are active.

Method One, Secant Method The first multiplier update method uses the well-known secant method [8]. A small optimization is performed to find the best candidate multiplier λ^* for each level set update. The implementation used in the presented research is shown in Equation (3.26).

$$\lambda^{\{k+1\}} = \lambda^{\{k\}} - \frac{\lambda^{\{k\}} - \lambda^{\{k-1\}}}{h^{\{k\}}(\phi) - h^{\{k\}}(\phi)} h^{\{k\}}(\phi) \tag{3.26}$$

for $k = 2,\ldots,N$ where $\lambda^{\{k+1\}}$ is the multiplier suggestion for λ^* at the k-th iteration within the secant based optimization. The function $h^{\{k\}}(\phi)$ is defined as follows:

$$h^{\{k\}}(\phi) = V^{\{k\}}(\phi) - V^{\{k\}}_{\max} \tag{3.27}$$

where $V^{\{k\}}(\phi)$ is the current material volume ratio in the design domain and $V^{\{k\}}_{\max}$ is the maximum allowable volume ratio at iteration k. The value for $V^{\{k\}}_{\max}$ is slowly decreased from the initial volume ratio V_{ini} to the set maximum of $V_{\max}$. This steady decrease is required for stable convergence. Without it, the material volume would reduce too rapidly, not allowing for an optimal distribution driven by the compliance based sensitivity. This method of steady decrease is a type of constraint relaxation and its form is based on the findings by Otomori et al. [80]. The slope of the relaxation is set by the parameter N_{vol}, see Equation (3.28).

$$V^{\{k\}}_{\max} = V_{\max} + (V_{\text{ini}} - V_{\max}) \max\left[0, 1 - \frac{k}{N_{\text{vol}}}\right]. \tag{3.28}$$

The advantage of this secant based update method is that the constraint value is met almost perfectly for every iteration. The disadvantage is that the current volume has to be evaluated for every iteration k. The optimization is terminated either when a threshold is reached, e.g. $\left|h^{\{k\}}(\phi)\right| < 1 \cdot 10^{-4}$, or when the maximum of iterations is reached. The method is initialized with: $\lambda^{\{1\}} = 10$ and $\lambda^{\{2\}} = 0$ for the first LSM iteration. In subsequent iterations, the secant based method has to be initialized, we propose $\lambda^{\{1\}} = \lambda^{\text{old}}$ and $\lambda^{\{2\}} = 0$, where λ^{old} is the multiplier from the previous LSM iteration.

Method Two, Augmented Method The common augmented Lagrangian function for the equality-constrained problem is defined as [8]:

$$\mathscr{L}(\vec{x}, h(\vec{x}), r) = f(\vec{x}) + \sum_{i=1}^{N} \left[\lambda_i h_i(\vec{x}) + \frac{1}{2} r h_i^2(\vec{x})\right] \tag{3.29}$$

where $h(\vec{x})$ is the set equality constraints, N the number of these equality constraints, λ_i the Lagrange multiplier for the i-th equality constraint and r the penalty parameter.

Remember that the inequality constraint problem is actually an equality constraint problem in the case of compliance minimization with a single global volume constraint. Based on the general description from Equation (3.29), the Lagrangian from Equation (3.5) is rewritten as follows [23, 70]:

$$\mathscr{L}(\phi(\vec{x})) = c(\phi(\vec{x})) + \lambda h(\phi(\vec{x})) + \frac{1}{2\tau^{\{k\}}}(h(\vec{x}))^2 . \tag{3.30}$$

The Lagrange multiplier is updated as follows:

$$\begin{aligned} \lambda^{\{k+1\}} &= \lambda^{\{k\}} + \tfrac{1}{\tau^{\{k\}}} h(\vec{x}); \\ \tau^{\{k+1\}} &= \max\left(\alpha\tau^{\{k\}}, \tau_{\min}\right) \end{aligned} \tag{3.31}$$

with the proposed hyperparameters $\alpha = 0.9$ and $\tau_{\min} = 0.1$. Initial values for the Lagrange multiplier and penalty are necessary for each optimization problem. Good initial guesses are: $\lambda^{\{1\}} = 4.$ and $\tau^{\{1\}} = 100$.

Optimization Flowchart An overview of the complete optimization procedure is shown in the flowchart in Figure 3.10.

3.4.3 Benchmark Problems

In this section, typical example problems are solved to validate the presented methods; note that more problem related applications are given later in the results chapter, Section 4.1. The mechanical simulation is performed with CALCULIX [26], an open source FEM program. The material used is a quasi-isotropic material with normalized values for the mechanical properties: $E_1 = 1.542$, $E_2 = 1.542$, $G_{12} = 0.206$ and $\nu_{12} = 0.12$. In both examples the bandwidth parameter h is set to 0.5 times the element side length. Convergence is reached when the compliance does not change more than 0.1% in five subsequent iterations and the relative constraint failure is below 0.05%.

Example One This example is concerned with the compliance minimization of a centrally loaded cantilever beam, see Figure 3.11. The beam length over width ratio is $L/B = 1.515$, the mesh for the mechanical simulation consists of 100×66 quadrilateral 8 degrees of freedom shell elements. The unit load is applied downward at the center of the right edge of the beam, the left edge is fully clamped. The initial level set boundaries are distributed as a pattern of circular holes, also known as the “Swiss cheese” design. The optimization hyperparameters are as follows: parameter penalty factor $\beta = 0.$ and

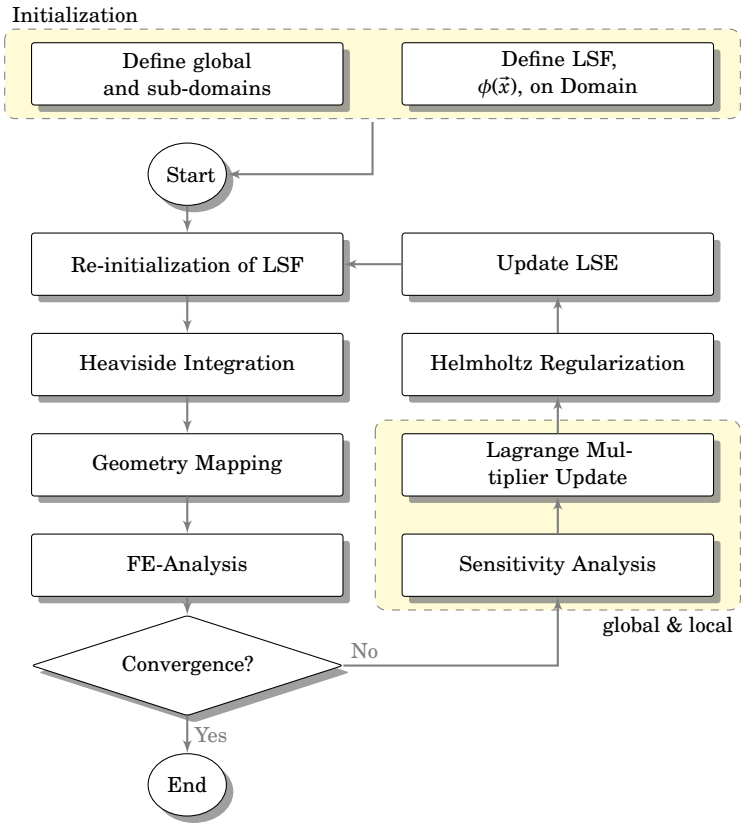

Figure 3.10: Optimization Flowchart.

CFL time step factor $\Delta t_{\text{fac}} = 0.9$. With $\beta = 0.$ the parameter penalty is switched off, meaning no boundary smoothing. For the Lagrange multiplier update, the parameters are as follows: no local constraints (secant method), $N_{\text{vol}} = 25$, with local constraints (augmented method), $\tau_0 = 100$ and $\lambda_0 = 4$.

The definition of the sub-domains for this problem is shown in Figure 3.12. The local volume fractions belonging to these sub-domains are, $V_{\text{loc}}^{\{N\}}$, with N equal to the number of sub-domains. Starting at the right edge, the first sub-domain with volume fraction, $V_{\text{loc}}^{\{1\}}$, of width, $\frac{1}{N}L_{\text{loc}}$, is defined, with a height equal to B. The next sub-domain with volume, $V_{\text{loc}}^{\{2\}}$, sits immediately next to the previous domain. This is repeated until N domains are created. For this example, we choose $L_{\text{loc}} = \frac{L}{2}$ and $N = 25$.

There are several ways to examine the difference between the method without and with local volume constraints. First a comparison is made between an optimization with only a global volume inequality constraint, $V^{\text{glob}} \leq V_{\text{max}}^{\text{glob}}$ and an optimization with both, a global and local inequality constraints, $V_{\text{loc}}^{\text{N}} \leq V_{\text{max}}^{\text{N}}$. Secondly, the optimization without local constraints is compared to the optimization with local equality constraints,

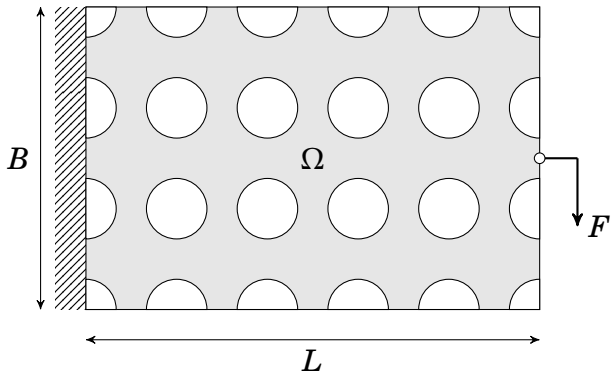

Figure 3.11: Centrally loaded cantilever and initial topology.

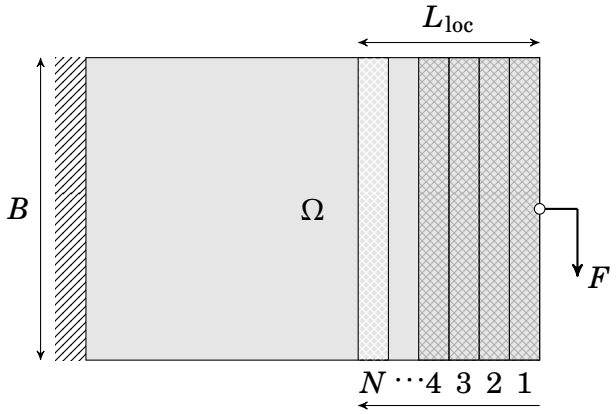

Figure 3.12: Definition of the local constraint domains for the centrally loaded cantilever beam.

TABLE 3.1. Overview of example cases and normalized optimal compliance values, P_{norm}, for the Cantilever Beam problem.

$V_{\text{max}}^{\text{glob}}$	$V_{\text{max}}^{\text{N}}$	$V_{\text{req}}^{\text{N}}$	P_{norm}
0.3	-	-	1.21
0.3	0.3	-	1.21
0.3	-	0.3	1.23

$V_{\text{loc}}^{\text{N}} = V_{\text{req}}^{\text{N}}$; see Table 3.1 for an overview.

Figure 3.13 shows the results for the first comparison case. The results show typical solutions to the cantilever beam problem. The optimum result without local volume constraints is taken as a reference solution and is shown in Figure 3.13a. All compliance values are normalized with respect to the initial compliance value, for an overview see Table 3.1. All cases are started with the same initial design. The normalized optimum

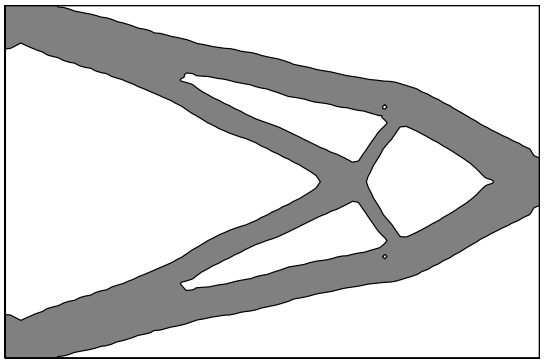

(a) Optimum with only a global constraint, $V_{\max}^{\text{glob}} \leq 0.3$.

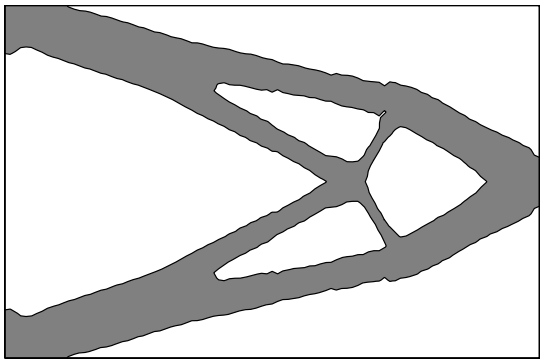

(b) Optimum with local inequality constraints, $V_{\max}^{\text{N}} \leq 0.3$, for $N = 1 \ldots 25$.

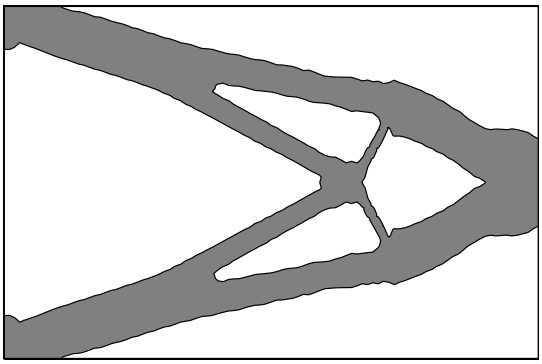

(c) Optimum with local equality constraints, $V_{\text{req}}^{\text{N}} = 0.3$, for $N = 1 \ldots 25$.

FIGURE 3.13. LSM based optima of the cantilever beam problem for both, without and with local volume constraints, $V_{\max}^{\text{glob}} \leq 0.3$ and $V_{\text{req}}^{\text{N}} = 0.3$, for $N = 1 \ldots 25$

compliance of the reference is 1.21. With local inequality constraints active, the optimum results look significantly different, see Figure 3.13b. The proposed LSM successfully applied the local inequality constraints, resulting in different topology. The global constraint with $V_{\max}^{\text{glob}} = 0.3$ ensured a total volume ratio equal to that of the reference example. The optimal compliance for this case is 1.21. The lack of strong topological / geometric changes on the boundaries between the sub-domains signifies the robust and smooth interaction between global and local constraints. The result with local equality constraints active, shown in Figure 3.13c, has a similar topology compared to Figure 3.13b. The effect of the equality constraint is most notable in the nose area of the cantilever structure. The nose shows a constant thickness distribution, because of the equality condition and required

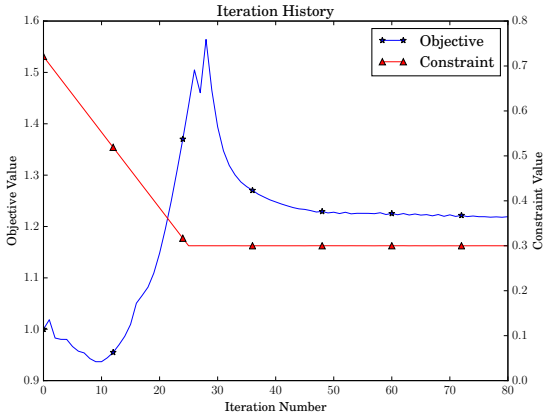

(a) Optimization history with $V_{\text{req}}^{\text{glob}} \leq 0.3$.

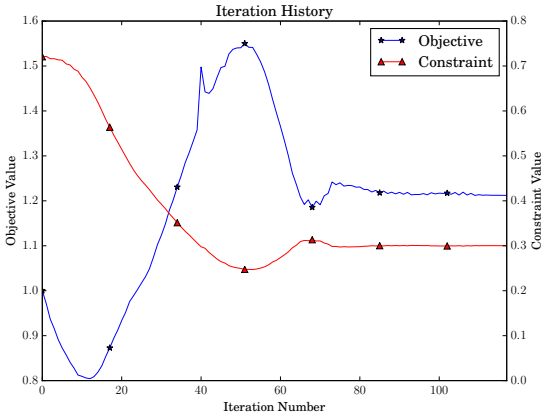

(b) Optimization history with $V_{\text{req}}^{\text{N}} \leq 0.3$, for $N = 1 \ldots 25$.

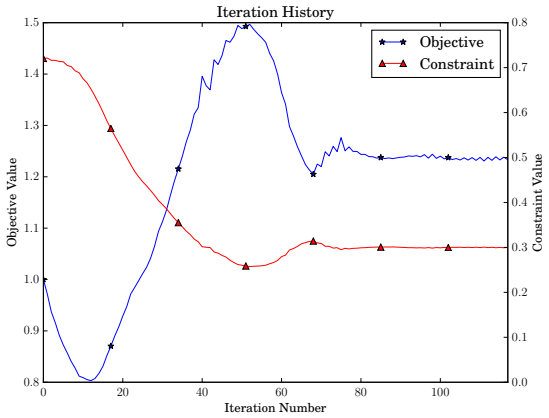

(c) Optimization history with $V_{\text{req}}^{\text{N}} = 0.3$, for $N = 1 \ldots 25$.

FIGURE 3.14. Optimization histories for case 1, corresponding to the results shown in Figure 3.13. The objective value is normalized with respect to the initial design.

volume of 0.3 per column. The optimal compliance for this case is 1.23, which is the highest of the three. An explanation is that here the design space is constrained the most, when compared to the other optimizations, leaving a less optimal result as the optimum. However, the increase in compliance due to this effect is small. The optimization histories belonging to the optimizations shown in Figure 3.13 are shown in Figure 3.14. The history for the reference case without local constraints active, Figure 3.14a, shows a different behavior for the constraint value than the other two. This is because of the Lagrange multiplier update scheme, which is different than for the cases with

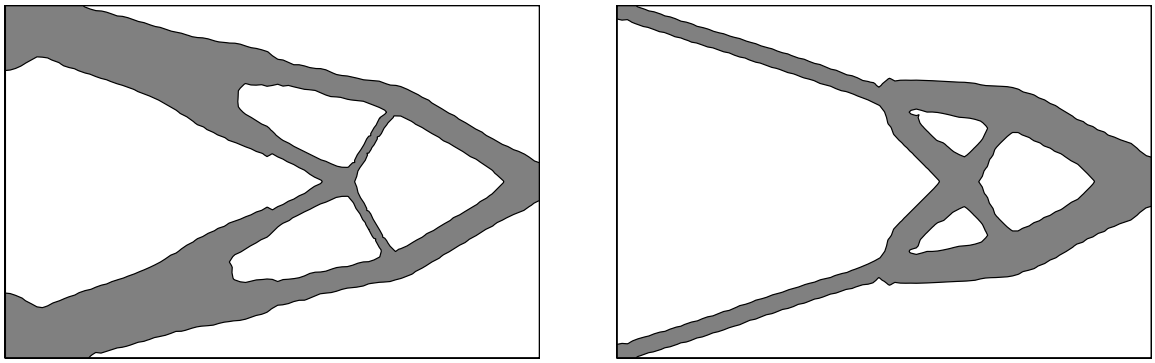

(a) Optimum of case 2, with $V_{\max}^{\text{glob}} \leq 0.3$ and $V_{\text{req}}^{\text{RH}} = 0.2$.

(b) Optimum of case 2, with $V_{\max}^{\text{glob}} \leq 0.2$ and $V_{\text{req}}^{\text{RH}} = 0.3$.

FIGURE 3.15. LSM based optima of the cantilever beam problem for case 2.

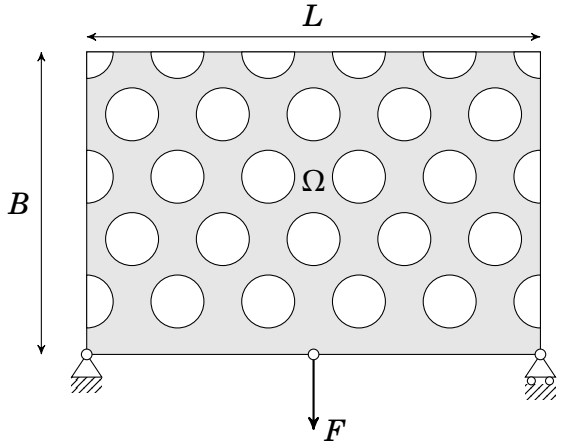

Figure 3.16: Description of the Three-Point-Bending structure problem and initial boundaries.

local constraints, as explained in Section 3.4.2. It can be seen, however, that the applied update method works as expected, showing a pre-set slope to the constraint value of 0.3 in 25 iterations (parameter N_{vol}). During this time, the objective value increases as expected and steadily optimizes towards convergence at constant volume. The amount of iterations required when the local constraints are active increases significantly, from 80 to 117 for the local inequality and equality constraints. The optimization histories show robust and stable convergence behavior.

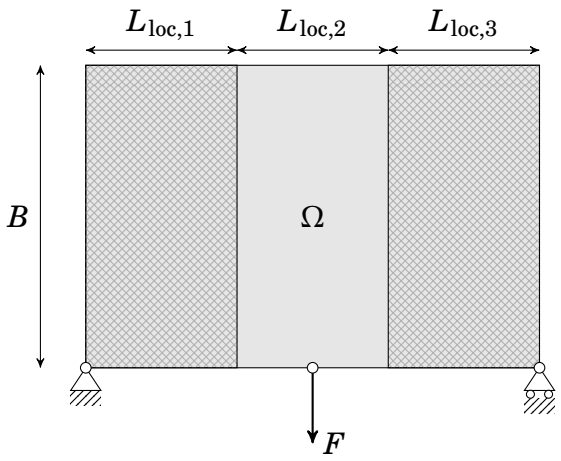

Figure 3.17: Definition of the local constraint domains for the Three-Point-Bending structure problem.

Example Two In this example, a classical Three-Point-Bending structure is solved. The general problem description is depicted in Figure 3.17. The design domain dimensions and mesh are the same as in Section 3.4.3, with $L/B = 1.515$ and 100×66 quadrilateral elements. The local volume domains are specified as: $L_{\text{loc},1} = 0.35L$, $L_{\text{loc},2} = 0.3L$ and $L_{\text{loc},3} = 0.35L$. The optimization hyperparameters are as follows: $\beta = 0.$, $R = 1.2$ and $\Delta t_{\text{fac}} = 0.9$. This setup is similar to the setup in example one. However, now boundary smoothing is included by applying the Helmholtz regularization method by setting $R = 1.2$. The bandwidth parameter h is set to 0.5 times the element side length. For the Lagrange multiplier update, the parameters are as follows: case one (secant method), $N_{\text{vol}} = 40$, case two and three (augmented method), $\tau_0 = 100$ and $\lambda_0 = 3$. The results are shown in Figure 3.19. The design domain, mesh, load case and boundary conditions are the same for all three results. The global volume constraint, $V_{\text{max}}^{\text{glob}}$, equals 0.3 for all three cases. In the first case, no local constraints are active. The second case has inequality constraints, $V_{\text{max}}^{1,3} \leq 0.2$, for sub-domains $L_{\text{loc},1}$ and $L_{\text{loc},3}$, the center domain $L_{\text{loc},2}$ is inactive. The third case has an inequality constraint, $V_{\text{max}}^{2} \leq 0.2$, on the sub-domain $L_{\text{loc},2}$, the other two sub-domains are inactive. The cases are summarized in Table 3.2.

The results show clear differences in optimal topology. The normalized optimal compliance values are presented in Table 3.2. The result of case one is a typical, well-known, optimal topology for the Three-Point-Bending structure. The normalized minimal compliance is 0.82. Case two shows the decrease in material volume in both outer local sub-domains, resulting in an increase of material in the central domain, as a result of the global volume requirement of 0.3. The normalized minimal compliance is 0.90, which

Table 3.2: Overview of example cases and normalized optimal compliance values, P_{norm}, for the Michell structure problem.

	$V_{\text{max}}^{\text{glob}}$	$V_{\text{max}}^{1,3}$	V_{max}^{2}	P_{norm}
Case 1	0.3	-	-	0.82
Case 2	0.3	0.2	-	0.9
Case 3	0.3	-	0.2	0.96

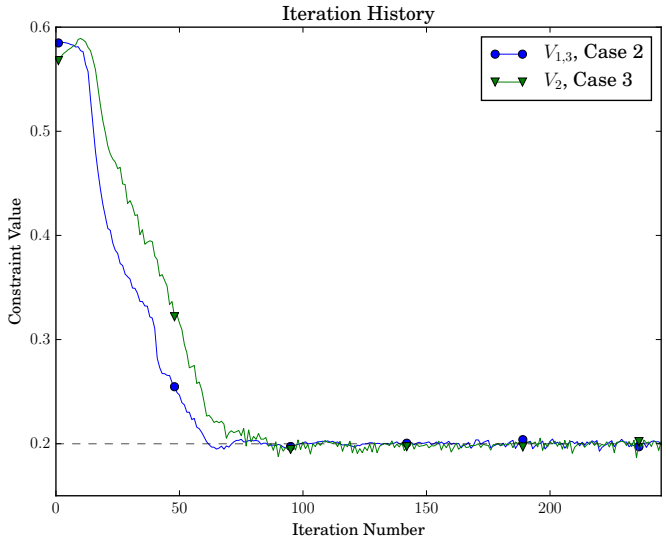

Figure 3.18: Iteration history of the local volume constraints for case 2 and 3.

is higher than in case one. This is to be expected as the same amount of material is distributed less optimal due to the introduced local constraints. The third case generated a different topology compared to case one and two to compensate for the lower allowed volume in the central sub-domain. The normalized minimal compliance is 0.96, which is higher than in both other cases. However, this is a logical consequence of the applied load case in combination with less material in the central sub-domain, due to the applied constraints. The optimization histories for these three cases are shown in Figure 3.20 and an overview of intermediate optimization results are shown in Figure 3.21. It should be noted that for the optimization with local constraints active, the convergence criteria were not met. Instead the optimization was terminated, because the pre-scribed number of iterations was reached. However, the optimization history shows reasonable stable behavior for the last 30 iterations with relative small oscillations, which is here considered as converged behavior. Similar histories can be seen for the local volume constraints, see Figure 3.18.

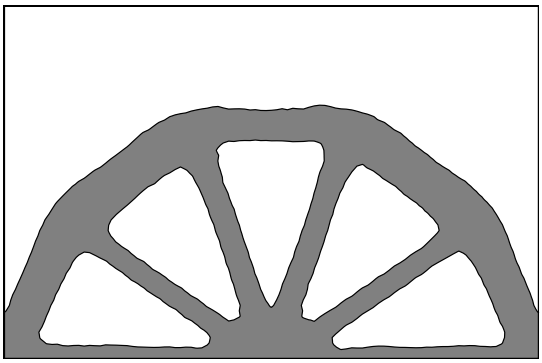

(a) Case 1: Optimum Three-Point-Bending structure with only a global constraint, $V_{\text{req}}^{\text{glob}} \leq 0.3$.

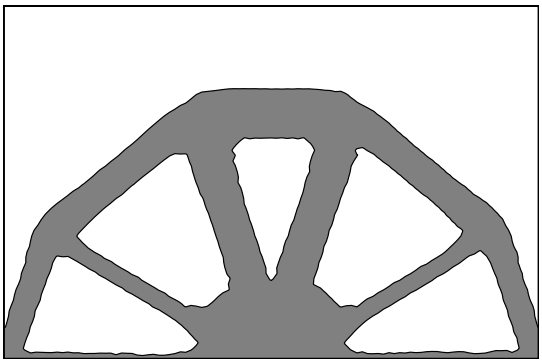

(b) Case 2: Optimum Three-Point-Bending structure with local inequality constraints, $V_{\text{req}}^{\text{N}} \leq 0.2$, for $N = 1, 3$.

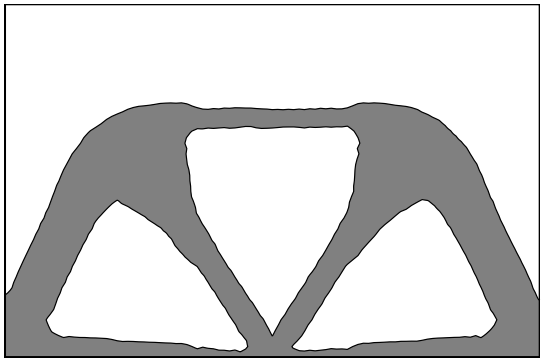

(c) Case 3: Optimum Three-Point-Bending structure with local inequality constraints, $V_{\text{req}}^{\text{N}} \leq 0.2$, for $N = 2$.

FIGURE 3.19. LSM based optima of the Three-Point-Bending structure for both, without and with local volume constraints.

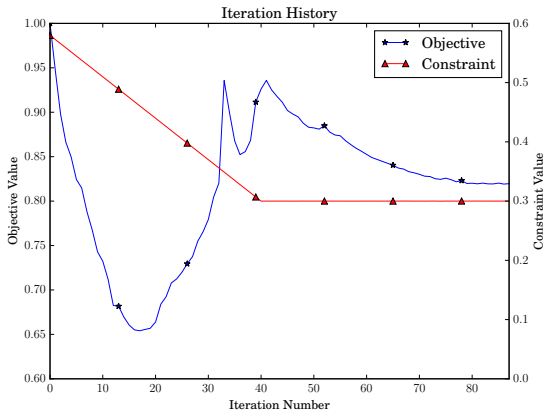

(a) Case 1.

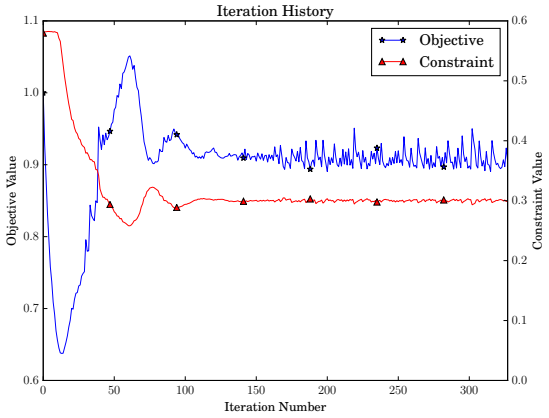

(b) Case 2.

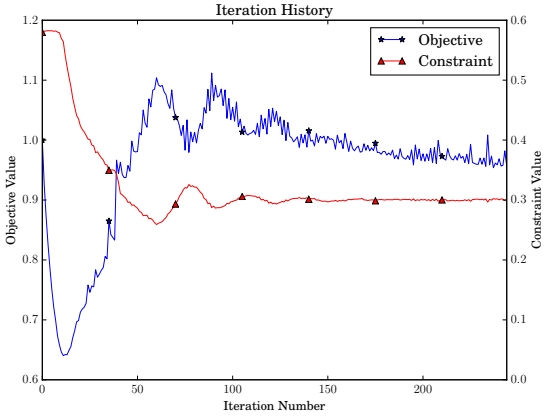

(c) Case 3.

FIGURE 3.20. Optimization histories for the cases shown in Figure 3.19. The objective value is normalized with respect to the initial design.

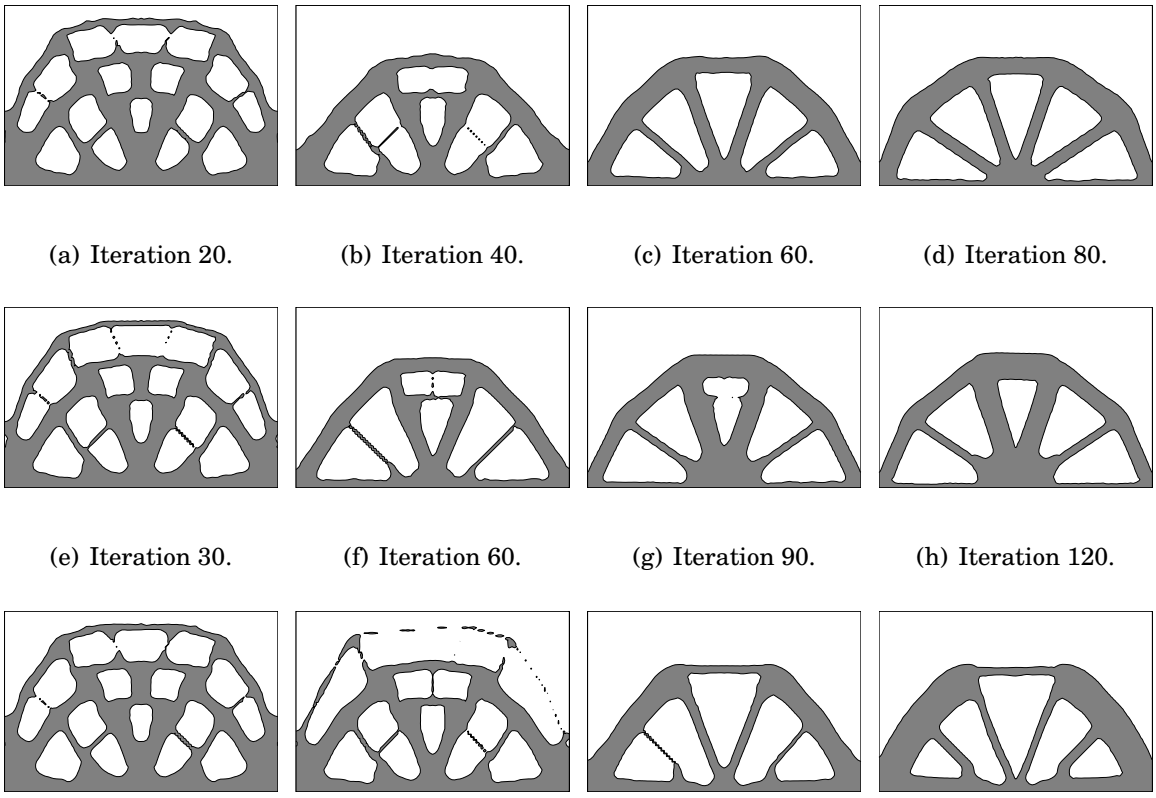

(a) Iteration 20. (b) Iteration 40. (c) Iteration 60. (d) Iteration 80.

(e) Iteration 30. (f) Iteration 60. (g) Iteration 90. (h) Iteration 120.

(i) Iteration 20. (j) Iteration 40. (k) Iteration 60. (l) Iteration 80.

FIGURE 3.21. LSM iteration history for the Three-Point-Bending design problem; case 1 (a to d), case 2 (e to h) and case 3 (i to l).

3.5 Mapping Approach from 2D to 3D

To determine if the optimal load paths work in the 3D initial vehicle structure, the 2D load paths are transformed back into the 3D simplified vehicle structure, presented in Sections 3.1 and 3.2. Information on the out-of-plane behavior of the 2D load paths is absent, therefore only simple transformations to 3D are performed. Even so, this transformation is only possible when some important assumptions are made:

- Structure consists of fixed thickness thin walls.
- Cross-sectional shape is fixed: the general cross-sectional shape remains fixed, for instance square or ellipsoid.
- Cross-sectional height is fixed: the new load bearing structure has a fixed height.
- Perfect connections between structure elements: joints, attachments and bonds are assumed perfect.

The transformation from 2D to 3D is done in several stages; 1) Extracting the level-set iso-contour, 2) Smoothing of the level-set iso-contour, 3) parsing the iso-contour to a FEM pre-processing tool, 4) meshing of the enclosed geometry and 5) extruding to 3D structure. The process will be explained in detail in the next paragraphs.

Smoothing

The initial level-set iso-contour can be rough, with high local curvatures and possibly local artifacts, such as 'bubbles'. Artifacts and/or non-smooth boundaries will later result in an inferior mesh quality and geometry for the 3D structure. This will have a significant effect on the structural stability during the crash simulations. The resulting structural instability is an unwanted side-effect from the 2D to 3D transformation and has very little to do with the optimal structures derived by the LSM. It should therefore be mitigated or reduced significantly.

There are several techniques available to control the amount of curvature on the level-set boundary during optimization, perimeter control among others. However, these techniques restrain the shape optimization. Therefore implementing a smoothing algorithm in a later stage has some benefits over applying shape constraints during optimization.

The smoothing algorithm used here consists of a maximum of two processes. The main process is to smooth the zero level-set iso-contour. The optional second process is

used to remove any 'bubbles' that might have occurred during the LSM optimization. These 'bubbles' are artifacts created by areas where the LSF varies around the zero level-set boundary, resulting in local multiple small iso-contours. First the main process is explained.

The quadrilateral mesh on which the LSF is discretized is transformed into a triangular mesh by splitting the quadrilaterals. We can now use an existing algorithm to generate an iso-contour with a bi-linear spline description. We extract the points describing the iso-contour path and create a new bi-linear spline over these points. By creating this new spline, we have control over its smoothness. The smoothness parameter controls the amount of local curvature over the spline path; a higher parameter value creates a spline with a lower maximum local curvature. The bi-linear spline description of the iso-contour is also necessary to transfer the optimized geometry to a CAD program.

The optional second process is applied to remove the 'bubble'-like artifacts and can be applied on top of the main smoothing process. This process is a pre-processing before the main smoothing step explained above. First, an offset is added to the discrete LSF values:

$$\phi_\Gamma(\vec{x}) = \phi(\vec{x}) + \Gamma \tag{3.32}$$

where $\phi(\vec{x})$ is the original LSF, Γ is the offset value and $\phi_\Gamma(\vec{x})$ is the temporary new LSF. The original LSF should be equal to the signed distance function before applying this smoothing step:

$$\left\|\nabla\phi(\vec{x})\right\| = 1. \tag{3.33}$$

With a negative offset value, Γ, the iso-contour portraying the new zero level-set of $\phi_\Gamma(\vec{x})$ is effectively expanded outward into the void domain, equivalently to having a boundary normal velocity, V_N, being constant everywhere on the boundary. The signed distance property of the LSF ensures that the level set boundary contracts or expands equally over the total boundary. The effect is that the material volume is increased and that all small artifacts around the original boundary disappear. The level of artifact removal can be determined by increasing the value for Γ. However, the larger this value, the more of the original contour is lost and at very high values new topologies may be created. For instance, at sufficiently large values of Γ boundaries could merge and distinct topologies may get lost. This over-crossing of geometrical features can cause a significant deviation of the optimal topological layout. Therefore, care should be taken in determining an adequate value for Γ. At this stage the main smoothing procedure is applied to smooth the new zero level-set iso-contour. The new LSF is re-initialized as an SDF, as explained in Section 2.1. The smoothing procedure changes the shape of the boundary, therefore

the re-initialization procedure is needed to ensure the new level set values have the signed distance property. The re-initialization makes sure the artifacts are removed. Then, the offset procedure can be applied again in reverse, with an offset value $-\Gamma$. The new LSF has a material volume close to the original, but all artifacts are removed and the boundary is smoothed.

Applying these smoothing procedures makes the original level-set boundary better suited for structural implementation. However, the smoothing procedures also modify slightly the topology of the optimum load paths. This may also change the volume by a small amount, leading to a possible failing of the volume constraint or constraints. This could be mitigated by iterating over the second step of the offset procedure, reverse offset, updating Γ until the same global volume is achieved as at optimum. This would not work with multiple volume constraints however. An overview of the smoothing steps can be seen in Figure 3.22.

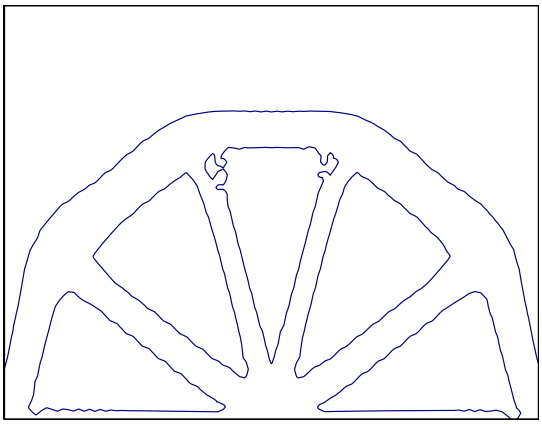

(a) Initial zero level-set with optimization artifacts visible around the inner top and outer bottom corners.

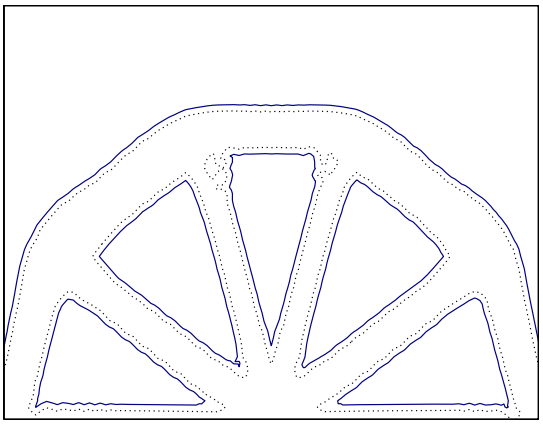

(b) First step: the initial zero level-set (dotted line) with an added offset, removing the artifacts and increasing the volume.

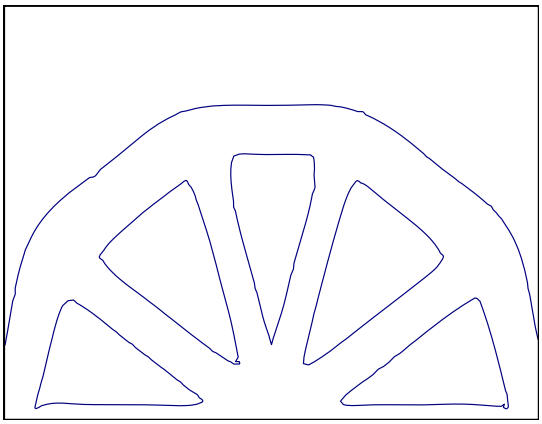

(c) Second step: the zero level-set with offset smoothed with the spline based method. The LSF shown is then re-initialized.

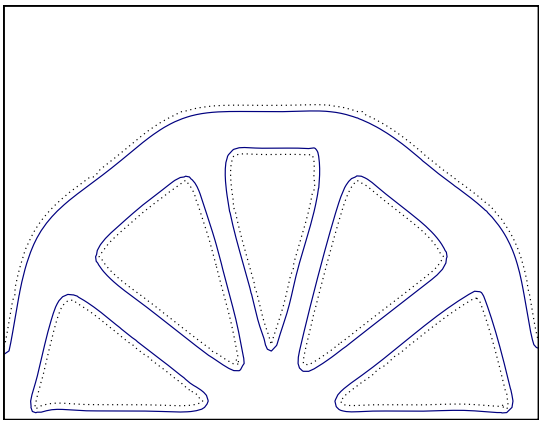

(d) Third step: Inverse offset of the smoothed zero level-set from step two (dotted line).

FIGURE 3.22. Smoothing process applied on Three-Point-Bending optimization result.

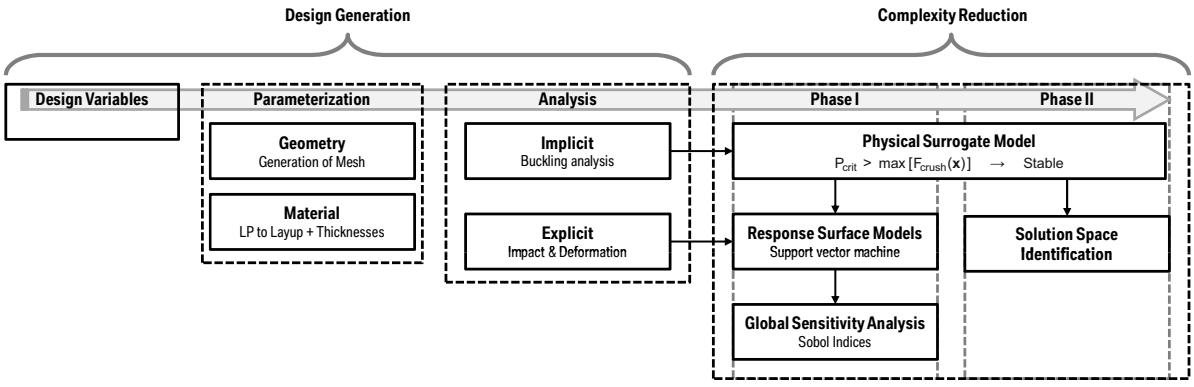

FIGURE 3.23. Diagram of the complexity reduction work-flow.

3.6 Complexity Reduction

The content of this section was partially published by the author in the journal of Composite Structures. [46]

The introduction of advanced composite materials into the design of crashworthy automotive structures increases the complexity of the already complex design development. The number of design parameters, the complex non-linear mechanical behavior and the high computational costs are compelling arguments for complexity reduction. In Section 1.4 more details are given.

In this section, a new systematic approach to reduce design complexity is introduced. This is the second part of the proposed design work-flow, as presented at the beginning of this Chapter 3. The method touches on the three complexity increasing factors as discussed in the introduction 1.4; the high number of design variables, mechanical behavior and computational cost. The approach consists of a novel work-flow, where the complexity is reduced in two stages. In the first stage, a parameter importance hierarchy is derived. In a second stage, a Solution Space Identification (SSI) method is used, adapted from the work proposed in [34, 38]. Both stages are designed to reduce the design space complexity. On top of this, a Physical Surrogate Model (PSM) is developed to approximate a Limit State Function (LiSF) that is applied in both stages to reduce the mechanical behavior complexity and increase the computational efficiency.

3.6.1 Methodology

The approach presented here is shown in Figure 3.23 and follows two major stages: The Design Generation stage and the Complexity Reduction stage. The work-flow is implemented using the optimization software NOESIS OPTIMUS [1].

In the design generation stage, a set of parameters is chosen as design variables for the problem to be considered. These parameters can be divided into geometry and material variables. Values for the parameters are parsed to a geometry modeler and a material handler. In this research SFE CONCEPT [29, 95] is used as the geometry modeler. With SFE CONCEPT a structure is designed with parameterized geometry; by changing a parameter value, the geometry of the structure is changed and all dependent structural parts as well. The parameter variables can be assigned a value by other programs, for example optimization algorithms. By running SFE CONCEPT in batch modus and parsing the updated parameter values, the structure can be adapted. SFE CONCEPT can do the same for many material properties. When a numerical structural analysis is required in the work-flow, as is the case in this research, SFE CONCEPT can generate a FE mesh compatible to various FEM solvers. The meshed design and material parameters are parsed in this work to an ABAQUS/EXPLICIT template input deck for numerical analysis. CZONE, see Section 2.3, is used to simulate the progressive crushing behavior in the crush-front of the composite structure. A separate FE model is generated for the PSM approach. Here ABAQUS/IMPLICIT is used for the buckling analyses. Both the explicit and implicit analyses can be run in parallel or one of them can be omitted. The results are extracted by Python classes and stored in data files which are parsed back to OPTIMUS. The crash-worthiness is derived from the explicit numerical analyses. The responses of interest are the maximum intrusion of the barrier into the structure, $\delta_{\max}$, and the total weight of the structure, M_{struc}. This weight can conveniently be directly calculated from the parameters that define the geometry and the laminate thicknesses, i.e. $M = M(\mathbf{\Phi})$ where $\mathbf{\Phi}$ equals the set of available parameters.

The second stage, the complexity reduction, forms the main part of this method and will be explained in the following sections.

Implementation of Lamination Parameters In Section 2.2 the background of LP is explained.

LPs considerably simplify the modeling of FRP composites and assist in decreasing the complexity of the whole design process. The answer of an FRP composite structure or laminate is a function of the stiffness matrices of the laminates, usually derived with the

CLT. The main challenge that comes from using the CLT to describe the laminate is the high number of required variables. Furthermore, the ply orientations are usually chosen from a set of available orientations, which leads to variables having partially discrete properties. Alternatively, the LPs can be used as design variables that entirely define the stiffness of the laminate properties. As is customary and good engineering practice, the laminates used in this project are assumed to be balanced and symmetric, resulting in four from the total of 12 possible LPs. The LP set then consists of $V_{i\boldsymbol{A}}$ and $V_{i\boldsymbol{D}}$ with $i = 1,3$, for membrane and bending stiffness respectively.

The LPs $V_{i\boldsymbol{D}}$ are omitted as laminates in a traditional vehicle design, designed for crash absorption, are predominantly loaded in-plane. The comparatively large closed cross-sections from the normally used tubular construction provide the bending resistance. For future applications, where the bending stiffness of the laminate has a greater influence on the structural reaction, LP $V_{i\boldsymbol{D}}$ can and should be included. The balanced and symmetric condition decreases the achievable range of LP to [51, 75]:

$$\begin{aligned} 2V_{1\boldsymbol{A}}^2 - 1 &\leq V_{3\boldsymbol{A}}; \\ -1 \leq V_{i\boldsymbol{A}} &\leq 1 \quad (i = 1;3). \end{aligned} \tag{3.34}$$

The domain described by Equation (3.34) is shown in Figure 3.24. In addition, due to manufacturing constraints, the number of available ply orientations are constrained to $\pm 45°$, $0°$ and $90°$. When using the CLT approach, this leads to discrete variables, which may cause problems when running optimization algorithms. However, for LPs this orientation constraint is handled by constraining the feasible LP domain from Equation (3.34) to:

$$\begin{aligned} 2V_{1\boldsymbol{A}} - 1 &\leq V_{3\boldsymbol{A}}; \\ -1 \leq V_{i\boldsymbol{A}} &\leq 1 \quad (i = 1;3). \end{aligned} \tag{3.35}$$

The LPs $V_{1\boldsymbol{A}}$ and $V_{3\boldsymbol{A}}$ are used as design variables. It is preferable to directly translate the LPs to stiffness information for use in the FE analyses. However, the material models used in ABAQUS and CZONE require specific layup information. Therefore, the LPs need to be translated into a laminate layup design with a certain stacking sequence and layer orientations. This process can be complex, as there is in theory an infinite number of possible layups that fit a certain set of LPs. This problem has three possible variables: (1) the amount of layers, (2) the orientation of a layer, and (3) the thickness of a layer. Depending on the application, different methods are suitable. If the application is a real world laminate layup design, the thickness of each layer is usually kept constant, defined by the fabric specification. The total laminate thickness together with the ply orientations

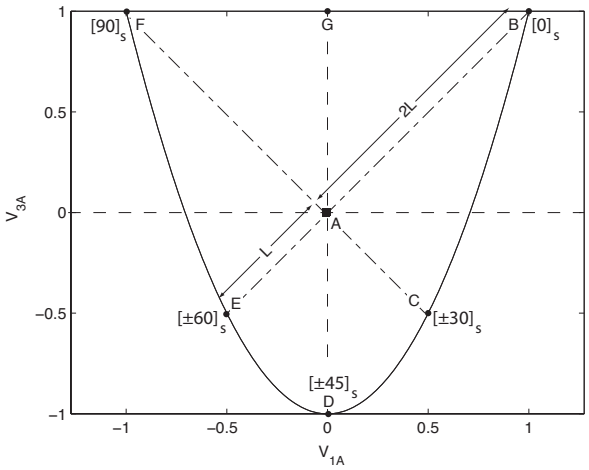

FIGURE 3.24. Miki diagram of feasible region for LPs for balanced and symmetric laminates, [51].

determine the final stiffness properties. This leads to an optimization problem where the objective is to match the LPs of the trail laminate layup to the desired LPs. This can be cumbersome and an exact fit may not exist. This could lead to discontinuity problems in the proposed work-flow.

If the application, however, is a material definition for an FEM solver the layup does not have to be physically realistic. Hence, a method is developed here to derive a laminate layup definition that exactly matches the desired LPs.

The method uses a variable thickness distribution of the plies in a template laminate design. This template laminate is established first, a convention layup is chosen:

$$\left[\pm 45^\circ, 0^\circ, 90^\circ, \pm 45^\circ, 0^\circ, 90^\circ\right]_s \tag{3.36}$$

The combination of a thickness distribution and a laminate template is possible, as laminate bending stiffness is not considered a design variable. Naturally, any template can be chosen, important is that all available ply orientations are included. The proportional contributions p_θ with $\theta = 45^\circ, 0^\circ, 90^\circ$ of each ply is determined by the LPs. The Miki diagram, as shown for example in Figure 3.24, is used to derive these proportional contributions. The Miki diagram gives the feasible domain of the LPs $V_{1\boldsymbol{A}}$ and $V_{3\boldsymbol{A}}$ and how they relate to a certain laminate layup. For instance, when $(V_1, V_3) = (1, 1)$ the only possible laminate would consist of only 0° plies. Point G is positioned exactly half way between the 90° and 0° ply orientations, meaning that $(V_1, V_3) = (0, 1)$ will correspond to a layup consisting of equal parts 90° and 0° ply orientations. This physical perception

of the relation between LPs and layup designs is interesting for parameterization of composite laminate properties. In this case, where only the ±45°, 0° and 90° orientations are available, the relation between the LPs and the proportionality contributions p_θ can be derived as shown in Equation (3.37).

$$\begin{aligned} p_{45} &= -\frac{V_3}{2}+\frac{1}{2}; \\ p_0 &= \frac{V_1}{2}+\frac{V_3}{4}+\frac{1}{4}; \\ p_{90} &= -\frac{V_1}{2}+\frac{V_3}{4}+\frac{1}{4}. \end{aligned} \tag{3.37}$$

The variable thickness for each ply in the template layup from Equation (3.36) is determined by deriving their respective proportions as follows:

$$t_\theta = t_{\text{tot}} p_\theta. \tag{3.38}$$

The complete thickness distribution is then defined as follows:

$$\frac{1}{4}[t_{45}, t_0, t_{90}, t_{45}, t_0, t_{90}]_s\,. \tag{3.39}$$

Implementation of the Limit State Function The proposed method for complexity reduction uses the implementation of a Limit State Function (LiSF), as used for example by Stocki et al. in their reliability analysis of a crashed thin-walled S-Rail [99]. The LiSF is a design method that is often used in structural engineering. It is applied where a system has a certain capacity or resistance and on the other hand is subjected to some sort of demand or loading. If at a certain point the demand or loading exceeds the capacity or resistance of the system, the system reaches its limit state and fails. Hence, the system does not display its intended behavior. The transition between accepted and unwanted behavior (also denoted as “system instability failure” or “system instability”) is characterized by the LiSF.

The LiSF is implemented here as follows. The limit state is expressed as the point where the composite structure transitions from stable progressive crush behavior to a global structural instability, for example buckling, and collapses. This is relevant for the crash-worthiness of FRP composite structures: a stable progressive crush front is essential for adequate energy absorption. The initiation and progression of a crush front and the crush-stress generate a load on the structure. If the structure is unable to provide

enough stability to support the peak and crush load, the structure is unable to absorb the required energy. Structural stability is therefore used to describe the limit state and is here defined as follows:

$$\begin{aligned} G(R,S) &= R - S \\ \text{with:} \quad & G(R,S) > 1: \quad \text{stable} \\ & G(R,S) < 1: \quad \text{unstable} \end{aligned} \tag{3.40}$$

where G is the LiSF, R is the resistance of the system and S is the load on the system. It should be emphasized, that in contrast to most other applications found in literature, the LiSF is not used in this research for reliability analysis. Rather it is used for variable screening and the corresponding complexity reduction as a preparation for optimization. Normally, the evaluation of an LiSF is very complex, different examples of this were discussed in section 1.4. Hence, a modeling based on physical surrogates is developed in order to reduce the complexity related to computational effort and the number of parameters. The Physical Surrogate solution is proposed next.

Implementation of the Physical Surrogate A model is needed to implement the LiSF method. Here the concept of a Physical Surrogate Model (PSM) is proposed to model the behavior, or more specific, the structural stability of the structure. The LiSF differentiates between two distinct structural behaviors, therefore the proposed model should provide this information. Commonly, Response Surface Approximation (RSA) techniques are used to approximate the LiSF for specified structural behaviors, see for example research by Kurtaran et al., Gu et al., Yang et al. [40, 65, 118] and the previously mentioned research by Stocki et al. [99]. Here, a method is proposed where a simplified simulation model is used to directly approximate the structural stability of a certain design, instead of using the RSA technique. The term “Physical surrogate modeling” is chosen, because a physical model is used to estimate the structural stability. Another reason the term is introduced is to avoid confusion with RSA methods. The term PSM underlines that the surrogate represents part of the physical characteristics of the assessed structure.

It was mentioned before that a progressive crush front is desirable and that global instability should be avoided. It is assumed that a linear elastic buckling analysis can be used to determine the onset of a primary structural instability. A perfect assessment is not necessary, as the PSM used in conjunction with the LiSF is used to establish a Parameter Hierarchy (explained in the next paragraph). Remember, the goal is to

reduce the complexity of the crash-worthiness optimization problem. For establishing a hierarchy of parameters or for filtering solution spaces (explained later in this Section), it can be accepted that the PSM only covers partially the actual investigated structural behavior.

The assumption is that a linear elastic buckling analysis can give an adequate prediction of the impact force threshold at which the structure becomes unstable. The underlining thought is that local or global buckling weakens the structure, while stresses are not reduced. This in turn results in collapse and eventually local failure of the laminate.

A typical crash load-case is a component, which is impacted by or on a rigid flat surface, see for example Figure 3.25. The PSM for use in the LiSF is implemented as follows. The rigid surface is replaced by a unit-force perturbation force in the same direction and location of the impact. Then, the critical buckling load P_{crit} is derived by the static linear buckling analysis. This P_{crit} is compared to the crush force F_{crush} of the composite component. The crush force can be analytically derived. This is important, as an explicit numerical FE analysis would defeat the purpose of this method in terms of computational efficiency. The procedure to analytically derive the crush force is explained later. The comparison is illustrated in Equation (3.41). If the critical buckling load is higher than the approximated crush load, the structure is deemed stable and behavior is as intended.

$$P_{\text{crit}} > \max[F_{\text{crush}}(\mathbf{x})] \quad \rightarrow \quad \text{Stable} \tag{3.41}$$

where $\mathbf{x}$ stands for the cross-sectional geometric properties of the impacted component. The first buckling mode and corresponding eigenvalue are taken as the critical buckling mode, subsequently the corresponding critical buckling force P_{crit} is calculated.

Using Equation (3.41) to modify the general description of the LiSF in Equation (3.40), results in:

$$G(P_{\text{crit}}, F_{\text{crush}}(\mathbf{x})) = P_{\text{crit}} - \max[F_{\text{crush}}(\mathbf{x})] \tag{3.42}$$

As mentioned earlier, the crush force F_{crush} can be analytically derived. The material specific crush stress data, determined a priori for the CZONE simulation model, is used to calculate F_{crush}. The crush stress is normally given in tabular form, with specific crush stresses for corresponding material orientation with respect to the impacting surface. The crush force can be interpolated from this data for a specific cross-sectional area parallel to the impact surface or for projected cross-sectional area. Figure 3.25 shows how the projected cross-sectional area is determined. The crush stress $\overline{\sigma}_{\text{crush}}$ can be

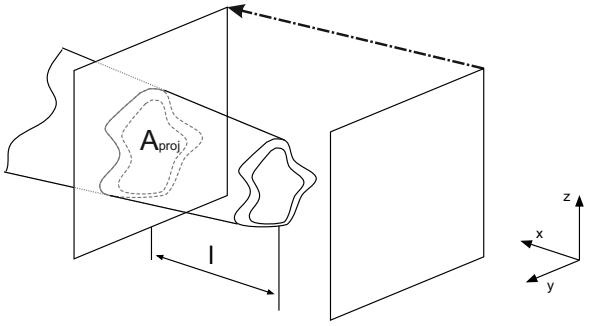

Figure 3.25: Typical load case for a composite specimen, impacted by a rigid surface. Determination of the impact surface projected cross-sectional area on the crushable structure.

calculated by interpolating the tabulated crush stress with laminate layup definition, see reference [76].

Implementation of the parameter importance hierarchy In Section 1.4.1, the use of an importance hierarchy is discussed. This method can help reducing the number of parameters in a structural optimization problem by giving an objective and mathematically derived influence of each parameter relative to the others. Important information might be lost if a small set of parameters is selected beforehand for a certain optimization problem, which is commonly the case. Therefore deriving an importance hierarchy can significantly reduce the complexity of the problem allowing a flexible consideration of parameters. The implementation of such a method in the proposed work-flow is presented here.

For the accurate derivation of the importance of each parameter a Global Sensitivity Analysis (SA) is performed. This is done by calculating the variance-based importance measures of the input variables with respect to the required outputs, for instance the maximum deformation and mass responses. The variational analysis is performed with the Sobol decomposition method [97]. This method derives the Sobol indices, which are in essence the global sensitivities of the parameters. In other words, the Sobol indices show the relative importance of the individual input parameters over the entire design domain, both in first and higher order dependencies. The exact derivation is well-documented and therefore not necessary to repeat here, a thorough explanation is given in the research by Arwade et al. [9].

For a practical problem, such as the structural crash-worthiness optimization problem in this research, numerical integration is necessary to obtain the Sobol indices, as

an exact form of the response is not available. On often used method is Monte Carlo Sampling (MCS). The MCS is used to approximate the integrals. However, this method requires a large amount of samples for an accurate approximation. Using design experiments for the MCS integration would require too much computational effort. Therefore a RSA is derived on which the MCS integration can be performed. Many RSA methods are available and detailed explanations of each one with their positives and negatives can easily be found in literature. In this research, a Support Vector Machine (SVM) method is used after comparing it to other candidates. It proved to provide good correlation for this type of crash simulation with composite materials in combination with CZONE analysis.

The Sobol indices provide an importance measure for the respective design parameters. In this research, the total Sobol indices are used, as they also cover higher order dependencies between parameters.

The design generation stage in the presented work-flow is used to execute a Design of Experiments (DoE) as the basis for the RSA. MCS is used to generate the DoE. The relatively simple Monte Carlo (MC) method is chosen here, because of its high flexibility. Other, more advanced methods, such as Latin Hypercube and Full Factorial, can provide a better, i.e. more uncorrelated, dispersion of samples. However, they also do not allow for the addition of samples at a later stage. The MCS also is insensitive to failed samples, which can be easily removed without making the MCS unusable. For a simulation environment with the presented crash-worthiness design problem, a relatively large number of simulations fails, for instance due to numerical issues. Furthermore, it should be assured that the feasible domain for the LP is not violated, see Figure 3.24 and Equation (3.35). To ensure that the DoE generates samples within these bounds, dependent constraints are set on the LP bounds. The method for enforcing these bounds should not interfere with the uniform random sampling distribution, or false correlations might occur. Therefore, each time the MC DoE picks a sample outside the feasible domain, the sample is disregarded and a new sample is tried in its place.

With the generated DoE, an SVM-based RSA is made for each desired response. In the case of the presented problem, the maximum deformation and structural mass are chosen. In first instance, the RSA for the maximum deformation response shows both system behaviors, stable and unstable, in unknown quantities. The approximation is not told how to differentiate between the two behaviors and therefore considers them the same. This results in some interesting sensitivities. If the dominant structural behavior within the design space of the DoE is unstable, the Sobol derived parameter hierarchy will prefer the parameters influencing that behavior. It is therefore essential to help

the method differentiate between these behaviors. This is done with the help of the previously presented implementation of the PSM and LiSF. The PSM is used to filter the samples of the DoE and create a second RSA, which is based on this filtered design space. Subsequently, the Sobol analysis is performed on this filtered RSA as well. The result is three hierarchies, one total and two filtered hierarchies for the chosen responses. The comparison of the hierarchies provides important information on which parameters should be kept and which could potentially be omitted in the design problem formation.

In a final step, a relatively simple guide line is used to determine which design parameters are kept. This guide line is as follow: a parameter hierarchy X is built, which sums for each response the total Sobol indices to a certain minimal total influence factor. This minimum is chosen such that a significant part of the solution space is represented. A value between 0.7 and 1.0 is considered appropriate. Finally, the parameters are compared between the unfiltered and PSM filtered RSMs and a final reduced design parameter set is chosen.

Implementation of the Solution Space Identification method At this point in the complexity reduction work-flow the design parameter hierarchy is known and a reduced set of parameters is chosen. Now, a method is presented to reduce the problem complexity based on determination of the bounds for this reduced set of parameters.

Zimmermann and Graff [38, 39] have developed the Solution Space Identification (SSI) method for maximizing the volume of an axis-parallel hyper-box in high-dimensional space under the constraint that the objective values of all enclosed designs are below a given threshold. Here, it is proposed to use the limit state formulation and the PSM approximation in combination with the SSI method, in order to find a design space that predominantly shows the desired stable structural behavior of the component. For clarity, the theory behind the SSI method is explained first.

Let $f(\mathbf{x})$ be a function with design space $\Omega_{\mathrm{DS}} \subseteq \mathbb{R}^d$. Here $\hat{\mathbf{x}}$ and $\check{\mathbf{x}}$ are the upper and lower bounds for all design points $\mathbf{x}$, where $\hat{x}_i \geq \check{x}_i$ for $i = 1 \ldots d$. Then, the volume of the hyper-box $\Omega_{\mathrm{box}} = \Omega_{\mathrm{box}}(\hat{\mathbf{x}}, \check{\mathbf{x}})$ is denoted as $\mu(\Omega_{\mathrm{box}})$ and f_c is some critical value.

The constrained optimization problem P can be defined as:

$$\left.\begin{array}{l} \text{find } \hat{\mathbf{x}}, \check{\mathbf{x}} \in \Omega_{\mathrm{DS}} \text{ with } \hat{x}_i \geq \check{x}_i, \text{for } i = 1 \ldots d \\ \text{such that } \mu(\Omega_{\mathrm{box}}) \rightarrow \max, \text{ s.t. } f(\mathbf{x}) \leq f_c \, \forall \mathbf{x} \in \Omega_{\mathrm{box}} \end{array}\right\} (P). \tag{3.43}$$

The algorithm only requires function evaluations and can therefore be considered as non-intrusive.

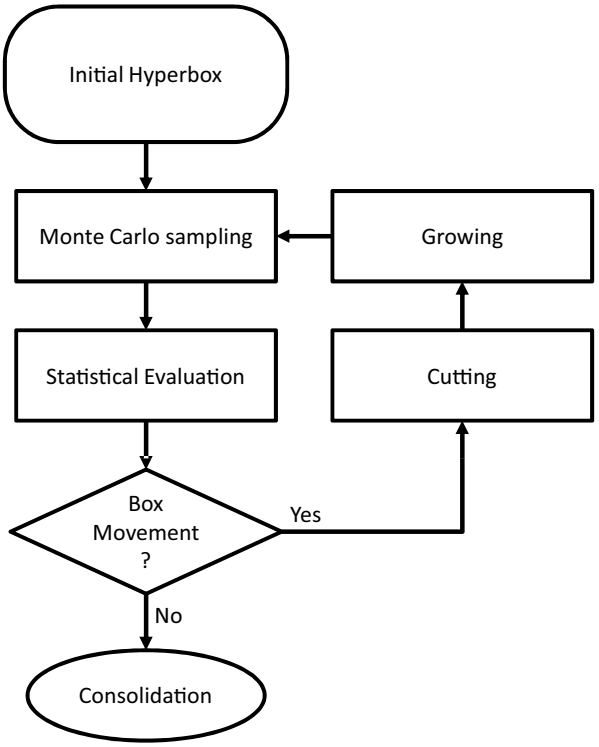

FIGURE 3.26. Schematic representation of the SSI method phase 1, exploration.

The algorithm uses differential evolution [101] to identify a design, $\mathbf{x}$, which fulfils the inequality $f(\mathbf{x}) \leq f_x$. When this design is found, an initial or candidate hyper-box, Ω_{cand}, is defined around this design. This entails the start of the algorithm, which consists of two phases: 1) Exploration and, 2) Consolidation.

The exploration phase is shown schematically in Figure 3.26. In the exploration phase, four steps are recognizable: Sampling, Evaluation, Cutting and Growing. In the Sampling step, the fraction of "good" designs within the generated population $\mathbf{x}_j$, is calculated. Good designs are those designs which fulfil $f(\mathbf{x}_j) \leq f_c$, the fraction $\tilde{\alpha}$ is determined by the ratio N_g/N of N_g good designs and total number N samples. With the fraction known, the Bayesian 95%-confidence interval is calculated for $\tilde{\alpha}$.

During the cutting step, the candidate hyper-box Ω_{cand} is shrunk such that only good points remain in the new hyper-box. To find the biggest new candidate hyper-box, a fast cutting algorithm is used. In the growing step, the hyper-box is modified such that it can evolve towards regions with increasing hyper-box size in connection with the cutting

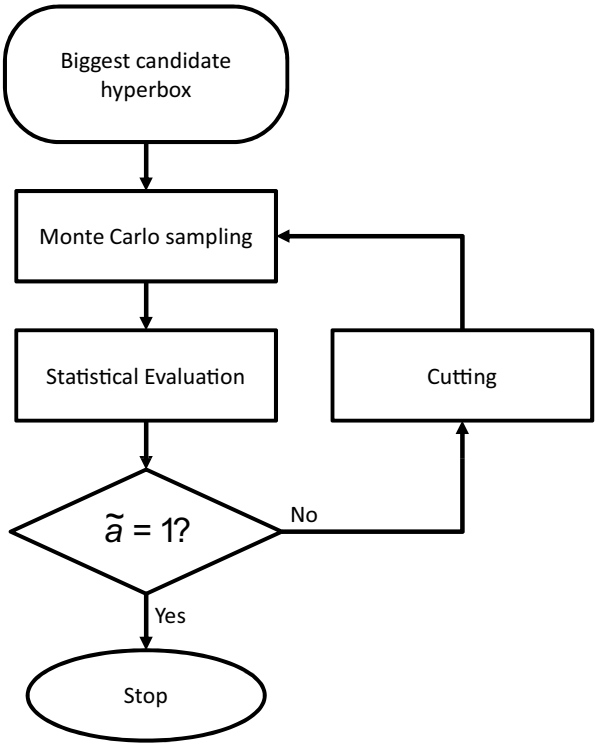

Figure 3.27: Schematic representation of the SSI method phase 2, consolidation.

step. This is done by modifying the boundaries with a certain growth factor $\beta^{(k)}$:

$$\begin{aligned} [\check{x}_i]^{(k+1)} &:= [\check{x}_i]^{(k)} - \beta^{(k)} \left([\hat{x}_i]^{(k)} - [\check{x}_i]^{(k)} \right) \quad \forall\, i = 1 \ldots d; \\ [\hat{x}_i]^{(k+1)} &:= [\hat{x}_i]^{(k)} + \beta^{(k)} \left([\hat{x}_i]^{(k)} - [\check{x}_i]^{(k)} \right) \quad \forall\, i = 1 \ldots d. \end{aligned} \tag{3.44}$$

The growth factor $\beta^{(k+1)}$ is determined based on the fraction $\tilde{a}$, such that good design points will be included in the new hyper-box candidate. The growing hyper-box and subsequent cutting moves the hyper-box to areas of increasing hyper-box size. This continues until the hyper-box is not growing or moving any more, the algorithm then switches to the consolidation phase.

The consolidation phase is shown schematically in Figure 3.27. In the consolidation phase, three steps are present: Sampling, Evaluation and Cutting. They are in essence the same as in the Exploration phase with the exception that the candidate hyper-box will not grow or move. Therefore the consolidation phase will decrease the candidate hyper-box size by re-sampling and cutting until the fraction $\tilde{a}$ is equal to one and the probability that Ω_{cand} only contains good designs is high enough.

The goal of the implementation of the SSI method is to reduce further the complexity of the optimization problem. This is done by finding new bounds for the remaining design

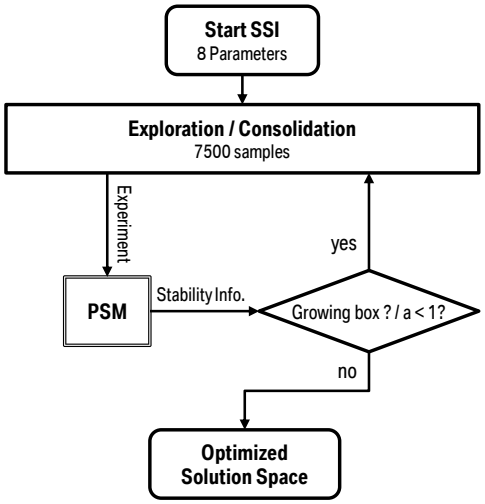

(a) Flow diagram of phase 2 of the complexity reduction method; identifying the optimal solution space. This diagram is a simplification of the processes shown in Figures 3.26 & 3.27, but with the PSM method integrated. A detailed view of the PSM box can be found in (b).

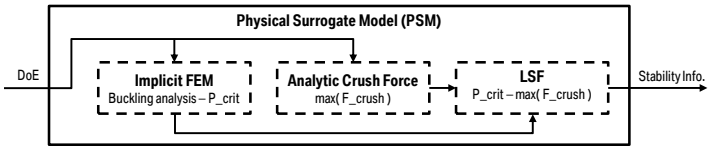

(b) The PSM process in more detail.

FIGURE 3.28. Flow diagrams explaining the work-flow of the SSI implementation.

parameters. The parameters after the parameter reduction are used.

The PSM is used in the SSI method to approximate the LiSF and implemented in the software CLEARVU [3]. The work-flow of the presented implementation is shown in Figure 3.28. The LiSF function from Equation (3.42) is used as the constraint equation in the SSI method. The constraint is then set as:

$$G(P_{\text{crit}}, F_{\text{crush}}) > 0. \tag{3.45}$$

This way, the method will try to find a solution space, represented with a hyper-box, that holds within its domain the largest amount of feasible, stable designs. The complexity of the SSI method, and with that the computational efficiency, is strongly reduced with a lower parameter number and the use of the computationally efficient PSM. The other, fixed parameters, should be set to their nominal values.

Result and benefit of the complexity reduction At this point the original design problem is significantly reduced in complexity. The optimization of the problem is less difficult, because:

1. Only the most influential parameters are used as the optimization variables. Less variables increases the convergence speed and increases the chance to find a global optimum.

2. The variable bounds and thereby the design domain of the problem will mostly consist of feasible, stable design. This increases the stability of the optimization and increases again the convergence speed and chance of finding a global optimum.

The application of the method on an S-rail problem and the structural optimization in the application chapter, Section 4.2, justify the two points made above.

CHAPTER 4

Application and Test of Methods

In this chapter, the methods presented previously are applied. Two main applications are in focus. First is the optimization of the CFRP composite support structure for the impact loaded front architecture of a novel vehicle design. Second is the optimization of an S-Rail before and after the complexity reduction.

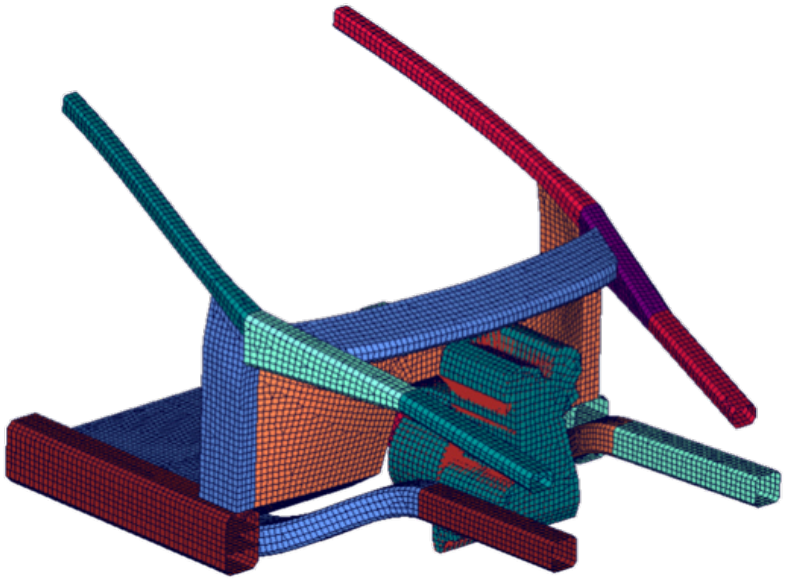

FIGURE 4.1. Early phase design of a novel CFRP composite vehicle front architecture. All parts are made of CFRP composites, except the motor

4.1 Optimization of Composite Vehicle for Crash

In Figure 4.1, an early phase design of a novel CFRP composite vehicle front architecture is introduced. The goal of this exercise is to optimize a composite supportive structure that enables a crash-worthy front vehicle design for two typical crash load cases. The load cases are a full overlap frontal impact on a rigid wall perpendicular to the impact and an impact on a rigid 30° oblique wall. These are both load-cases that are part of the regulatory requirements in the USA and part of the FMVSS208 regulations.

4.1.1 Mapping to the 2D Design Domain

The optimization work-flow presented in Chapter 3, Sections 3.1 to 3.5, starts with simplifying the problem and mapping the main structural components to the 2D plane. The results of the mapping process are shown in Figure 4.2. The process of mapping is not trivial and engineering choices are required. Firstly, only the longitudinal stiffeners are mapped to the XY-plane. The optimization of a support structure is done in a 2D design domain. If therefore there exist multiple structural components perpendicular to the mapping plane, a decision must be made which components need to be stabilized by the later optimization stage. In this case, as displayed in Figure 4.2a and 4.2b, the

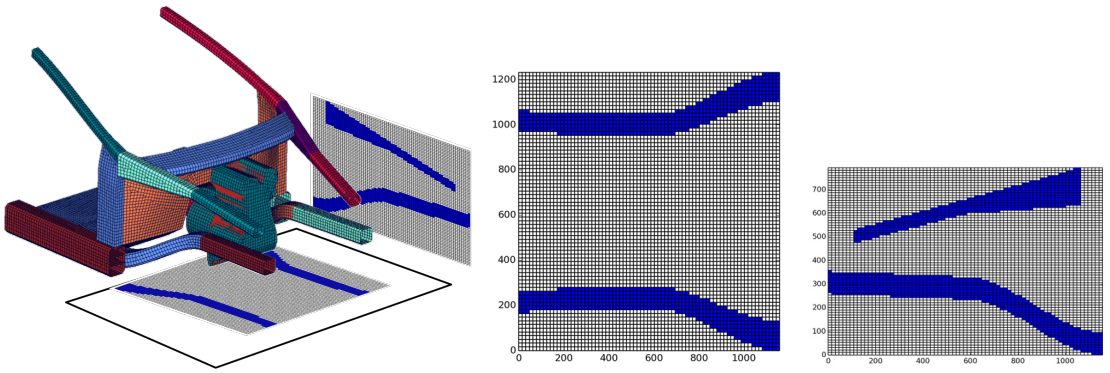

(a) Vehicle front with the two mapping planes, XY-plane and XZ-plane.

(b) Map of the longitudinal stiffeners on the XY-plane.

(c) Map of the longitudinal stiffener and upper load-path on the XZ-plane.

FIGURE 4.2. Mapping results on the composite vehicle front.

choice is made to focus on the longitudinal stiffener. This choice is supported by the fact that these stiffeners classically perform the bulk of the energy absorption in a crash and provide a large part of the structural rigidity in the vehicle front. The upper load paths, portrayed by the beams attached to the upper part of the A-pillar, can be part of a separate optimization stage and optimized in parallel to the other mapped components. For reasons of scope and simplicity this chapter focuses on the optimization of the longitudinal stiffeners. Figure 4.2c shows the upper load-path and longitudinal stiffener mapped on the XZ-plane.

4.1.2 Defining the Load Case

The next step is to define the load case for the shape optimization of the supporting structure. The method applies an adapted form of the ESL method, as explained in section 3.3. It is possible to define the load-lines directly on the entire structure as presented in Figure 4.1 and assess the transient dynamic response of the FMVSS208 load cases on it. However, this is relatively complex and not necessary to validate the methods. Therefore, the scenario is simplified and the longitudinal stiffeners are “flattened” as shown in Figure 4.3. This simplification has an influence on the structural behavior of the stiffeners, this influence is ignored for now.

The load lines are defined as seen in Figure 4.4. These load lines represent the location from which the displacements are assessed during the transient dynamic response

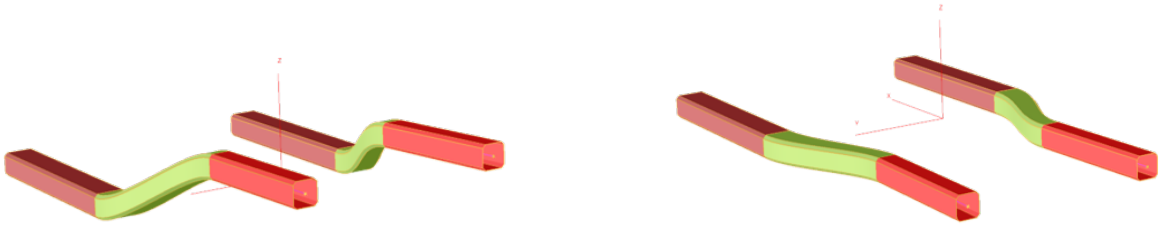

(a) Longitudinal Stiffeners in their original shape.

(b) Flattened Stiffeners to 2D XY-Plane.

FIGURE 4.3. Flattening of the Longitudinal Stiffeners to the 2D XY-Plane.

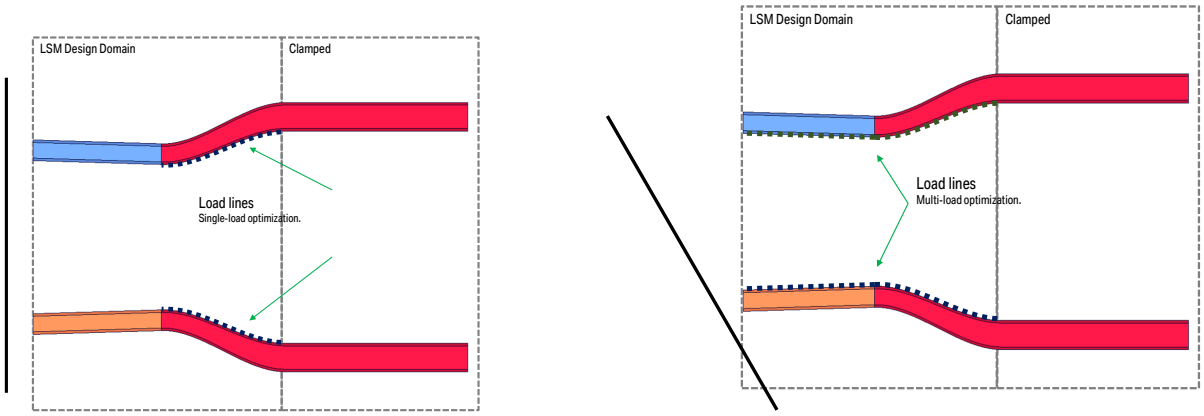

(a) Load lines for the 0° impact load case. This is a single load case.

(b) Load lines for the 30° impact load case. These are two separate load cases (multi-load).

FIGURE 4.4. Definition of the load lines for the two impact cases, resulting in three separate load cases.

simulation. Figure 4.5 shows the location of the load lines on the 3D representation of the longitudinal stiffeners. The load lines for the 0° impact case are placed on the curved section of the stiffeners and not over the entire length of the stiffener. The load lines should be placed on locations that will undergo the most deformation and therefore need to be supported in subsequent optimization steps. This assessment is done by engineering judgement. In the symmetrical 0° impact case the deformations obviously take place where the structure undergoes moment forces, i.e. in the curved section.

Now the stiffeners are assessed in an explicit crash simulation for both load cases. The 30° load case is symmetrical around the X-axis and therefore needs to be simulated once for one impact side. The other side is mirrored and handled as an extra load case.

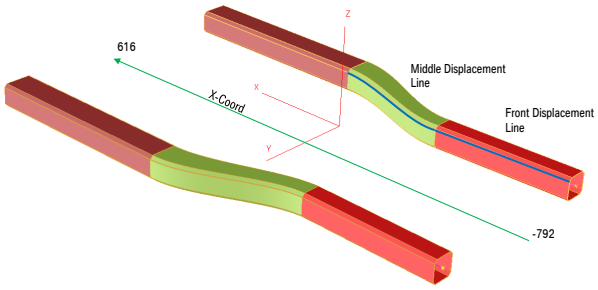

FIGURE 4.5. 3D location of the load lines on the longitudinal stiffeners.

The deformation results are shown in Figure 4.6.

In Section 3.3 it was explained that a snapshot of the dynamic structural behavior at a certain time should be chosen. In the case of the 30° impact, the deformation status at 3 ms shows significant deflection away from the rigid barrier, as seen in the deformation plot in Figure 4.18a. The preferable behavior would be that the beams remain stiff and absorb the impact energy through progressive crushing, hence the structural rigidity is compromised. Therefore the deformation at 3 ms is taken as initial snapshot. The deformation as a result from the 0° impact is not that clearly visible. However, from the plotted deformation of the load lines at 3 ms, seen in Figure 4.18b, it can be said that the deformation is still significant. The lateral displacement of the stiffener at $x = -200$ mm is comparable to the lateral deformation resulting from the 30° impact at $x = -200$ mm.

The snapshot of the dynamic structural behavior is translated into a load case for the two-dimensional representation of the structure, see Figure 4.2b. First, the displacements assessed on the loadlines are interpolated on the corresponding FE nodes of the 2D representation, see Figures 4.9a and 4.9b. Then, via the ESL method, the equivalent loads are derived, see Figures 4.9c and 4.9d. The ESL are calculated on a FE model with an initial material distribution, which was explained in Section 3.3. The initial FE model can be found in Figure 4.8.

4.1.3 Solving the shape optimization problem

With the load cases defined, the LSM based shape optimization, as explained in Section 3.4, is applied. However, the optimization of the support structure presents a challenge to the overall crash-worthiness problem. The forward portion of the longitudinal stiffeners is designed to absorb the impact energy of the crash. Section 1.2 explained that the amount of energy absorbed by the advanced composite material is proportional to the

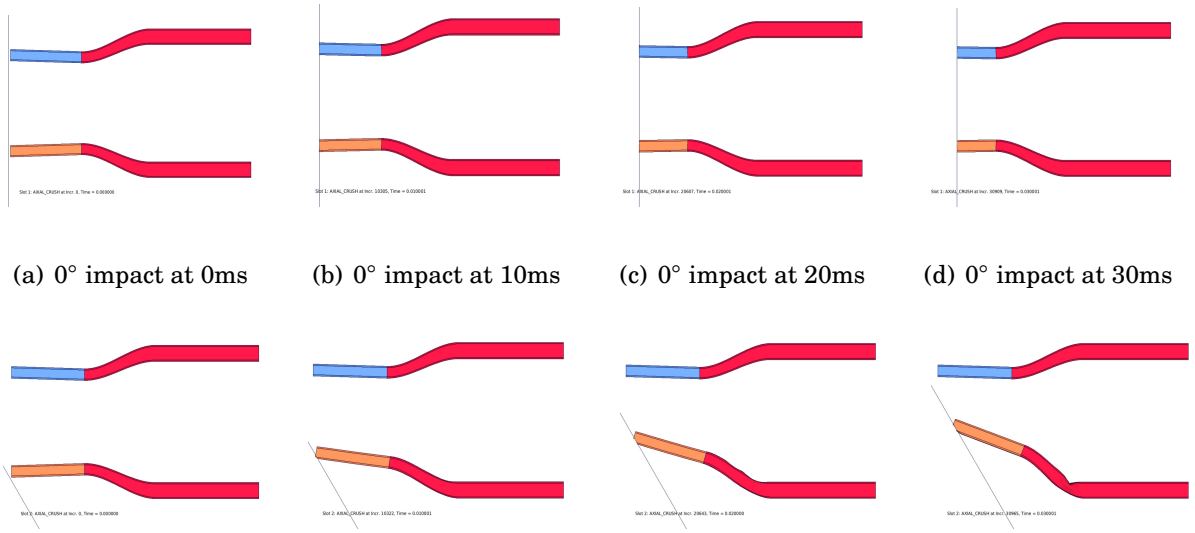

(a) 0° impact at 0ms (b) 0° impact at 10ms (c) 0° impact at 20ms (d) 0° impact at 30ms

(e) 30° impact at 0ms (f) 30° impact at 10ms (g) 30° impact at 20ms (h) 30° impact at 30ms

FIGURE 4.6. Deformation results after simulating both impact scenarios for 30ms.

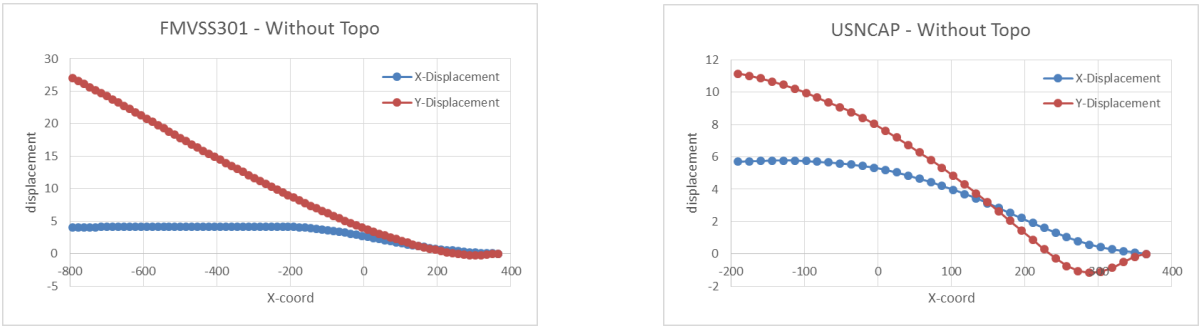

(a) Displacement [mm] of the loadline for the 30° load case.

(b) Displacement [mm] of the loadline for the 0° load case.

FIGURE 4.7. Displacement of the loadlines for both load cases at 3 ms without optimized structural support.

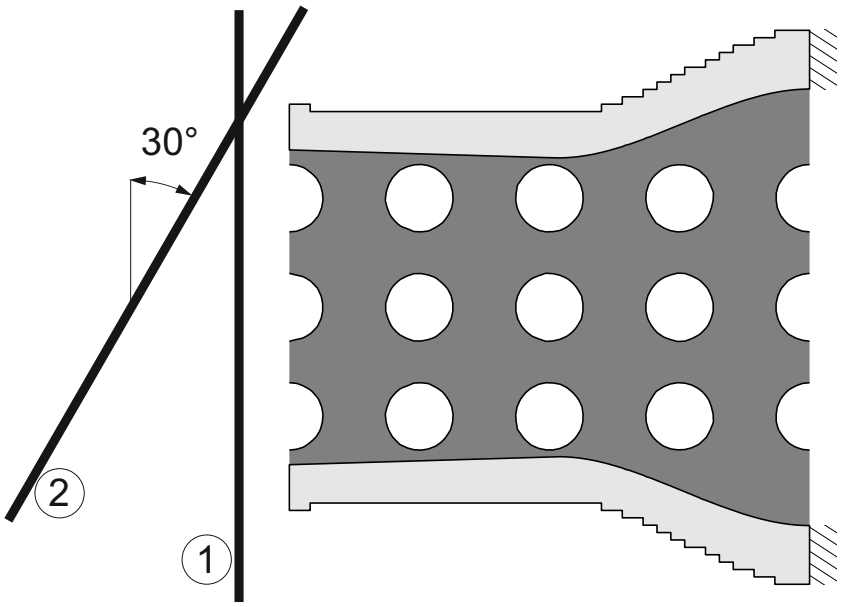

FIGURE 4.8. Load case definition and initial material distribution for the longitudinal stiffener structural optimization problem.

amount of material perpendicular to the crash front. Also, the ability of the composite to produce a stable progressive crush-front, and thus absorb energy, is dependent on the stability of the local composite material and structure near the crush-front. The reaction forces during the impact are therefore largely dependent on the crush force. By adding material in the impact or crush zone, the reaction force is potentially increased and thus the deceleration of the vehicle is increased as well. The level of deceleration largely determines the level of injury on the vehicle occupants. Another way to look at it is the minimum required overall vehicle deformation by applying the conservation of energy equation:

$$T^K = T^P \tag{4.1}$$

where T^K is the kinetic energy at the moment of impact and T^P is the potential energy of the vehicle structure. After substituting:

$$0.5mV^2 = m \cdot a \cdot L \tag{4.2}$$

with m the vehicle mass, V the initial velocity, L the overall deformation length and a the vehicle average deceleration. Now rewriting for deformation, results in:

$$L = \frac{V^2}{2a}. \tag{4.3}$$

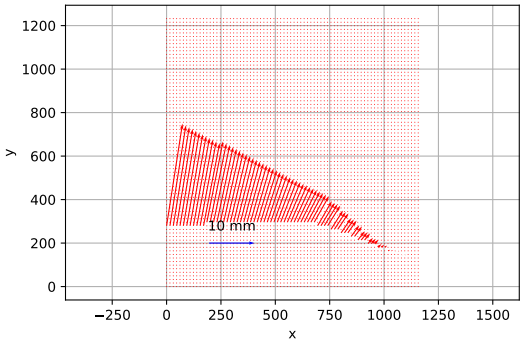

(a) Displacement distribution resulting from the 30° load case interpolated on the 2-D projection of the longitudinal stiffener.

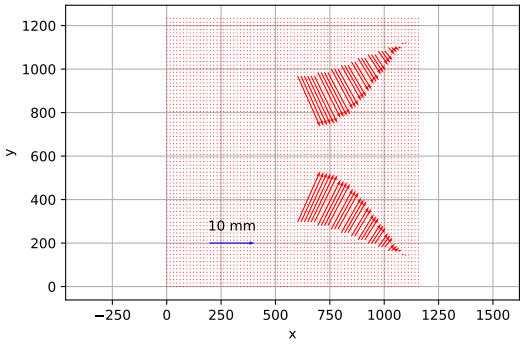

(b) Displacement distribution resulting from the 0° load case interpolated on the 2-D projection of the longitudinal stiffener.

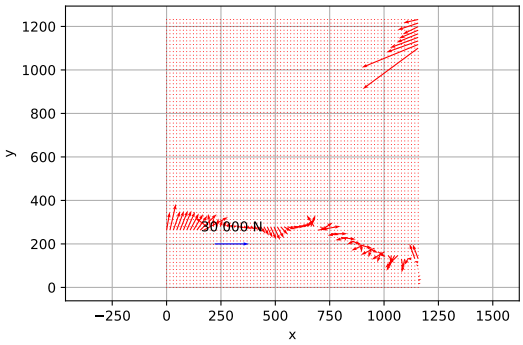

(c) The ESL distribution for the 30° load case.

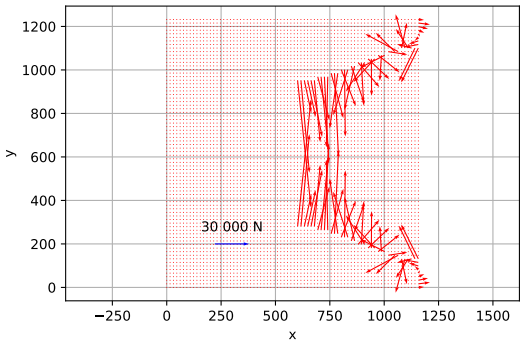

(d) The ESL distribution for the 0° load case.

FIGURE 4.9. Nodal displacement distributions of the 2-D FE model of the longitudinal stiffener and their ESL distributions resulting from the crash load cases.

The USNCAP load case (0° impact) requires a controlled deceleration, as in this case the impact is most severe and the requirements on the injury criteria are the hardest. As a rule of thumb, 30g is considered a good maximum for the deceleration. The impact speed for the USNCAP load case is equal to 56 km/h. Equation (4.3) can easily be solved if we assume a perfect, constant, deceleration:

$$L = \frac{V^2}{2a} = \frac{15.56^2}{2 \cdot g \cdot 30} = 411 \text{ mm} \tag{4.4}$$

The deformation of 411 mm is the minimum required deformation in order to achieve a vehicle deceleration that evolves around the maximum of 30g (the deceleration will never be constant in realistic crash scenarios). By adding a support structure for the stiffeners

in the presented optimization problem, the deformation length might be reduced. By providing partial control over the geometry during the shape optimization of the structure in the crush zone the deceleration, also known as vehicle crash pulse, can be reduced. In this research, this control is provided by the Local Volume method as presented in Section 3.4. This was partially published by the author of this thesis in [45].

The goal is to provide a constant cross-sectional area, perpendicular to the 0° impact barrier, and to create relatively thin structural members. The optimization problem set-up is shown in Figure 4.10. The local volume domain consists of 15 local volume columns, COL_l for $l = 1 \ldots 15$, in the area that contains the minimal deformation depth. By dividing the design domain in slender columns and setting subsequent constraints, the volume in perpendicular direction to these columns can be compelled to a predefined distribution. The mesh for the mechanical simulation consists of approximately 6,000 shell elements with eight degrees of freedom. The right edges of the beams are fully clamped. The initial level set boundaries are distributed as a pattern of circular holes, as shown in Figure 4.8.

The optimization problem, as described by Equations (3.4) and (3.20), is defined as follows. The global maximum volume constraint, $V_{\max} = 0.2$, the local maximum volume constraints, $V_l^{\text{loc, max}} = 0.2$ for $l = 1 \ldots 12$ and $V_l^{\text{loc, max}} = \{0.3, 0.4, 0.5\}$ for $l = \{13, 14, 15\}$. The increasing constraint value in the last three columns is to allow for a smooth geometry transition between the local and global volume domains. The parameters for the optimization algorithm are set as follows: $\beta = 0.$, which means the parameter regularization method is disabled. In addition, we choose for the Helmholtz-type regularization smoothing parameter, $R = 20$, and the Courant-Friedrichs-Lewy (CFL) time step multiplication factor, $t_{\text{fac}} = 0.9$. For the Lagrange multiplier update method, the parameters are as follows: $\tau_0 = 100$ and $\lambda_0 = 7$. The bandwidth parameter h is set to 0.8 times the critical element side length. The critical element side length is here: $l_{\text{crit}} \approx 15,4\text{mm}$. The parameters for the optimization algorithm are summarized in Table 4.1.

The optimization result is shown in Figure 4.11a and the iteration histories of the objective and global volume constraint are given in Figure 4.12. The iteration history of the local volume constraints is shown in Figure 4.13. The local volume history shows that all constraints are met. The local volumes can be lower as their set maximum, because inequality constraints are used. This effect is seen in the first three columns. However, the compliance minimization drives most local volumes towards their maximum. Therefore, columns 4 to 12 show a convergence to 0.2. This result gives the required constant volume distribution in x-direction.

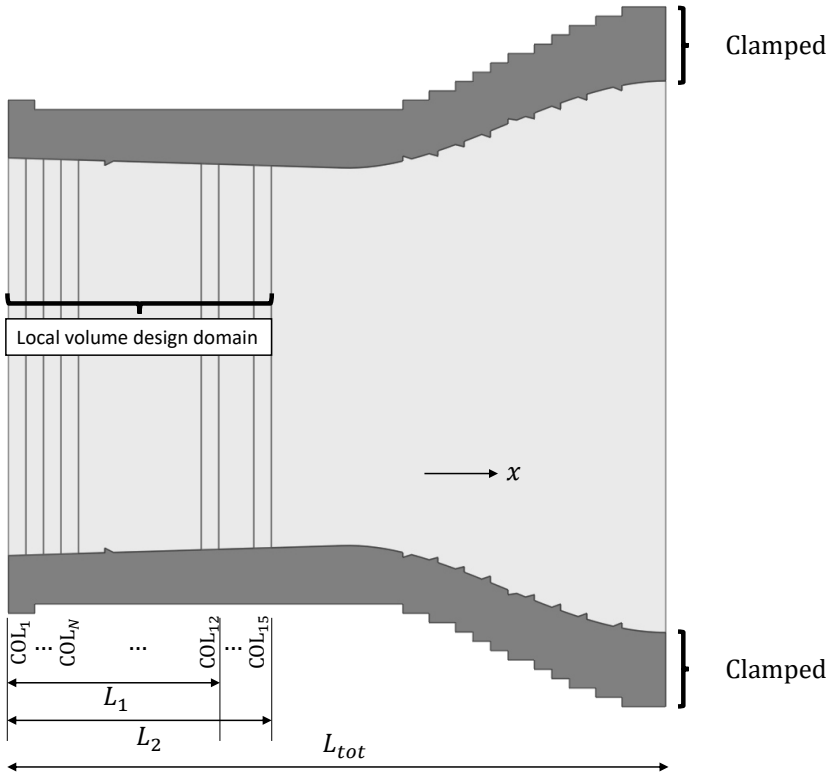

FIGURE 4.10. Problem set up and definition of the design domains. Each local volume column, COL_N, has a width of ≈ 31mm, $L_1 \approx 370$mm, $L_2 \approx 463$mm and $L_{tot} = 1157$mm. A total of $N = 15$ local volume domains is used.

TABLE 4.1. Parameter set-up for the optimization algorithm.

Parameter	**Symbol**	**Value**	**Unit**
Bandwidth	h	0.8	[-]
Maximum Iteration	–	600	[-]
Lagrangian Method	–	Augmented	[-]
Minimum Element Density	ϵ	1.e-4	[-]
Parameter Regularization Penalty	β	0.	[-]
Initial Penalty Factor	τ_0	100.0	[-]
Penalty Multiplier	α	0.9	[-]
Initial Lagrangian Multiplier	λ_0	7.0	[-]
Helmholtz-type Regularization	R	20.0	[-]
CFL Time Step Factor	t_{fac}	0.9	[s]

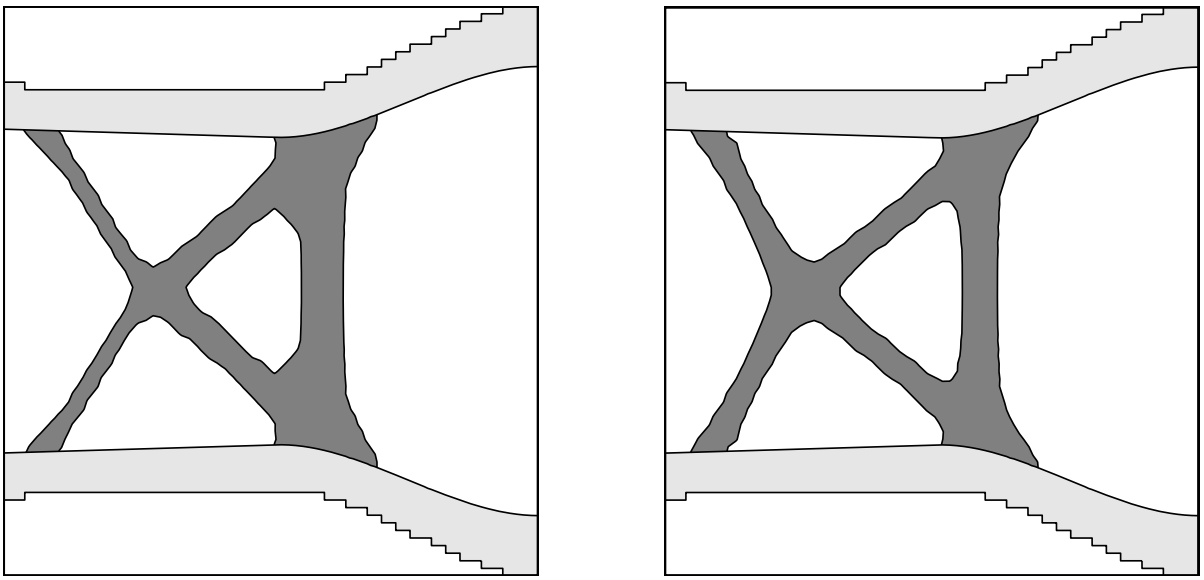

(a) Optimal shape with local volume constraints active.

(b) Optimal shape with only the global volume constraint active.

FIGURE 4.11. Shape optimization results for longitudinal stiffener structural optimization problem.

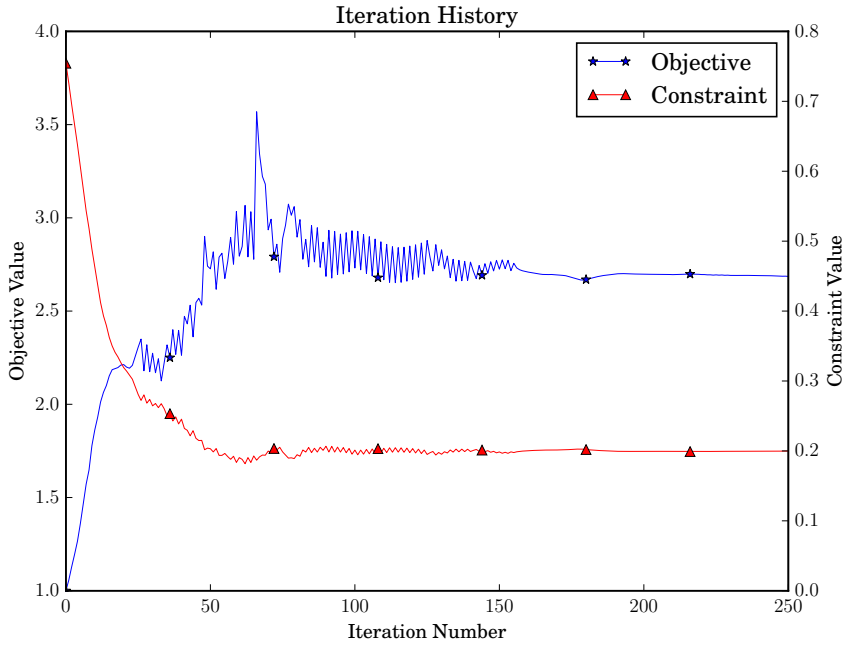

FIGURE 4.12. Optimization history for the objective and global volume values.

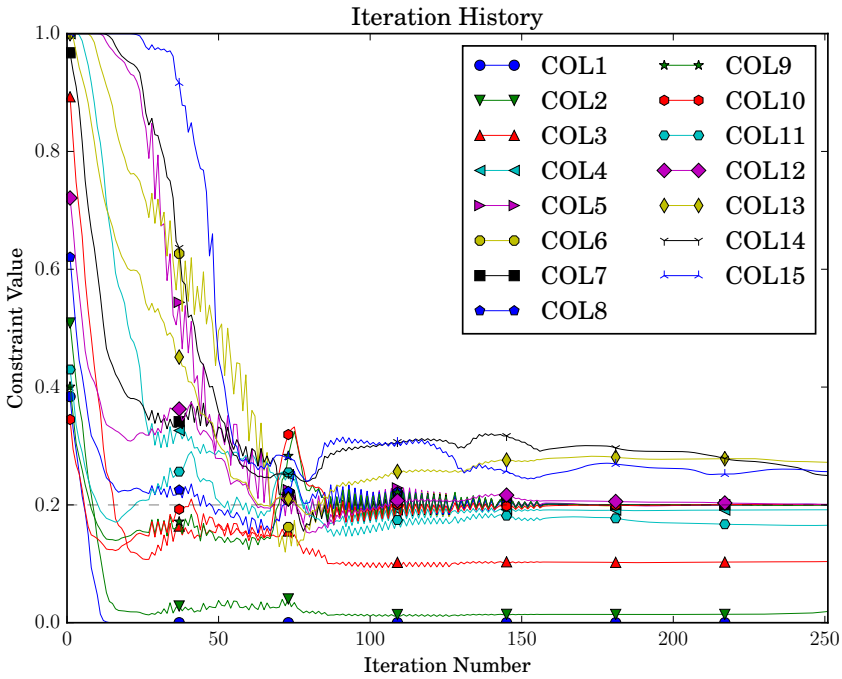

FIGURE 4.13. Optimization history for the local volume values.

To exemplify the effect of the local constraints, the optimization is rerun with only the global volume constraint active, $V_{glob}^{\max} = 0.2$. The result is shown in Figure 4.11b. The resulting optimal shape looks similar to the optimum with local constraints active. However, looking at the volume ratios in the local domains in Figure 4.14, the differences become clear. With only the global constraint active, the volumes in most domains are significantly higher than 0.2. More importantly, the local volume ratios change notably over the domains, resulting in a discontinuous cross-sectional impact area. The volume ratios with local constraints active show a largely constant value of 0.2, going upwards in domains 13, 14 and 15. This is a result of the higher constraint value in those domains, as described earlier.

4.1.4 Mapping to the 3D Design Domain

In this stage of the optimization work-flow the optimized composite support structure from the previous section is mapped back to the 3D design domain. In Section 3.5 the assumptions and sequence of methods necessary are explained. First the raw shape optimized result is smoothed. The result in Figure 4.11a shows some rough edges and minor shape artifacts that are undesired and difficult to translate into a 3D FE-model.

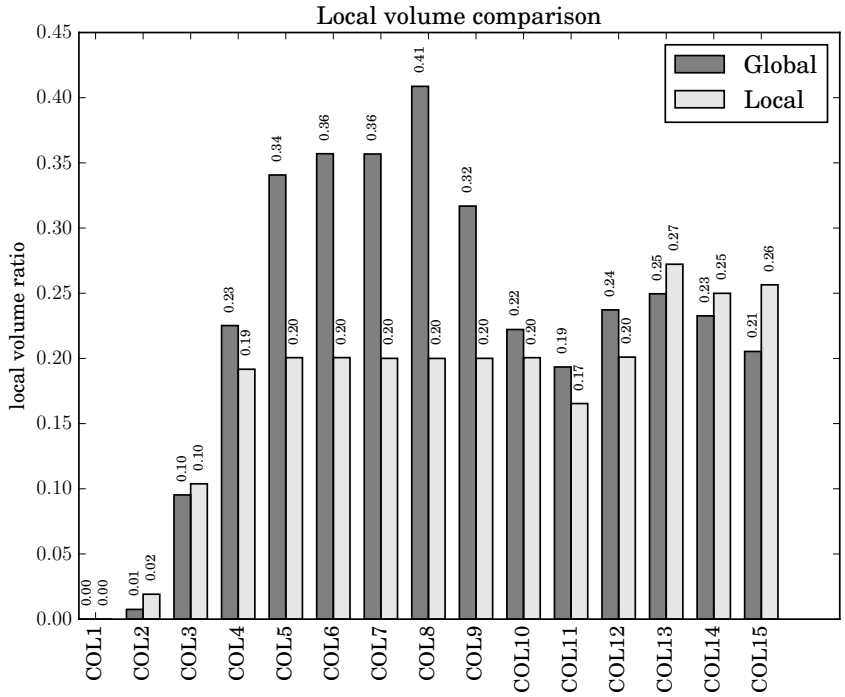

FIGURE 4.14. Comparison of the local normalized volume values. Light gray: only global constraint active. Dark gray: Global and local constraints active.

The smoothing is done by transforming the iso-contour to a bi-linear spline description. In this step, the smoothness of the splines are controlled by a smoothing parameter. The bi-linear splines are exported to a DXF format, which is a familiar CAD geometry description. The geometry is imported by a pre-processor for developing the 3D FEM mesh, in this case HYPERMESH from Altair is used. The bi-linear spline description of the optimized structure and the subsequent transformation to a 3D shell structure is shown in Figure 4.15.

The result from Figure 4.15f is then integrated in the initial crash problem (see Figure 4.4), the final structure is shown in Figure 4.16. Both load-cases are simulated with the optimized support structure. The results are shown in Figure 4.17. When compared to the deformations shown without structural support in Figure 4.6, the results are significantly better. In Figure 4.18, the displacements at 3ms of the nodes at the loadlines for both load cases are plotted. Progressing further in the 30° crash case, the longitudinal stiffener becomes unstable again. The lateral support is crushed and the stiffener is allowed to deform unhindered. Therefore, no progressive crushing takes place and only little energy is taken out of the impact. This result could be expected, as the static linear optimization

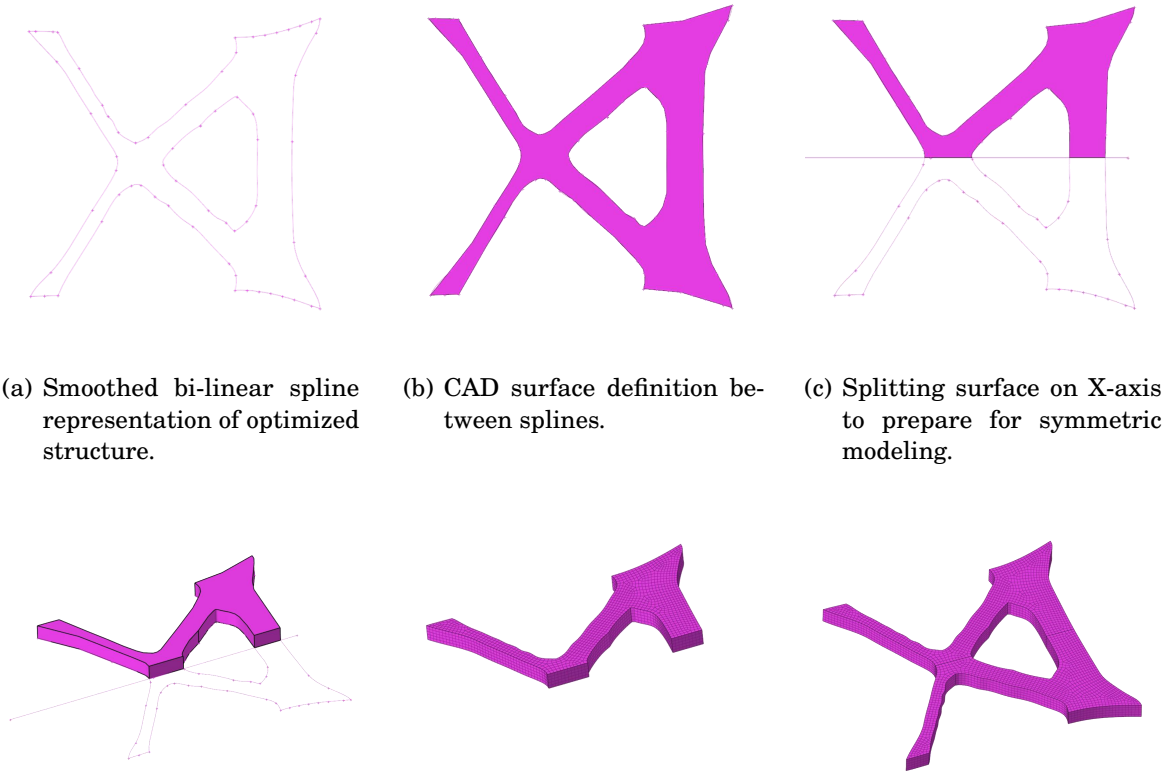

(a) Smoothed bi-linear spline representation of optimized structure.

(b) CAD surface definition between splines.

(c) Splitting surface on X-axis to prepare for symmetric modeling.

(d) Offsetting the surface to create a 3D box.

(e) Automatic meshing on the surface of the box.

(f) Duplicating on symmetry axis.

FIGURE 4.15. Process of creating the 3D representation on the basis of the 2D optimized results.

of the support structure is based on the ESL of the deformations at 3ms into the impact.

The proposed optimization work-flow solves this problem by introducing an outer loop of the optimization. The results are assessed and a new time point is defined where the structure becomes unstable. The 0° load case is stable and needs no further optimization. Upon further investigation of the deformation behavior, the 30° load case now shows significant structural instability starting at 16ms. At this time the left longitudinal stiffener starts to move inward. The second iteration of the optimization process starts at the ESL load case definition. This creates two new load cases: the symmetric 30° impact. It is important to notice that at 16ms, a portion of the longitudinal stiffeners is crushed. This phenomenon is incorporated by leaving this part of the stiffener out in the calculation of the new ESL. The two new load cases are added to the current three, leading to five loadcases to consider in the multi-objective shape optimization stage. The

process and settings are the same as in the first iteration of the outer loop. The resulting optimized structure and its comparison to the first iteration result is shown in Figure 4.19.

An interesting result is the rearward shift of the forward “legs” of the supporting structure. Also, the attachment to the stiffeners is broader. The angle of the legs are a bit steeper. This second iteration result is again subjected to both crash load cases, the results are presented in Figure 4.20. These results clearly show a better performing structure in case of the 30° impact. The left longitudinal stiffener stays stable throughout the impact. Also, more energy is absorbed by the stable progressive crush of the CFRP composite material. This is visible by the progress of the impact barrier at 50ms, which is significantly less compared to the previous iteration. However, the stability after 30ms might also be a result of the left leg of the support structure that, after it lost its attachment to the stiffener, still provides support. This is of-course not a result incorporated within the optimization work-flow.

The 0° impact load case does not show the ideal behavior. Part of the longitudinal stiffeners break away due to crush forces. This is likely a result of local failure caused by stress concentrations at the base of the attachment between the forward legs of the support structure and the longitudinal stiffeners. These stresses are induced by the relatively large connecting area and the way the joint is modeled. Further local optimization of the joint is necessary.

The local volume constraints in both outer loop iterations influenced mainly the shape of the forward legs. I both cases, the direct influence on the crush force by having a constant cross-sectional area in X-direction is minimal, as the legs buckle and move away without significant crushing. However, the local volume constraints do influence the slenderness of the forward legs, without compromising on the global volume constraint. This result was already seen in Figure 4.11. This in turn does influence the overall crash response of the structure. The slender members break or buckle away from the crush-front easier as soon as the crush-front passes the joint area on the stiffeners. And consequently, this reduces the overall impact on the deceleration pulse of the vehicle. In Chapter 5 we further discuss the results of the local volume constraint method.

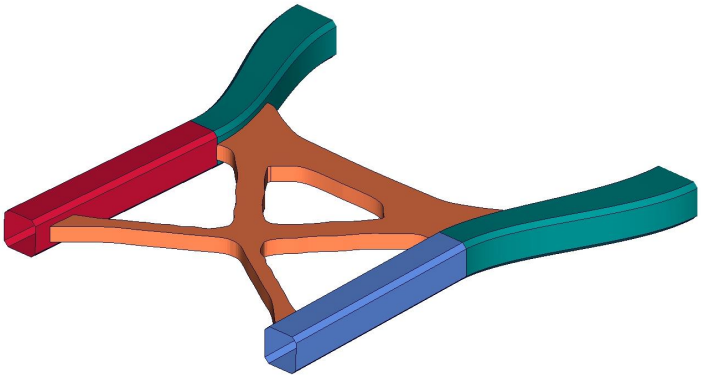

FIGURE 4.16. Longitudinal stiffeners with the optimized support structure.

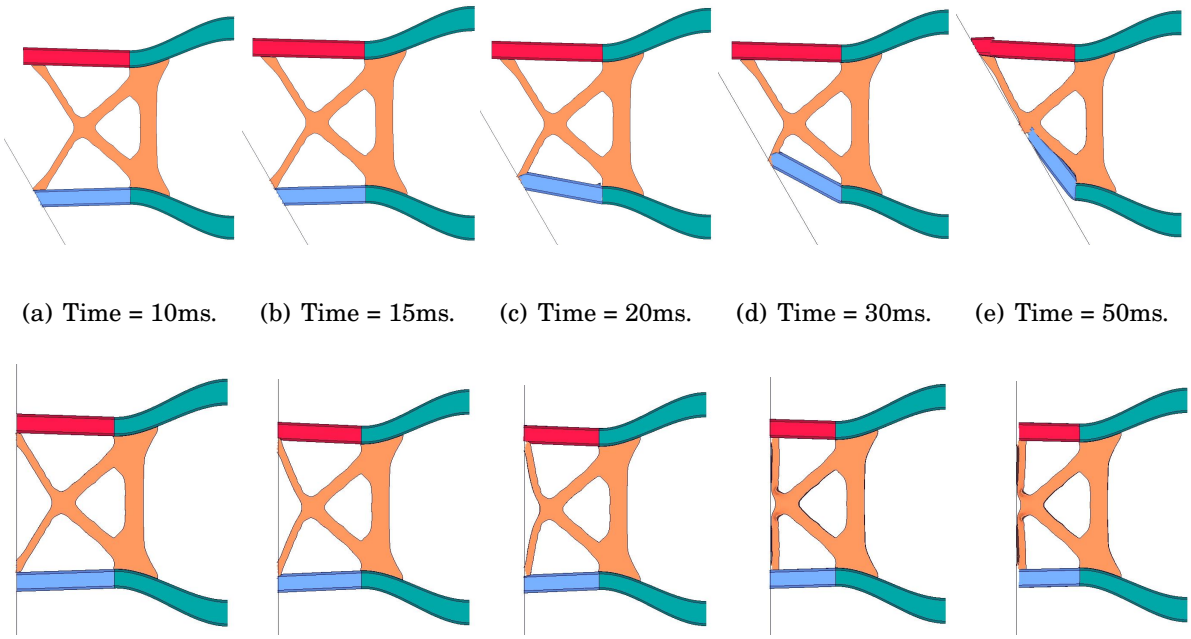

(a) Time = 10ms. (b) Time = 15ms. (c) Time = 20ms. (d) Time = 30ms. (e) Time = 50ms.

(f) Time = 10ms. (g) Time = 15ms. (h) Time = 20ms. (i) Time = 30ms. (j) Time = 50ms.

FIGURE 4.17. Crash results of the 30° (top row) and 0° (bottom row) load-cases on the optimized longitudinal stiffeners.

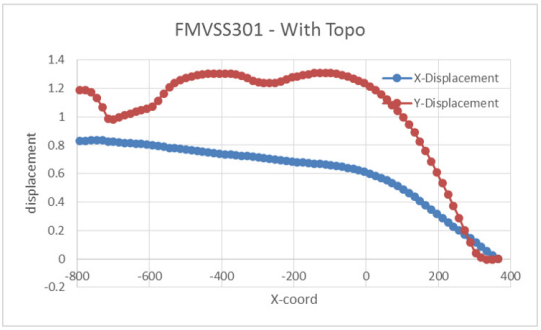

(a) Displacement [mm] of the loadline at 3ms for the 30° load case.

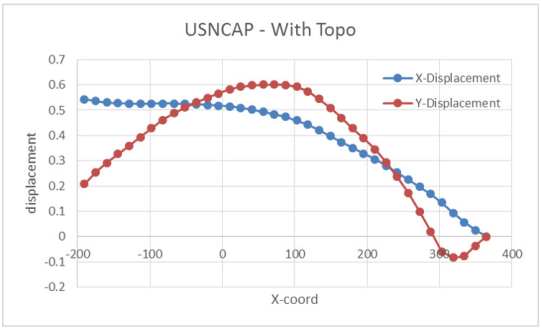

(b) Displacement [mm] of the loadline at 3ms for the 0° load case.

FIGURE 4.18. Displacement [mm] of the loadlines for both load cases at 3 ms with the optimized structural support.

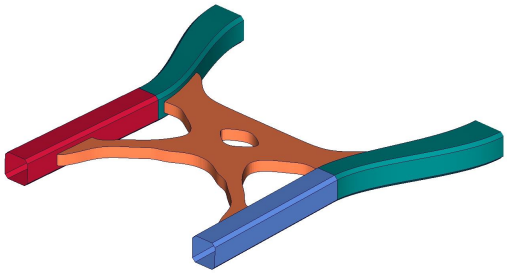

(a) Longitudinal stiffeners with the optimized support structure after a second optimization iteration.

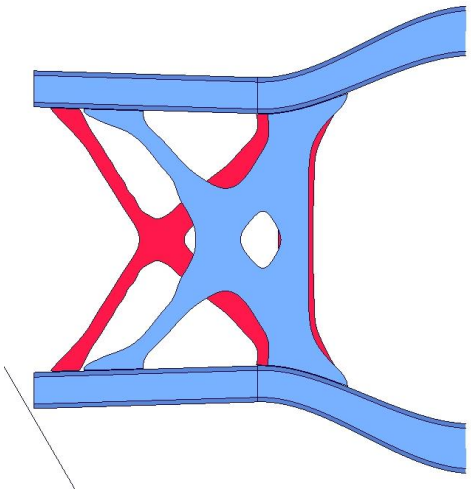

(b) Comparison of the results from the first (in the back) and second (in front) loop iteration: first loop at 3ms, second loop at 16ms.

FIGURE 4.19. Longitudinal stiffeners with the optimized support structure.

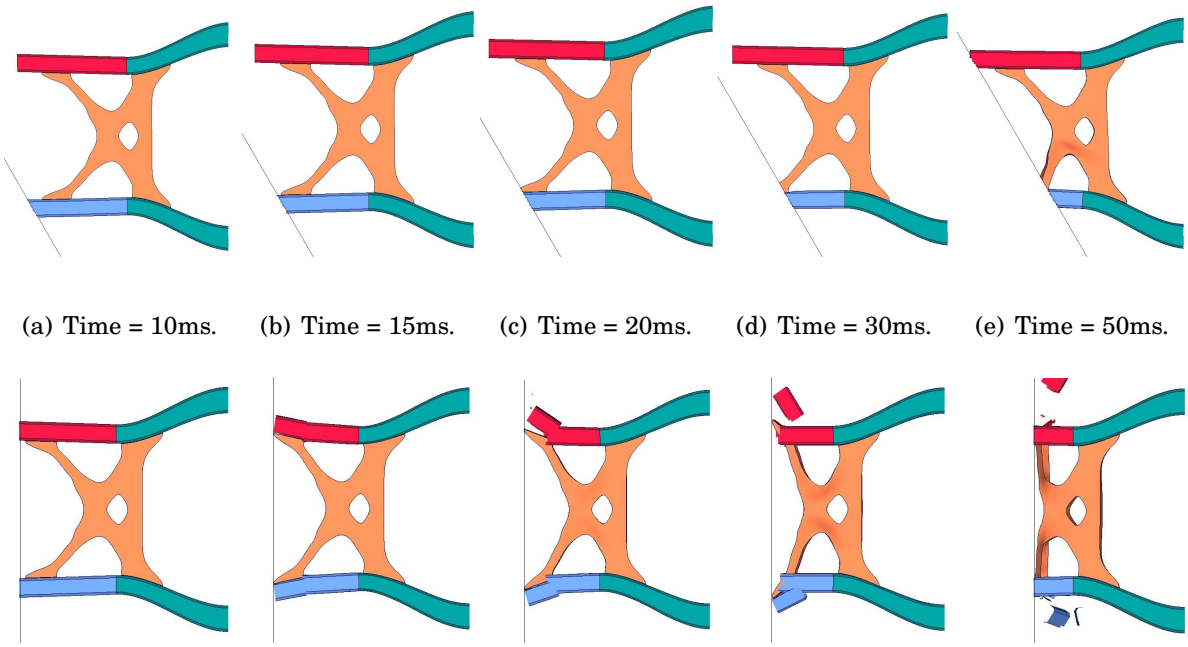

(a) Time = 10ms. (b) Time = 15ms. (c) Time = 20ms. (d) Time = 30ms. (e) Time = 50ms.

(f) Time = 10ms. (g) Time = 15ms. (h) Time = 20ms. (i) Time = 30ms. (j) Time = 50ms.

FIGURE 4.20. Crash results of the 30° (top row) and 0° (bottom row) load-cases on the optimized longitudinal stiffeners from the second outer loop iteration.

4.2 Optimization of an S-Rail

4.2.1 Complexity Reduction on an S-rail problem

The content of this section was partially published by the author in the journal of Composite Structures. [46]

In this section, a vehicle typical crash-worthiness problem is solved to validate the presented methods. The example is relatively simple for a design problem, but shows enough complexity, including combinations of bending, local and global buckling, and axial crush of the composite material. The complexity of the problem is deemed sufficient to validate the presented methods.

Problem Description: S-Rail The design problem, which can be considered a benchmark for this field, is a parametric tubular structure with a single S-shaped bend, representing a simplified vehicle S-rail. The S-rail is a typical and important sub-structure of every modern automotive vehicle. It is located in the front of the car and has generally the following three main purposes:

- Energy absorption: It is the major component in the vehicle front, carrying most of the drive-train and reaching almost to the front of the vehicle. It should therefore absorb a significant part of the energy resulting after impact.
- Passenger protection: it should increase the overall stability and deformation resistance of the safety cell.
- Functionality: it should provide sufficient stiffness and strength to carry the motor and other core vehicle components.

The S-rail is shaped as an 'S' to bridge the bumper height (partly determined by law) and the vehicle undercarriage, thus guiding the impact forces to the stiffest parts of the vehicle main body. The 'S' shape is also a result of the vehicle front package, such as spring-damper systems. A typical example of the S-rail is given in Figure 4.21. The simplified S-rail is shown in Figure 4.22 and Figure 4.23.

The simplified S-rail is fully clamped at its roots (cross-section CS_1, see Figure 4.23a). An rigid 400 kg impactor impacts the S-rail with 8.2 m/s. This simulation represents a full frontal impact scenario, with the impact energy scaled down for the solitary S-rail with respect to a full vehicle. The impact energy should be absorbed fully within a certain

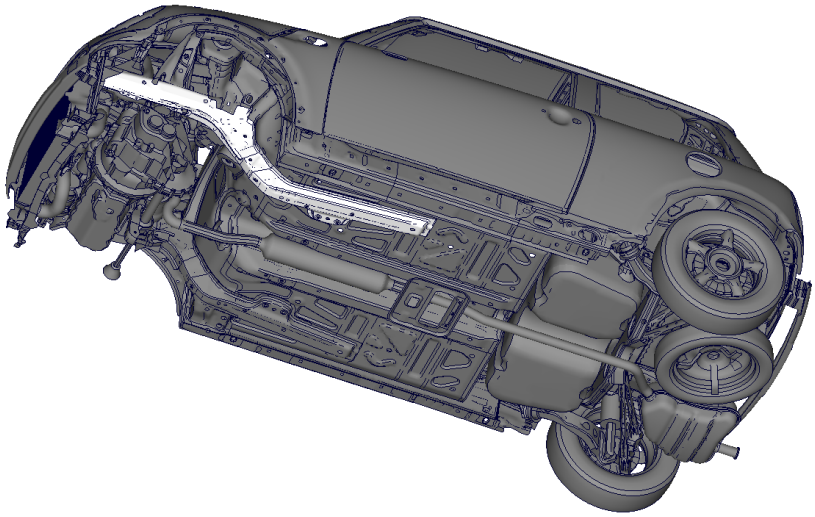

FIGURE 4.21. Example of an S-rail structure in a current vehicle (marked in white).

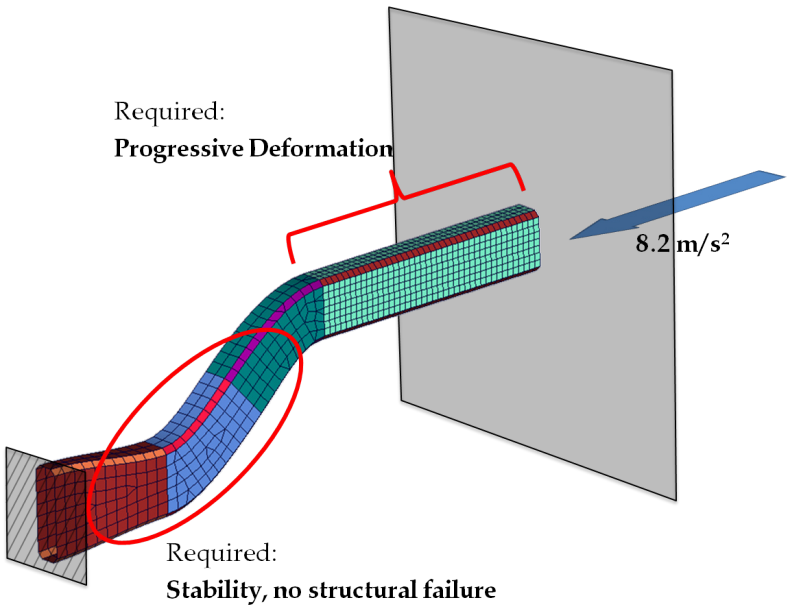

FIGURE 4.22. Setup of the design problem, showing the two important design requirements.

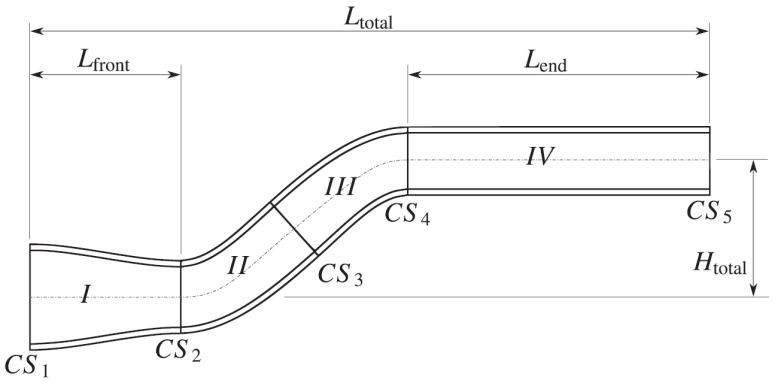

(a) side view of the S-rail.

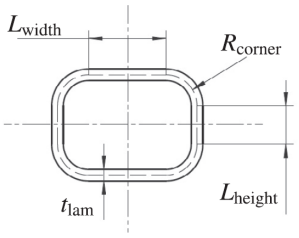

(b) cross-section view of the S-rail.

FIGURE 4.23. Problem description; parameterized tubular structure with single S-shaped bend.

maximum available deformation length. This is a common requirement in automotive crash-worthiness design. The shape of the S-rail causes large bending moments at its root, increasing the problem of structural stability.

The S-rail has two main design requirements: (1) Stable progressive crushing over a certain maximum deformation length. (2) Structural stability to support this behavior without collapse. Figure 4.22 summarizes the problem set-up. The S-rail is considered structurally stable when stable progressive crush is possible until all impact energy is absorbed. Structural instability is defined as the collapse or global buckling of the S-rail during impact. The limit state is now defined as the point in between these two stability criteria.

The S-rail geometry and composite material properties are parameterized. The structure is divided into four sections and five cross-sections. The geometry parameters are shown in Figure 4.23 and SFE CONCEPT is used to parameterize the design. Here, L_{front}, L_{end}, H_{total} and W_{total} are initial parameters and are not varied. Cross-sections CS_i are parameterized such that the dimensions L_{width} and L_{height} can be changed symmetrically about their respective symmetry axis. The corner radius R_{corner} remains unchanged at 8 mm. The total height and width of the cross-sections CS_i are calculated by: $2R + L$. A 3^{rd} order Bézier curve is used to shape the curved sections, making sure that the structure will stay smooth with the correct tangents at all cross-sections. A summary of the initial set-up parameters and their respective values can be found in Table 4.2 and a summary of the design variable parameters with their bounds can be

TABLE 4.2. Summary of the initial set-up of the S-rail, determined by the initial set-up parameters.

nr.	Name	Value [mm]
1	L_{total}	900
2	W_{total}	0
3	H_{total}	180
4	L_{end}	400
5	L_{front}	200

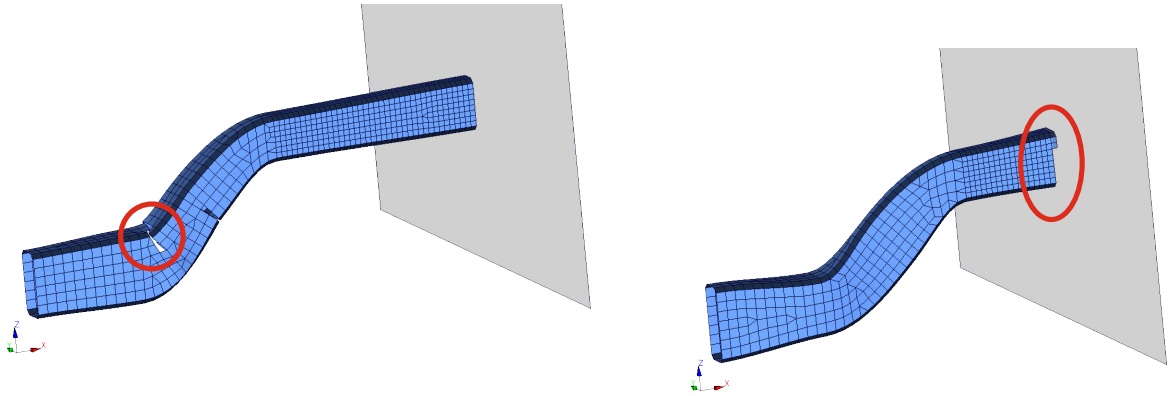

(a) S-rail showing structural instability by collapse.

(b) S-rail showing stable progressive crush.

FIGURE 4.24. Two typical simulation results, showing structurally stable (right) and unstable (left) behavior.

found in Table 4.3.

Implementation of FEA for impact simulation The crush behavior of the composite S-rail is simulated with ABAQUS/EXPLICIT and CZONE. The simulation is run until all energy is absorbed or the impactor has moved through the S-rail in its entirety. A simulation takes on average 15 minutes to run using one Intel Xeon CPU E5-2640 core at 2.5GHz on a 12 core workstation. Two examples of the simulated structural behavior are shown in Figure 4.24. An example of a structural instability is shown in Figure 4.24a and an example of stable progressive crushing in Figure 4.24b.

PSM for the S-rail The PSM approximates the LiSF from Equation (3.42) by predicting the onset of structural instability using global buckling.

TABLE 4.3. Summary of the design variable parameters used in the S-rail composite crash simulation.

nr.	Name	Bounds [mm] $\check{x}$	Bounds [mm] $\hat{x}$	Description
1	CS_{1_Y}	10	44	symm. increase of CS on y-axis or z-axis. Controls dimensions L_{height} (Y) and L_{width} (Z). Values in mm.
2	CS_{1_Z}	94	134	
3	CS_{2_Y}	10	70	
4	CS_{2_Z}	50	110	
5	CS_{3_Y}	10	70	
6	CS_{3_Z}	50	110	
7	CS_{4_Y}	10	64	
8	CS_{4_Z}	44	104	
9	CS_{5_Y}	10	64	
10	CS_{5_Z}	44	104	
15	V_{1_I}	–	–	Lamination Parameters per material section. Feasible domain is described in section 2.2.
16	V_{3_I}	–	–	
17	V_{1_II}	–	–	
18	V_{3_II}	–	–	
19	V_{1_III}	–	–	
20	V_{3_III}	–	–	
21	V_{1_IV}	–	–	
22	V_{3_IV}	–	–	
23	t_{I}	2	15	Thickness of the laminate per material section in mm.
24	t_{II}	2	15	
25	t_{III}	2	15	
26	t_{IV}	2	15	

Numerical buckling analysis is used to calculate P_{crit} in Equation (3.42). The mesh generated by the parameterized model in SFE-CONCEPT is parsed to an ABAQUS template where a linear static buckling analysis is performed on the model. The mesh is the same one used for the transient dynamic analysis from the previous step. It is important to note that the type of mesh and element size influence the buckling analysis significantly. To assess this influence, a simple mesh convergence study was performed. The results from this analysis are shown in Figure 4.25. The convergence study shows that there is some convergence. However, the critical buckling load will always decrease with smaller mesh sizes. A trade-off was made between computational efficiency and accuracy, resulting in the choice of an average mesh size of 18 mm. For the section of the S-rail where the impact occurs (material section IV) an average element size of 10

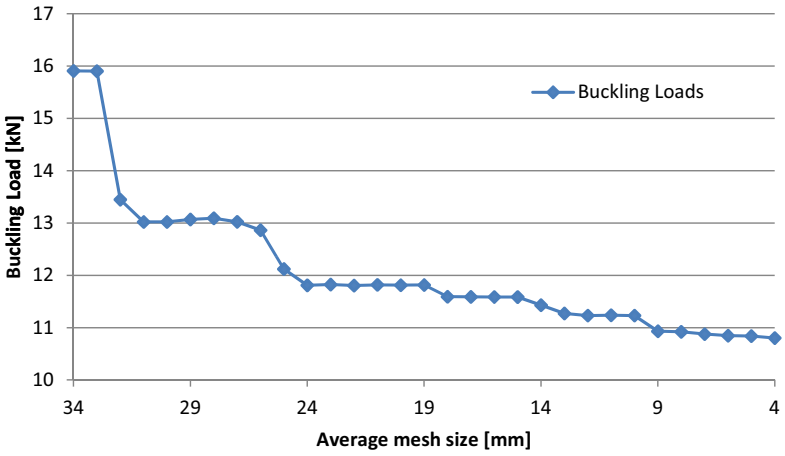

FIGURE 4.25. Mesh Convergence Study.

TABLE 4.4. Validation results of the PSM method.

Total DoE	599
Validated stable designs	173 (28.88 %)
Predicted stable designs	123
correctly predicted	103 (83.74 %)
Valid stable designs neglected	70 (40.46 %)

mm was chosen. This should facilitate accurate simulation results when cone forming occurs in this section. This happens when for instance cross-section CS_5 is significantly decreased with respect to CS_4.

The PSM is set-up as follows: a static perturbation force of $P = 1$ is placed at the center of cross-section CS_5 and is parameterized with the model. This perturbation force reflects the force into the structure caused by the barrier impact.

To validate that the PSM model reflects the structural stability of the S-rail accurately enough, the following experiment was performed. Both the transient dynamic and PSM simulation were run in parallel, each time using the same design instance of the S-rail model. To create a sufficiently large and diverse data set, a DoE was set up to collect 600 samples. The DoE used the MCS method and was constrained by the bounds as described in Table 4.3. The results of the PSM validation experiment are shown in Table 4.4. The results in Table 4.4 show that initially 173 designs (28.88 %) of the 599 experiments showed stable progressive crushing. One experiment failed to simulate

completely. After the assessment of the LiSF, 123 designs are deemed structurally stable, which is a reduction in the number of samples in the DoE of 71.12 %. Of comparing with the data from the transient dynamic simulations, 103 designs are correctly predicted structurally stable. In essence, a filtered design space is created out of the original DoE using the PSM as the filter. The filtered set of 123 designs has 83.74 % stable designs, showing improvement over the 28.88 % stable designs in the original 599 sample DoE set. The results show that the PSM method works as intended. It can be concluded that in this case the LiSF approximated by the PSM is correct up to 83.7%. It should be noted however, that after filtering, 70 stable designs are neglected, this is equal to 40.46 % of all stable designs. As a consequence the engineer should make a trade-off between the loss of valid designs over increased computational efficiency using the PSM. It is noted here, that this loss of valid designs is not a problem for most industrial design problems. That level of accuracy is not required here.

Creating the parameter importance hierarchy The goal is to find the parameter influence on the two major responses of the S-rail; the maximum deformation $\delta_{\max}$ and the S-rail mass M_{rail}. The S-rail design space is filtered for structurally stable designs with the PSM. This results in a significantly different response surface compared to the unfiltered design space. To reflect the difference, it is important to derive the parameter importance for both the complete design space and the filtered one. Sobol decomposition is used to derive the design parameter importance hierarchy. The derivation of the Sobol indices is a form of variation analysis. To remain computationally efficient, this decomposition requires some form of RSM to derive integrals necessary for this variational analysis. The SVM method is used to derive the RSM. A DoE is performed to generate the input for the SVM method. For convenience the same 600 sample DoE for validating the PSM and its results is used as input for the SVM.

The quality of the model is verified by deriving the Pearson correlation values:

$$r(X,Y) = \frac{\sum_{i=1}^{n}(X_i-\overline{x})(Y_i-\overline{y})}{\sqrt{\sum_{i=1}^{n}(X_i-\overline{x})^2\sum_{i=1}^{n}(Y_i-\overline{y})^2}} \tag{4.5}$$

where X and Y form two data sets, observed output and fitted model respectively, with individual values X_i and Y_i for $i = 1 \ldots N$ (Data set size). $\overline{x}$ and $\overline{y}$ are the mean values of both data sets. Table 4.5 presents the correlation values belonging to both the SVM models with and without Cross Validation (CV). The Pearson correlation values without cross validation show the quality of the SVM model with respect to the actual transient

TABLE 4.5. Correlation coefficients for validation of the SVM, with and without CV. For both the complete and filtered data set.

Data set	**Response**	**Correlation**	
		w/o CV	**with CV**
All	Intrusion, $\delta_{\max}$	0.8956	0.7487
	S-rail mass, M_{rail}	0.9541	0.9355
Filtered	Intrusion, $\delta_{\max}$	0.9591	0.7274
	S-rail mass, M_{rail}	0.968	0.9112

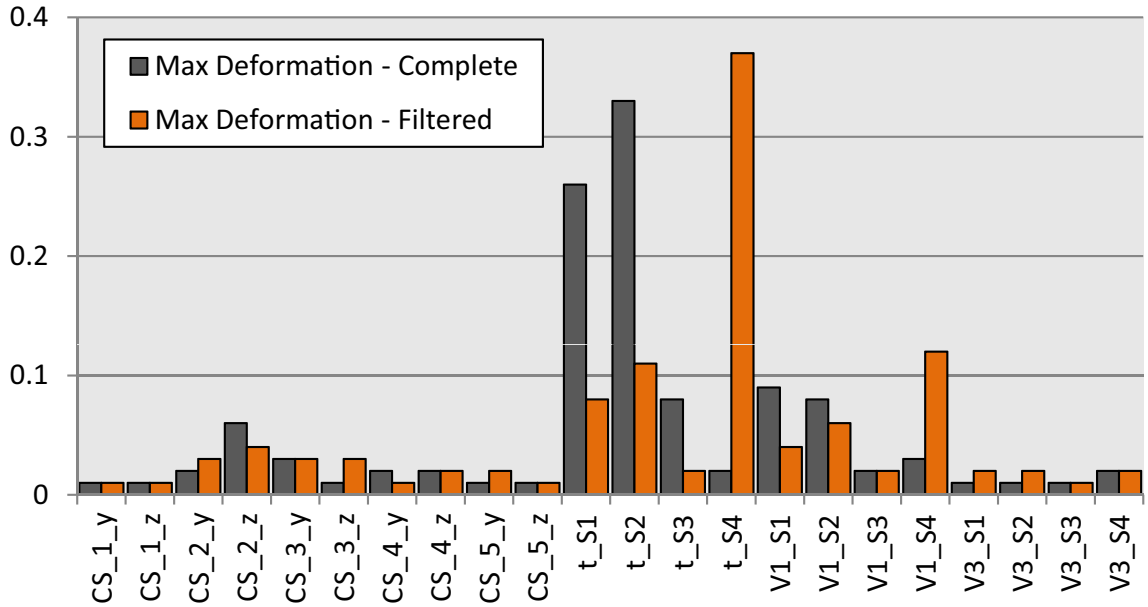

FIGURE 4.26. Total Sobol indices with respect to the maximum deformation response, $\delta_{\max}$.

dynamic simulation and the values with CV (leave-one-out method) show the predictive quality of the SVM model [62]. The SVM model shows satisfying results with and without CV. CLEARVU ANALYTICS [3] is used to generate the SVM response surface approximation and derive the Sobol indices. The results of the Sobol decomposition on the SVM based RSM model are shown in Figures 4.26 and 4.27. On comparing the results between the two responses, it becomes clear that the indices for the mass response are very similar for both PSM filtered and unfiltered response surfaces. For the maximum deformation response however, the results differ significantly. This is explained by that

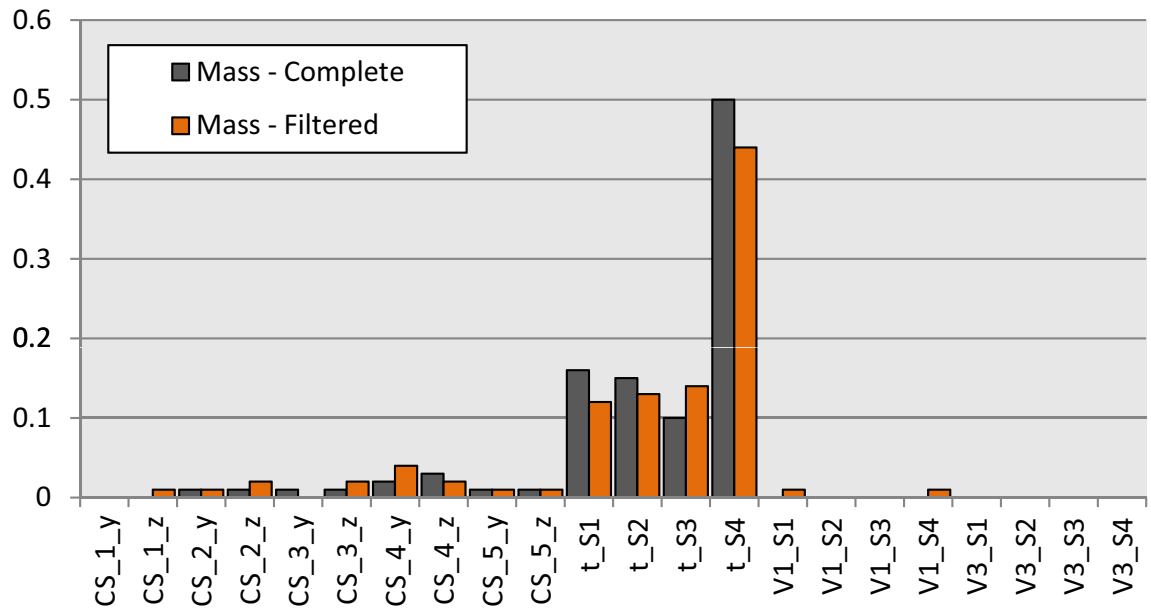

FIGURE 4.27. Total Sobol indices with respect to the S-rail mass response, M_{rail}.

the mass of the S-rail structure is a direct function of the design parameters, therefore the influence of a parameter stays the same. It is also noticeable that for the laminate thicknesses $t_{1,2,3}$ the sequence in hierarchy changes between the filtered and unfiltered design space. However, the changes are small and can be attributed to the quality of the RSM. Due to the reduction of the number of samples in the filtered design space, the accuracy of the RSM decreases. Table 4.6 presents the parameter importance hierarchy in the form of a top 6. Because of previously explained reasons, only the parameter hierarchy based on the complete design space is shown for the mass response. A more detailed discussion of the results follows, first for the unfiltered and second for the filtered design space. An overview of how the parameter hierarchy is derived and how the PSM is integrated is given by the flow diagram in Figure 4.28.

The hierarchy for the S-rail mass response from Table 4.6 and the results presented in Figure 4.27 show that the influence of laminate thickness t_4 on the S-rail mass is significantly higher than that of the others. This result is trivial and can easily be explained by the fact that section IV of the S-rail has the largest surface area of the 4 sections. Also, a change in laminate thickness increases the mass more than a change in cross-sectional area. This is true for all laminate thickness parameters presented here.

TABLE 4.6. Top 6 in the parameter hierarchy for set 1 and 2 and corresponding total Sobol indices S_{T_i} for the intrusion and mass response.

	Maximum Deformation				**S-rail Mass**	
	Complete		**Filtered**		**Complete**	
nr.	**Par**	S_{T_i}	**Par**	S_{T_i}	**Par**	S_{T_i}
1	t_2	0.33	t_4	0.37	t_4	0.50
2	t_1	0.26	V_{1_S4}	0.12	t_1	0.16
3	V_{1_S1}	0.09	t_2	0.11	t_2	0.15
4	V_{1_S2}	0.08	t_1	0.08	t_3	0.10
5	t_3	0.08	V_{1_S2}	0.06	CS_{4_Z}	0.03
6	CS_{2_Z}	0.06	CS_{2_Z}	0.04	CS_{4_Y}	0.02
Total		0.9		0.78		0.96

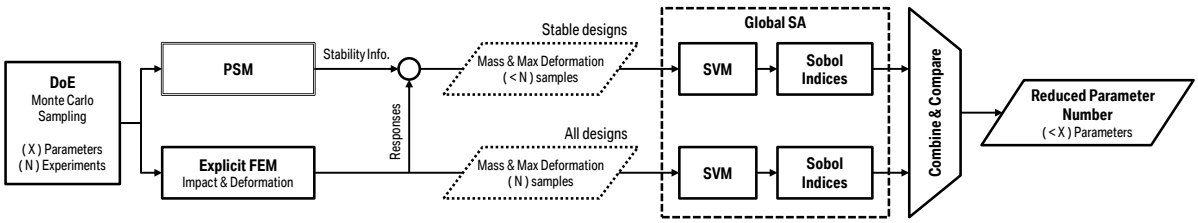

FIGURE 4.28. Flow diagram of phase 1 of the complexity reduction method; derivation of the parameter hierarchy and subsequent reduction of the parameter number. The PSM process in more detail can be found in Figure 3.28b.

Obviously the LPs do not have an influence on the mass and should therefore not appear in the hierarchy. The two small occurrences for V_{1_S1} and V_{1_S4} are only present in the filtered design space and can be attributed to the somewhat reduced quality of the RSM. The mass of the S-rail can directly be derived from the design parameters and therefore the derivation of the influence hierarchy is trivial and the results as expected. There is a reason the mass response of the S-rail was assessed by the presented methods. By using the same method as for all responses, it can be concluded that the Sobol indices for the mass response serve as a partial validation of the method.

The hierarchy for the S-rail maximum deformation response from Table 4.6 and the graph in Figure 4.26 present some interesting results. It is notable that the influence of both laminate thickness parameters t_1 and t_2 for the unfiltered design space are dominant. Parameters t_1 and t_2 are important for the structural stiffness in S-rail

sections I and II. They directly influence the buckling resistance by increasing the structural bending stiffness and laminate membrane stiffness. Additionally the LPs V_{1_S1} and V_{1_S2} are ranked third and fourth in the Sobol hierarchy. LP V_1 has a significant influence on the amount of either 90 or 0 degree orientated plies in the laminate layup. This results in a large influence on the principal stiffness directions as well. Subsequently V_1 has a significant influence on the structural bending stiffness in those material sections. The design parameters t_3 and CS_{2_Z} are ranked fifth and sixth in the hierarchy. The presence of the laminate thickness t_3 in this hierarchy might not be intuitive. However, note that when sections I and II are strong and stiff enough, S-rail section II is the next weak link. The cross-sectional height CS_{2_Z} is last in the top 6 hierarchy.

It is noticeable that the parameters for the laminate thickness have a significantly higher influence on the maximum deformation response than the cross-sectional dimension. It is known that for thin-walled structures ($L_{\text{height}} >> t_{\text{lam}}$), the area moment of inertia is mainly determined by a change in thickness. This is easily checked by looking at the area moment of inertia equation for a hollow, thin walled, rectangular cross-section and its partial derivatives:

$$\begin{aligned} I &= b(6h^2t + 2t^3)/12; \\ \frac{\partial I}{\partial h} &= bht; \\ \frac{\partial I}{\partial t} &= b(h^2 + t^2)/2 \end{aligned} \tag{4.6}$$

where h and b are the cross-sectional height and width respectively and t the wall thickness. The partial derivatives reveal that a change in thickness has a larger effect on I than a change in cross-sectional height. This explains the fact that laminate thickness has a higher importance than the cross-sectional height of the S-rail.

The Sobol indices show that the design parameters influencing the rear most part of the S-rail structure, away from the impact zone, are the most influential. It can be concluded that for the response surface over the complete, unfiltered, design space the design is driven by structural stability and that the parameters, t_1, t_2, V_{1_S1} and V_{1_S2} have the highest influence on that stability.

However, looking at the indices for the filtered design space, see Figure 4.26 and Table 4.6, we see a different hierarchy than with the unfiltered design space. The Sobol indices indicate that section thickness t_4 is the most influential parameter. When the S-rail allows for stable progressive crushing, the maximum deformation is determined by the crush resistance of the material in section IV. The laminate thickness t_4 has a large

TABLE 4.7. Final parameters and their Sobol indices.

nr	Parameter	Max deformation		Mass
		Compl.	Filt.	Compl.
1	t_1	0.26	0.08	0.16
2	t_2	0.33	0.11	0.15
3	t_3	0.08		0.1
4	t_4		0.37	0.5
5	V_{1_S1}	0.09		
6	V_{1_S2}	0.08	0.06	
7	V_{1_S4}		0.12	
8	CS_{2_Z}	0.06	0.04	
Total		0.9	0.78	0.91

influence on this crush resistance. Second in the hierarchy is LP V_{1_S4}. This supports the fact that crush resistance is driving the deformation value in this filtered design space. It is noted that parameters t_2, t_1 and V_{1_S2} are present in the top 6. This shows that the PSM was not able to filter the complete design space perfectly for only structurally stable designs.

On further inspection of the results from Table 4.6, it is noted that there are design parameters in common between the three hierarchies. The parameters CS_{4_Y} and CS_{4_Z} are omitted as they are both almost insignificant and only marginally influential for the mass response. This leads to eight unique parameters: With the parameters presented in Table 4.7 both, the maximum deformation and mass response behavior of the S-rail structure can be captured for both structural stability behaviors around the limit state. It is noted, however, that the sum of Sobol indices using the PSM at the maximum deformation response is relatively low. A value of 0.78 can be interpreted that about 78% of the behavior is captured with the parameters that are chosen for this set. The engineer is responsible for deciding whether that value is sufficient for the problem at hand. For the other sets, more than 90% of the corresponding behavior is captured. It is concluded that the proposed parameter influence hierarchy method resulted in a reduction of variable design parameters from 26 to 8 parameters in an automated manner and with only limited loss of design behavior.

Applying the SSI method The SSI method was explained in Section 3.6.1. The results of the SSI analysis, the new parameter bounds, are shown in Figure 4.29.

The results show that the bounds of laminate thickness parameter t_4 are significantly

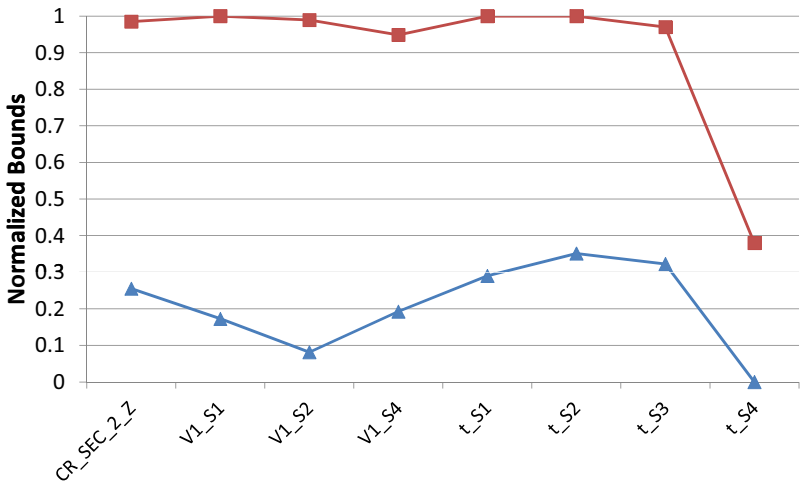

FIGURE 4.29. Design variable upper and lower bounds generated with the SSI method.

reduced. Relative thick laminates for section IV are not prohibited. Laminate thickness for sections I to III, $t_{1,2,3}$, show smaller but still significant reductions. However, the laminates for sections I, II and III are now constraint to a higher minimum thickness. These findings relate well to the findings in the parameter influence hierarchy. There, it was concluded that the laminate thickness in sections I, II and somewhat less in III influence the stability of the structure. In other words, thicker laminates mean higher stability. Furthermore, it was concluded that only laminate thickness t_4 has an influence on the maximum deformation at stable progressive crush behavior. A lower laminate thickness in this section means lower crush stresses and therefore higher deformation. This results in that less force is introduced in the component. This, in turn, reduces the chance of collapse. Noticeable is the reduced lower bound on the cross-sectional height parameter CS_{2_Z}. In the parameter importance hierarchy, the influence was relatively low compared to that of the other parameters. It seems the PSM shows a more significant reaction to a change in this parameter.

Validation of the presented method with the S-rail benchmark At this point the original design problem is significantly reduced in complexity. Originally, the problem consisted of 26 design variables and arbitrarily chosen bounds. After derivation of the design parameter hierarchy and using the proposed PSM, the parameter number was automatically reduced to 8 suitable parameters. The SSI method, also using the proposed

TABLE 4.8. SSI validation.

behavior	**nr**	**%**
Stable	171	85.5
Unstable	29	14.5

PSM, enabled the automated reduction of the parameter bounds to a design space with required structural responses. To validate the new design problem, a new DoE of 200 experiments is performed with the bounds adjusted to the newly derived values and only the 8 design parameters from Table 4.7 are variable.

The results in Table 4.8 show that 85.5% of the experiments are stable. When compared to the first DoE, see Table 4.4, it is a significant improvement. It should be noted however that "stable" means stable progressive crush behavior within S-rail section IV, without the S-rail collapsing during impact. Some other unwanted behavior is still possible with this definition. A more detailed discussion on this is given in the critical reflection.

4.2.2 Optimization of the S-rail problem

In this section, the S-rail is optimized to validate the method for complexity reduction. The original problem started with 26 design variables with arbitrarily chosen bounds. After applying the complexity reduction work-flow the design variables are reduced to 8 with optimized variable boundaries to maximize valid designs. Optimizing the S-rail should show the benefits of the proposed methods.

The optimization problem is formulated as follows: minimize the total S-rail mass constrained by a maximum intrusion of 350 mm. See Figure 4.22 for a description of the crash scenario.

Differential Evolution (DE) is used as the optimization algorithm [100]. This algorithm is part of a family of stochastic search algorithms and does not require the calculation of sensitivities. It is widely used in literature and generally provides good results in terms of convergence speed and finding global optima for NP-hard problems. It is therefore well-suited for our current problem.

To test the complexity reduction, two different settings for the DE algorithm are applied to the S-rail problem, both before and after the complexity reduction. The settings for the DE algorithm differ in the population number of allowed iterations. These two parameters define how many function evaluations are made per iteration

TABLE 4.9. Setup parameters for the DE algorithm, all units are dimensionless.

Parameter	**Value**
Population Size	10 or 40
Maximum Iterations	30 or 25
Maximum Function Evaluations	300 or 1000
Weight Factor	0.7
Step Width	0.5
Average Stop Width	0.01
Inverse Crossover Probability	0.85

(population) and the total possible evaluations (population x iterations). The choice for the optimization parameters is often a trade-off between a robust optimization performance and computational efficiency. More evaluations per iteration will generally provide a higher chance of finding a global optimum, at the cost of computational time. The number, however, should be higher than 7, otherwise the algorithm gets stuck in an endless loop. The population size and maximum number of iterations are chosen such that both, a quick but narrow (low number of evaluations) and slow but broad search (large number of evaluations) are performed. The other setup parameters are chosen based on common praxis. The DE setup parameters are summarized in Table 4.9.

First, the optimization with the large population per iteration is performed. This setup reflects an robust optimization, but one that is computationally less efficient, i.e. requiring a relatively large number of evaluations. The optimization is performed on the S-rail before complexity reduction (Figure 4.30) and after complexity reduction (Figure 4.31). When comparing both cases, the following is noted. The optimization on the original S-rail problem results in a better optimum (lower mass) than after complexity reduction (see Figures 4.30a and 4.31a). This is explained by the fact that certain valid design possibilities are lost after removing less influential parameters and setting narrower variable bounds. However, it is also noted that far less invalid designs are evaluated on the problem after complexity reduction. Also the convergence behavior (bandwidth of evaluations as iterations progress) is better after complexity reduction. Nevertheless, the DE algorithm was able to find a better optimum quicker with the original S-rail (in less iterations) than when performed on the S-rail after complexity reduction. This could have been expected, because the DE algorithm performs best when allowed to evaluate high numbers of designs in each iteration.

To show the benefit of the complexity reduction scheme, the optimization is performed

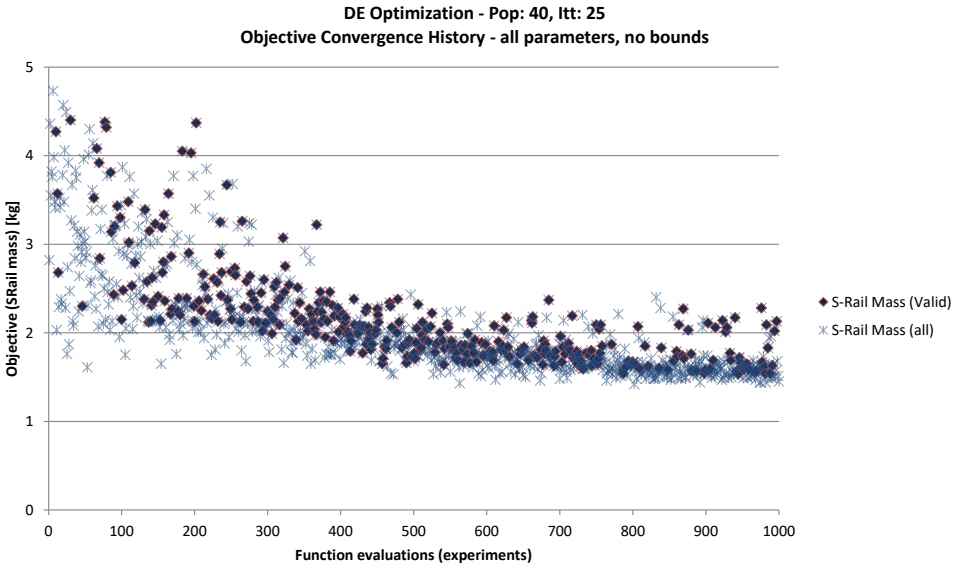

(a) The convergence of the objective (S-rail mass)

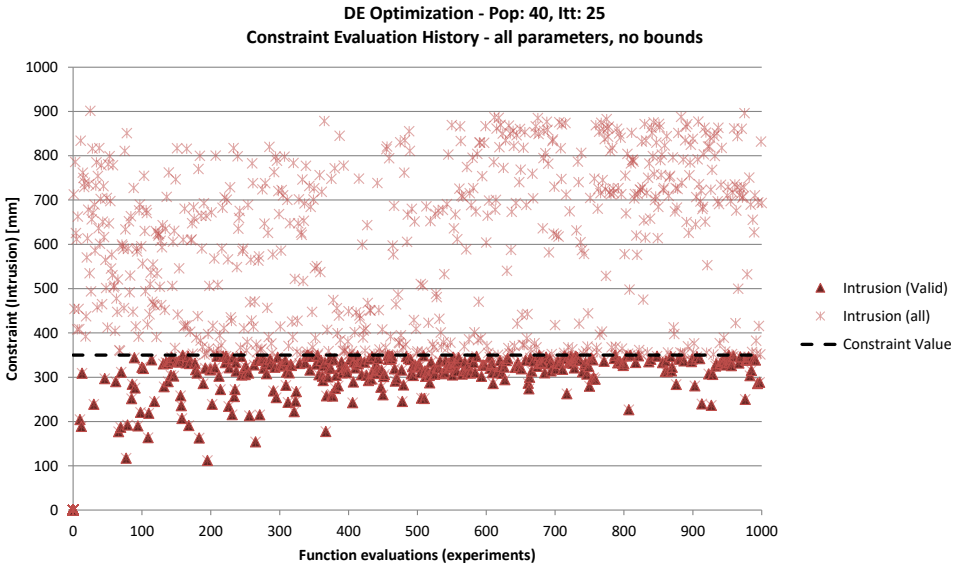

(b) The evaluations of the constraint function (intrusion)

FIGURE 4.30. The evaluation history of the objective and constraint functions for the original (unadapted) S-rail problem. The difference between valid (constraint is met) and invalid designs is made visible.

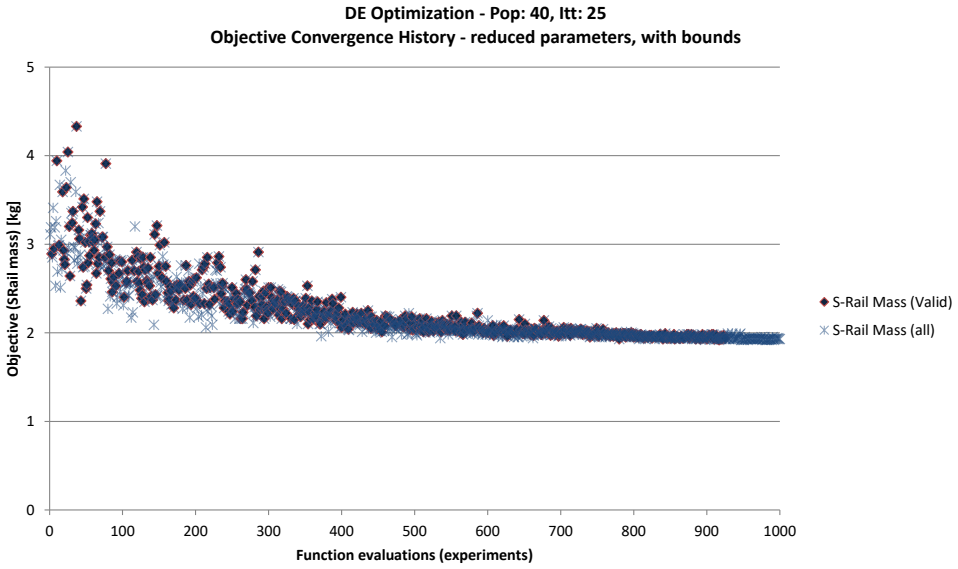

(a) The convergence of the objective (S-rail mass)

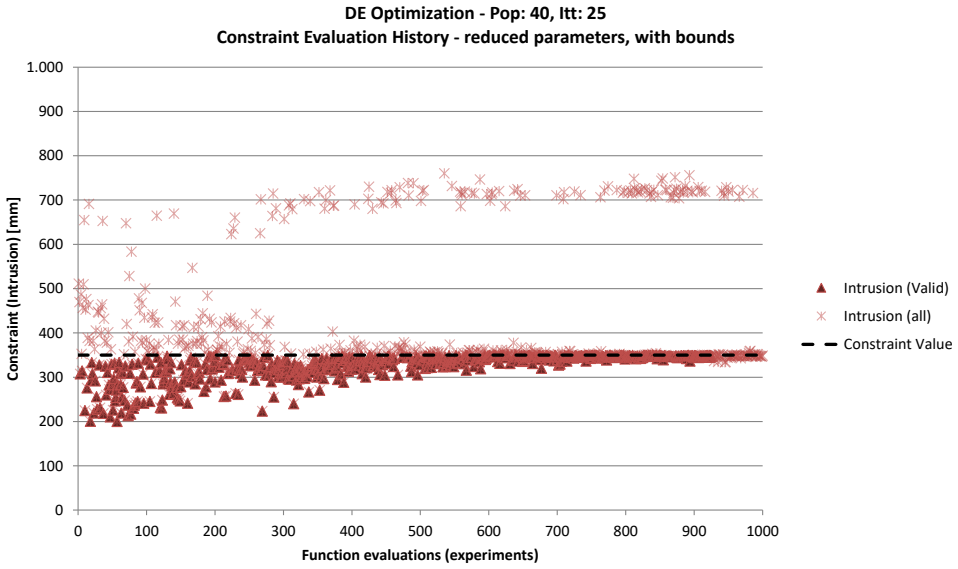

(b) The evaluations of the constraint function (intrusion)

FIGURE 4.31. The evaluation history of the objective and constraint functions for the S-rail problem after complexity reduction. The difference between valid (constraint is met) and invalid designs is made visible.

again, but this time with settings that benefit computational efficiency. Now, the population per iteration is set to 10 and again the optimization is performed on the S-rail before and after complexity reduction. The results are shown in Figures 4.32 and 4.33. After comparing the results, again the optimization on the S-rail after complexity reduction shows significantly less invalid evaluations. Furthermore, the optimization finds a better optimum in less evaluations than when performed on the S-rail before complexity reduction. Also noted are the “cleaner” histories in Figure 4.33 when compared to Figure 4.32.

By applying the complexity reduction to the S-rail problem, the optimization algorithm was able to find a good optimum efficiently (less evaluations), than when performed on the original. This is of significant benefit when design evaluations require high computation times, such as in the case of composite structure crash simulations. Indeed, when allowing for larger number of evaluations, the optimization can find better optima comparably quick on the original problem. However, the presented S-rail problem is of relatively low complexity, when compared to actual industry relevant design problems. The benefits of the proposed work-flow are expected to increase with increasing problem complexity.

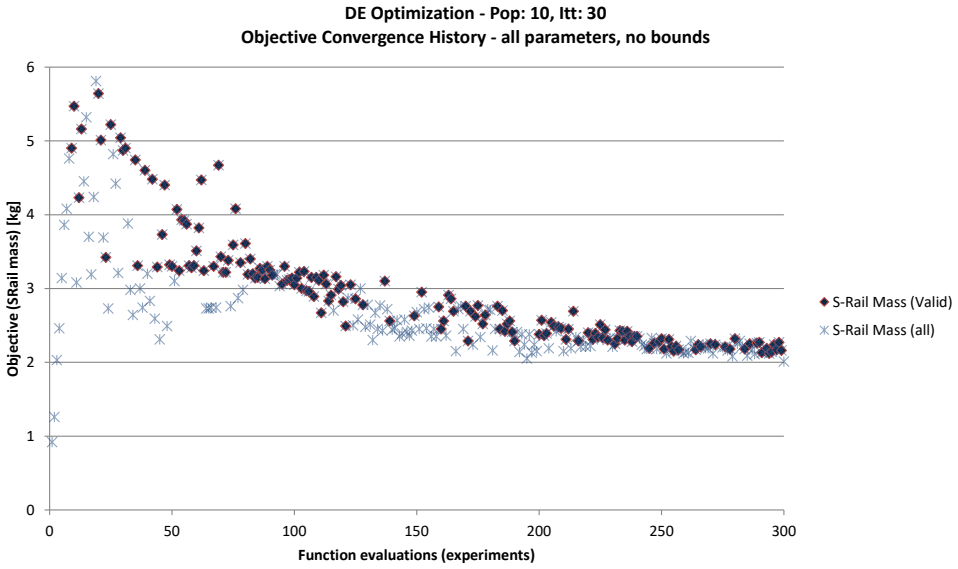

(a) The convergence of the objective (S-rail mass)

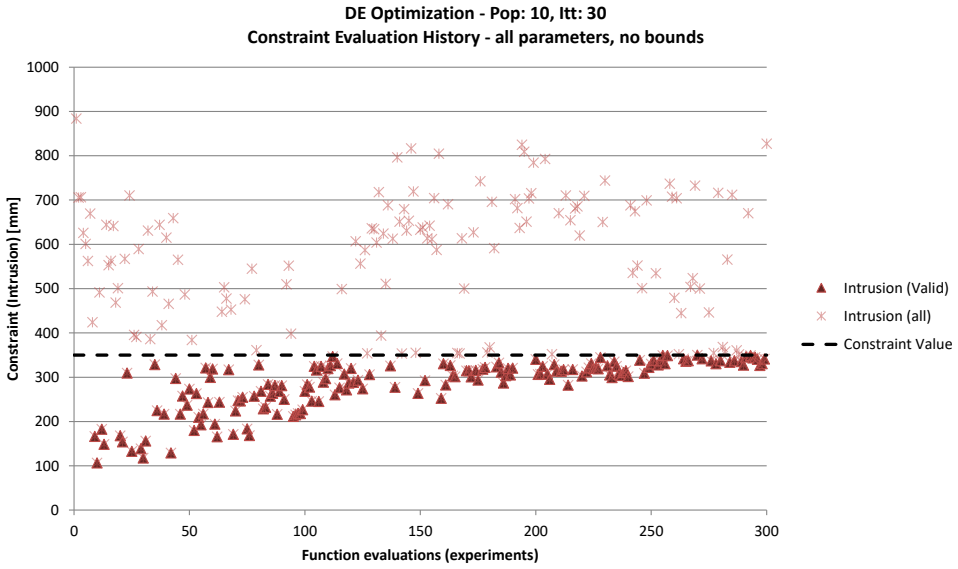

(b) The evaluations of the constraint function (intrusion)

FIGURE 4.32. The evaluation history of the objective and constraint functions for the original (unadapted) S-rail problem. The difference between valid (constraint is met) and invalid designs is made visible.

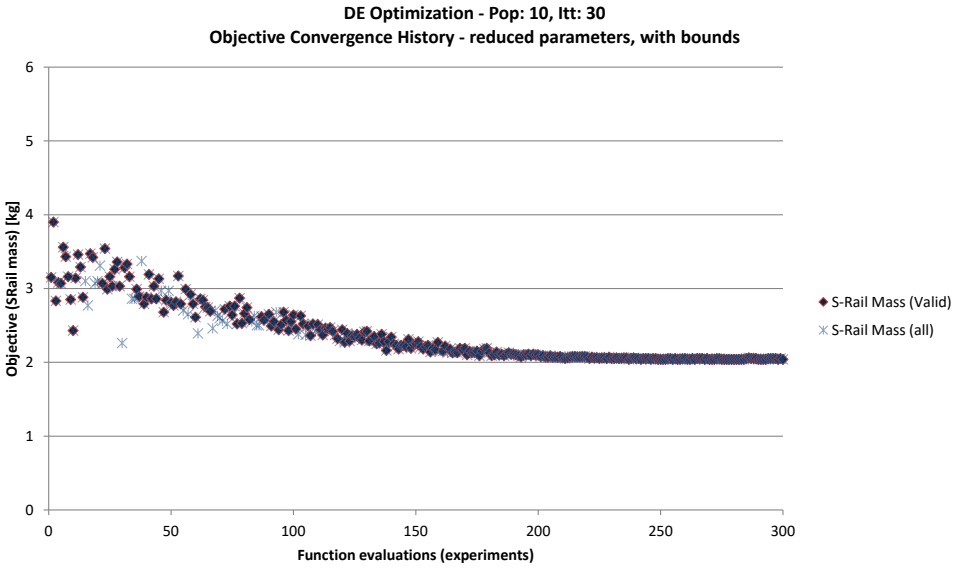

(a) The convergence of the objective (S-rail mass)

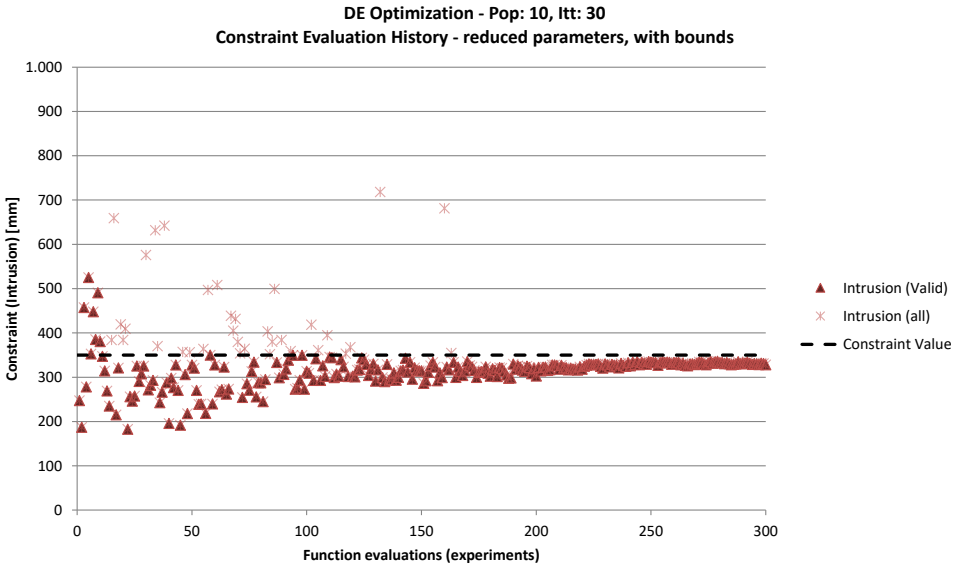

(b) The evaluations of the constraint function (intrusion)

FIGURE 4.33. The evaluation history of the objective and constraint functions for the S-rail problem after complexity reduction. The difference between valid (constraint is met) and invalid designs is made visible.

CHAPTER 5

DISCUSSION & OUTLOOK

5.1 Shape Optimization

5.1.1 Implementation of the LSM with local volume constraints

The shape optimization with the LSM as presented in the methods chapter in Section 3.4 works well, but is not without challenges. Some of these challenges are discussed next.

Oscillatory behavior In some cases oscillatory behavior around the optimum could be seen, on both the objective and constraint values. Especially in the first example, with the three-point-bending problem, this issue was present. It was expected that the introduction of extra Lagrange Multipliers would increase instability in the convergence history. Two possible solutions might mitigate this issue:

- A method to decrease the time step Δt in the LSM update procedure as soon as oscillatory behavior is detected. This method was used in the application of the method on the composite vehicle front in the application chapter.
- Development and use of better Lagrange multiplier update methods. This thesis provides a first look into the use of sub-domain specific volume constraints. The presented multiplier update methods work well for this purpose. However, the author realizes that better update algorithms are available and future research on this topic should reflect that.

Problem Initialization The distribution and size of the holes for the problem initialization has a significant effect on the final optimized topology. Indeed, any kind of initial geometry / shape description will show its influence on the final results. The introduction of local volume constraints increases the sensitivity to problem initialization. The dependence of the problem's initial design on the shape / topology optimization result is a well known issue within this field of research. It can be expected that the introduction of extra constraints increases this dependence. The research presented here did not focus on this issue and its effects, which are left for future developments.

Mesh Size The mesh used for both validation examples is the same and consists of relatively large elements. It is expected that a smaller mesh size will improve the results considerably, removing many of the artifacts shown in the topology results.

5.1.2 Mapping between 3D transient dynamic and 2D static linear domains

In this thesis, the composite structure, or parts of it, including its relevant structural behavior during impact, need to be translated onto a 2D domain for shape optimization. In the proposed methods, the structure undergoes several simplifications, such as flattening of the longitudinal stiffeners to remove the out-of-plane curvature. For the sake of scope, these simplifications are allowable. However, valuable mechanical information is of course lost. The author researched using 3D LSM based shape optimization, but the benefit of using the LSM is largely lost in this case. Geometrical boundary crossing is much more present in 3D as in 2D and, therefore shape control is comparably less. Furthermore, 3D shape optimization with the LSM is, as is with the SIMP method, only possible with solid elements. Hollow shell structures, such as composite beams, cannot be directly represented. However, in hindsight, the local volume method should work just as well in 3D, although stable convergence would be a challenge. The local volume method could also enforce relative constant cross-sectional designs. These constant cross-sections would be subject to the same problems as in 2D (see the next section). However, they could allow for a significantly better translation into hollow shell profiles. This idea should be pursued in further research.

5.1.3 Composite crush relevant constraints with local volumes

The idea behind the addition of local volume constraints in the shape optimization is to gain more control over the shape evolution during optimization. This way, the optimization can be steered to find structures that benefit the dynamics behind composite crush and energy absorption. The theory behind this idea was explained in the methods chapter. However, the behavior relevant discrepance between the highly non-linear crush mechanics of a CFRP composite beam profile and a 2D representation in the static linear domain is very large. Therefore, many of the mechanical characteristics are lost in the transition. The methods proposed in this thesis provide a very first step in this direction, but should be further developed. The local volume method was able to steer the shape optimization to develop slender, constant cross-section, beam-like structures in the energy absorbing part of the design domain. The constant cross-section helps in the manufacturability and the slenderness of the beams means that they only take up minimal energy when impacted. Be that as it may, the constant cross-section did not provide the constant crush force during impact as was intended. This is of course a result of the instability of the optimized members of the support structure. As they are impacted, their angle towards the impacting surface does not allow for a stable crush front. As a result, the members buckle and bend away. Although this behavior is not necessarily negative, it is not part of the explicitly intended optimization goals. Indeed, it is more of a side effect, which, however, can be steered with the local volume constraints. The author therefore does not consider the method to be without purpose or a failure. Nevertheless, more research is necessary.

5.2 Complexity Reduction

The structural stability is approximated comparably well with the PSM method of the LiSF. Nevertheless, this only takes collapse and global buckling type failure into account. It should be noted again, that here no transient dynamic crashworthiness assessment is made of the structure. Another form of undesired structural behavior is that stable crushing continues up to the end of section IV. At this point the impactor encounters a new material which may increase the impacting force resulting in structural failure or allow continued crushing. Both are undesirable as either failure occurs or the maximum allowed deformation is exceeded. Taking these considerations into account, some new definitions on structural behavior type are created:

- **Limit State** All experiments which showed a structural response below the limit state for the S-rail benchmark. This is equal to the limit of what the PSM can predict.
- **Stable** All experiments which showed stable crush behavior with a maximum deformation of 400 mm, the length of section IV.
- **Semi Stable** All experiments which showed stable crush behavior up until and over a maximum of 400 mm. This means the crushing is continued into section III. The S-rail does not collapse.
- **Unstable** All experiments which showed unstable behavior. In these cases the S-rail collapsed during impact without reaching a maximum deformation of 400 mm.
- **Semi unstable** All experiments which showed unstable behavior when the crush front reached into section III, meaning the maximum of 400 mm deformation was exceeded.

The validation DoE (see Table 4.8) is reevaluated with these new definitions on structural behavior. The results are shown in Table 5.1. The results show that here 63%

Table 5.1: SSI validation.

Behavior	**nr**	*%*
Limit State	193	96.5
Stable	126	63
Semi Stable	45	22.5
Unstable	7	3.5
Semi Unstable	22	11

of the experiments can be considered fully stable, meaning 37% showed some kind of instability. Considering that the methodology performed on the S-rail benchmark does not account for such a thorough behavior assessment, the results may be considered good. Furthermore, the reduced design problem is most likely used in an optimization framework, as the one applied in Section 4.2.2. Here, a constraint can be set on the maximum deformation, for instance the 350 mm that was applied previously. This will result in mitigating both the semi-stable and semi-unstable results. However, this would mean invalid designs are still a possibility in the reduced design space of the S-rail problem. These invalid designs were therefore also part of the solution space during optimization on the complexity reduced S-rail.

CHAPTER 6

CONCLUSION

In this thesis a work-flow is presented to methodically handle different issues concerning the optimization of the crashworthiness of automotive structures. The structural problems make use of advanced composite laminates as the main structural material, adding complexity to the optimization problem. The proposed novel design work-flow addresses different aspect of the optimization process; shape optimization and complexity reduction. A two part method is introduced. The first part is concerned with the optimization of load paths, taking crash loads and composite crush behavior into consideration. Also the translation from 3D crash scenarios to 2D shape optimization domains and back is researched and a solution is presented. The second part introduces a complexity reduction work-flow that can be applied to the design from the first part.

The first part is based on a Level Set type shape optimization for crash. Shape optimization is used to improve the structural stability in the early phase of development of crash loaded composite structures. Use is made of shape optimization to create structural solutions with clear and smooth material boundaries. A composite vehicle concept and the non-linear explicit crash-simulation results are used in a multi-stage optimization work-flow to create load cases for optimization in the 2-D domain. A novel local volume constraint method is introduced to provide control over shape development. This enhanced control supports the creation of shapes that are beneficial for reducing force peaks during the energy absorption phase of the impact. Other properties of the novel optimization framework are a coupling of the explicit 3D crash domain to an implicit 2D Level Set Method (LSM) optimization domain using new mapping methods and a

variation of the Equivalent Static Load (ESL) method to transform impact behavior into corresponding load cases. The resulting optimized material boundaries are described in terms of finite elements and continuous splines.

The second part introduces a complexity reduction method for automotive composite structures with respect to crashworthiness. A combination of a new type of physical surrogate model and sensitivity analysis are used to reduce the number of design parameters without significantly compromising the possible solution space. The Lamination Parameter (LP) method is used to efficiently characterize composite laminates. The Solution Space Identification (SSI) methodology is used to identify optimal boundaries for the remaining parameters.

The optimization framework introduced in the first part is applied on a basic initial vehicle design with some essential structural components integral for the crashworthiness of the vehicle. These components are necessary components to absorb crash energy, for example longitudinal front rails, which are pre-specified from prior decisions and knowledge. These structures are initially unstable in crash and cannot fulfill their function as energy absorbing components. The components have to have a high level of structural stability, in order to have stable and progressive crush behavior. The presented optimization framework serves to find an optimal structural support system (load paths) to support these primary components in their optimal crash function for the duration of the crash and for multiple crash load cases. The method implements an outer and an inner optimization loop. The outer loop starts with a non-linear explicit crash simulation to assess the structural stability. A time point (snap-shot) is determined at which the structure becomes unstable. Then, a method to map a 3D structure to a 2D representation of the design space is applied. An adapted ESL method is introduced and used to derive a (multi)-load case from the snap-shot. The inner loop applies the LSM in the 2D domain to find an optimal shape of the supportive composite structure to stabilize the vehicle concept. Finally, a method to map the 2D optimization results back to the 3D vehicle structure is introduced. The result is crashed in an explicit simulation and the outer loop starts again, until the structure is stable for the duration of the crash.

The second part of the proposed design optimization work-flow is concerned with the reduction of complexity of crashworthiness optimization problems. The introduction of advanced composite materials into the design of crashworthy automotive structures increases the complexity of the already complex design development. The number of design parameters, the complex non-linear mechanical behavior and the high computational costs are the reason a new systematic approach to reduce design complexity

is introduced. The method touches on the three complexity increasing factors; the high number of design variables, mechanical behavior, and computational cost. The approach consists of a novel work-flow, where the complexity is reduced in two stages. In the first stage, a parameter importance hierarchy is derived. In the second stage, a Solution Space Identification (SSI) method is used to define new parameter boundaries. Both stages are designed to reduce the design space complexity. On top of this, a Physical Surrogate Model (PSM) is developed to approximate a Limit State Function (LiSF) that is applied in both stages to reduce the mechanical behavior complexity and increase the computational efficiency.

As a result of this method the original design problem is significantly reduced in complexity. Firstly, only the most influential parameters are used as the optimization variables. Less variables increases the convergence speed and increases the change to find a global optimum. Secondly, the variable bounds and thereby the design domain of the problem will mostly consist of feasible, stable design. This increases the stability of the optimization and increases again the convergence speed and chance of finding a global optimum. Because of these results the optimization of the problem is now less difficult.

The presented methods are applied on two distinct problems, relevant in the field of automotive crashworthiness. First is the optimization of the CFRP composite support structure for the impact loaded front architecture of a novel vehicle design. Second is the optimization of an S-rail before and after the complexity reduction.

The load cases for the first application are a full overlap frontal impact on a rigid wall perpendicular to the impact and an impact on a rigid 30° oblique wall. These are both load-cases that are part of the regulatory requirements in the USA and part of the FMVSS208 regulations. The application of the presented optimization methods shows promising results. The design work-flow is able to find supportive structures that enable progressive crushing of the vehicle front for the duration of the impact. Two outer loop iterations were necessary to achieve this. The local volume constraints in both iterations influenced mainly the shape of the structure in the deformation area. In both cases, the direct influence on the crush force by having a constant cross-sectional area in X-direction is minimal, as parts of the optimized support structure buckle and move away without significant crushing. However, the local volume constraints do influence the slenderness of the optimized shape, without compromising on the global volume constraint. This in turn does influence the overall crash response of the structure. The slender members in the optimized structures break or buckle away from the crush-front easier as soon as the

crush-front passes the joint area to the initial vehicle concept. And consequently, this reduces the overall impact on the deceleration pulse of the vehicle.

The second application problem is solved with the complexity reduction method and consists of a parametric tubular structure with a single S-shaped bend. This represents a simplified vehicle S-rail. The example is relatively simple for a design problem, but shows enough complexity, including combinations of bending, local and global buckling and axial crush of the composite material. The simplified S-rail is fully clamped at its roots and is impacted by a rigid surface.

The initial problem setup has 26 design variables with arbitrarily chosen bounds. After applying the complexity reduction work-flow, the parameter number was automatically reduced to 8 suitable parameters. The SSI method, also using the proposed PSM, enabled the automated reduction of the parameter bounds to a design space with required structural responses. To validate the new design problem, a new DoE of 200 experiments was performed with the bounds adjusted to the newly derived values and only the 8 design variables. The results show that 85.5% of the experiments are stable, which is a significant improvement.

To test the effectiveness of the complexity reduction, a Differential Evolution (DE) based optimization is applied to the S-rail problem, both before and after the complexity reduction. Two different setups, with either high or low computational effort required, for the DE algorithm are applied.

First, the optimization with the large population per iteration is performed. This setup reflects a robust optimization, but one that is computationally less efficient. The results show a better optimum (lower mass) for the S-rail before complexity reduction. However, it is also noted that far less invalid designs are evaluated on the problem after complexity reduction. Also the convergence behavior (bandwidth of evaluations as iterations progress) is better after complexity reduction. Nevertheless, the DE algorithm was able to find a better optimum quicker with the original S-rail (in less iterations) than when performed on the S-rail after complexity reduction.

Secondly, the optimization is performed again, but this time with settings that benefit computational efficiency. After comparing the results, again the optimization on the S-rail after complexity reduction shown significantly less invalid evaluations. Furthermore, the optimization finds a better optimum in less evaluations than when performed on the S-rail before complexity reduction. Also noted are the cleaner optimization histories when compared to the histories before complexity reduction.

By applying the complexity reduction to the S-rail problem, the optimization algo-

rithm was able to find a good optimum efficiently (less evaluations), than when performed on the original. This is of significant benefit when design evaluations require high computation times, such as in the case of composite structure crash simulations.

APPENDIX A

DERIVATIVES

The Lagrangian $\mathscr{L}$ is derived in order to transform the inequality constrained optimization problem into an unconstrained problem:

$$\mathscr{L}(\phi(\vec{x})) = c(\phi(\vec{x})) + \lambda \left(g(\phi(\vec{x})) + s^2 \right) \tag{A.1}$$

where s is a slack variable which converts the inequality into an equality constraint. The optimum is defined by meeting the KKT optimality conditions.

Let us take the compliance equal to the total strain energy:

$$c = \vec{u}^T \cdot \vec{\vec{K}} \cdot \vec{u}. \tag{A.2}$$

The stiffness matrix $\vec{\vec{K}}(\vec{\rho})$ is determined as follows:

$$\vec{\vec{K}}(\vec{\rho}) = \bigcup_{e=1}^{N_e} \rho_e(\phi) \vec{K}_e \tag{A.3}$$

where $\bigcup$ denotes the assembly of element components, N_e is the total number of elements, $\vec{K}_e$ is the element stiffness matrix and ρ_e is the element density determined by the LSF values. The strain energy density can be determined as follows:

$$\begin{aligned} c &= \textstyle\sum_{e=1}^{N_e} \rho_e(\phi) \vec{u}_e^T \cdot \vec{K}_e \cdot \vec{u}_e \\ &= \textstyle\sum_{e=1}^{N_e} \tilde{H}\left(\phi(\vec{x})\right) \vec{u}_e^T \cdot \vec{K}_e \cdot \vec{u}_e. \end{aligned} \tag{A.4}$$

The shape derivative of the Lagrangian $\mathscr{L}$ is derived as the Fréchet derivative with respect to ϕ as follows:

$$\frac{\mathrm{d}\mathscr{L}}{\mathrm{d}\Omega} = \left\langle \frac{\mathrm{d}\mathscr{L}}{\mathrm{d}\phi}, \psi \right\rangle \tag{A.5}$$

where ψ is the variation of the level set function such that $\psi \in \Psi$. Combining Equations (A.1) and (A.5), we get:

$$\frac{\mathrm{d}\mathscr{L}}{\mathrm{d}\Omega} = \frac{\mathrm{d}c}{\mathrm{d}\Omega} + \lambda \frac{\mathrm{d}g}{\mathrm{d}\Omega}. \tag{A.6}$$

A.1 Shape Derivative of the Compliance

Now let us define the shape derivative of the strain energy density as the Fréchet derivative with respect to ϕ:

$$\frac{\mathrm{d}c}{\mathrm{d}\Omega} = \left\langle \frac{\mathrm{d}c}{\mathrm{d}\phi}, \psi \right\rangle. \tag{A.7}$$

Now by rule of total derivative, Equation (A.7) can be rewritten as follows:

$$\begin{aligned} \left\langle \frac{\mathrm{d}c}{\mathrm{d}\phi}, \psi \right\rangle &= \left\langle \frac{\partial c}{\partial \phi}, \psi \right\rangle + \left\langle \frac{\partial c}{\partial \vec{u}} \frac{\mathrm{d}\vec{u}}{\mathrm{d}\phi}, \psi \right\rangle \\ &= \left\langle \frac{\partial c}{\partial \phi}, \psi \right\rangle + \left\langle \frac{\partial c}{\partial \vec{u}}, \vec{w} \right\rangle. \end{aligned} \tag{A.8}$$

The partial derivatives from Equation (A.8) are derived as follows:

$$\begin{aligned} \frac{\partial c}{\partial \phi} &= \sum_{e=1}^{N_e} \tilde{\delta}\left(\phi(\vec{x})\right) \vec{u}_e^T \cdot \vec{K}_e \cdot \vec{u}_e; \\ \frac{\partial c}{\partial \vec{u}} &= \sum_{e=1}^{N_e} \tilde{H}\left(\phi(\vec{x})\right) 2\vec{K}_e \cdot \vec{u}_e. \end{aligned} \tag{A.9}$$

The Fréchet derivatives for the condition $\vec{\vec{K}}\vec{u} - \vec{f}^{\text{ext}} = 0$ are as follows:

$$\begin{aligned} \frac{\mathrm{d}\vec{f}^{\text{ext}}}{\mathrm{d}\Omega} &= 0; \\ \frac{\mathrm{d}\vec{a}}{\mathrm{d}\Omega} &= \left\langle \frac{\mathrm{d}\vec{a}}{\mathrm{d}\phi}, \psi \right\rangle = \left\langle \frac{\partial \vec{a}}{\partial \phi}, \psi \right\rangle + \left\langle \frac{\partial \vec{a}}{\partial \vec{u}}, \vec{w} \right\rangle \end{aligned} \tag{A.10}$$

where $\vec{a} = \vec{\vec{K}}\vec{u}$. The partial derivatives from Equation (A.10) are derived as follows:

$$\begin{aligned} \frac{\partial \vec{a}}{\partial \phi} &= \sum_{e=1}^{N_e} \tilde{\delta}\left(\phi(\vec{x})\right) \vec{K}_e \cdot \vec{u}_e; \\ \frac{\partial \vec{a}}{\partial \vec{u}} &= \sum_{e=1}^{N_e} \tilde{H}\left(\phi(\vec{x})\right) \vec{K}_e. \end{aligned} \tag{A.11}$$

From combining Equations (A.10) and (A.11) follows:

$$\begin{aligned} &\left\langle \frac{\partial \vec{a}}{\partial \vec{u}}, \vec{w} \right\rangle = -\left\langle \frac{\partial \vec{a}}{\partial \phi}, \psi \right\rangle; \\ &\textstyle\sum_{e=1}^{N_e} \tilde{H}\left(\phi(\vec{x})\right) \vec{K}_e \cdot \vec{w} = \dots \\ &\quad -\textstyle\sum_{e=1}^{N_e} \tilde{\delta}\left(\phi(\vec{x})\right) \vec{K}_e \cdot \vec{u}_e \psi. \end{aligned} \tag{A.12}$$

Now combining Equations (A.8) and (A.9) and substituting Equation (A.12), we get the following:

$$\begin{aligned} \frac{\mathrm{d}c}{\mathrm{d}\Omega} = &\textstyle\sum_{e=1}^{N_e} \tilde{\delta}\left(\phi(\vec{x})\right) \vec{u}_e^T \cdot \vec{K}_e \cdot \vec{u}_e \psi + \dots \\ &\textstyle\sum_{e=1}^{N_e} \tilde{H}\left(\phi(\vec{x})\right) 2\vec{K}_e \cdot \vec{u}_e \cdot \vec{w} \\ = &\textstyle\sum_{e=1}^{N_e} \tilde{\delta}\left(\phi(\vec{x})\right) \vec{u}_e^T \cdot \vec{K}_e \cdot \vec{u}_e \psi - \dots \\ &\textstyle\sum_{e=1}^{N_e} 2\tilde{\delta}\left(\phi(\vec{x})\right) \vec{u}_e^T \cdot \vec{K}_e \cdot \vec{u}_e \psi. \end{aligned} \tag{A.13}$$

This leads to the following relation for the shape derivative of the strain energy density:

$$\frac{\mathrm{d}c}{\mathrm{d}\Omega} = -\sum_{e=1}^{N_e} \tilde{\delta}\left(\phi(\vec{x})\right) \vec{u}_e^T \cdot \vec{K}_e \cdot \vec{u}_e \psi. \tag{A.14}$$

A.2 Shape Derivative of the Global Volume Constraint

The derivation of the shape derivative of the volume constraint follows the same procedure as with the compliance. The volume V is expressed as follows:

$$V(\phi(\vec{x})) = \sum_{e=1}^{N_e} \tilde{H}\left(\phi(\vec{x})\right). \tag{A.15}$$

The shape derivative of the constraint $g(\phi(\vec{x}))$ is derived as follows:

$$\frac{\mathrm{d}g}{\mathrm{d}\Omega} = \left\langle \frac{\mathrm{d}g}{\mathrm{d}\phi}, \psi \right\rangle = \left\langle \frac{\partial g}{\partial \phi}, \psi \right\rangle. \tag{A.16}$$

This leads to the following definition of the constraint shape derivative:

$$\frac{\mathrm{d}g}{\mathrm{d}\Omega} = \sum_{e=1}^{N_e} \tilde{\delta}\left(\phi(\vec{x})\right) \psi. \tag{A.17}$$

A.3 Shape Derivative of the Lagrangian

The shape derivative of the Lagrangian can now be defined by substituting the results from Equations (A.14) and (A.17) into Equation (A.6) and taking the derivative with respect to the LSF values:

$$\frac{\mathrm{d}\mathscr{L}}{\mathrm{d}\phi} = \sum_{e=1}^{N_e} \tilde{\delta}\left(\phi(\vec{x})\right)\left[-\vec{u}_e^{\,T} \cdot \vec{K}_e \cdot \vec{u}_e + \lambda\right]. \tag{A.18}$$

The boundary normal velocity $V_N(\vec{x},t)$ can now be defined as:

$$V_N(\vec{x},t) = \frac{\mathrm{d}\mathscr{L}}{\mathrm{d}\phi}. \tag{A.19}$$

The Lagrangian formulation of the optimization problem contains a slack variable s to account for the inequality constraint. The switching condition from the KKT conditions can be satisfied in two ways:

- $\lambda = 0$: This implies that the inequality condition is inactive, meaning that the suggested optimum features a lower volume fraction than $V_{\max}$. However, for problems with fixed boundary conditions and fixed loads, not considering body forces, the compliance is minimized when the design domain is completely filled with material. This fact makes this case physically irrelevant.
- $s = 0$: Zero slack implies an active inequality constraint, $g(\phi) = 0$, indicating that $V(\phi) = V_{\max}$ for the optimum solution.

These cases show that the optimum will always lie at $V(\phi) = V_{\max}$. As a result of this, one could define the volume constraint in Equation (3.4) as an equality constraint. The slack variable s is now redundant and omitted.

BIBLIOGRAPHY

[1] Noesis optimus. https://www.noesissolutions.com/

[2] ABAQUS/Standard User's Manual. Dassault Systèmes Simulia Corp, United States (2013)

[3] Clearvu analytics. https://divis-gmbh.de/home/software/clearvu-analytics/ (2015)

[4] Allaire, G., Gournay, F.D., Jouve, F., Toader, A.M.: Structural optimization using topological and shape sensitivity via a level set method. Control and cybernetics **34**, 59 (2005)

[5] Allaire, G., Jouve, F.: Minimum stress optimal design with the level set method. Engineering Analysis with Boundary Elements **32**(11), 909–918 (2008). DOI 10.1016/j.enganabound.2007.05.007

[6] Allaire, G., Jouve, F., Toader, A.M.: A level-set method for shape optimization. Comptes Rendus Mathématique **334**(12), 1125–1130 (2002). DOI 10.1016/S1631-073X(02)02412-3

[7] Allaire, G., Jouve, F., Toader, A.M.: Structural optimization using sensitivity analysis and a level-set method. Journal of Computational Physics **194**(1), 363–393 (2004). DOI 10.1016/j.jcp.2003.09.032

[8] Arora, J.S.: Introduction to Optimum Design. Academic Press (2012)

[9] Arwade, S.R., Moradi, M., Louhghalam, A.: Variance decomposition and global sensitivity for structural systems. Engineering Structures **32**(1), 1–10 (2010). DOI 10.1016/j.engstruct.2009.08.011

[10] Avalle, M., Chiandussi, G., Belingardi, G.: Design optimization by response surface methodology: Application to crashworthiness design of vehicle structures. Structural and Multidisciplinary Optimization **24**(4), 325–332 (2002). DOI 10.1007/s00158-002-0243-x

[11] Barnes, G., Coles, I., Roberts, R.: Crash safety assurance strategies for future plastic and composite intensive vehicles (PCIVs). Tech. rep., US Department of Transportation, Research and Innovative Technology Administration, Volpe National Transportation Systems Center (2010)

[12] Barnes, G., Nixon, S., Schrank, M.: Composite crush simulation-emerging technologies and methodologies. In: NAFEMS World Congress (2009)

[13] Belingardi, G., Beyene, A.T., Koricho, E.G.: Geometrical optimization of bumper beam profile made of pultruded composite by numerical simulation. Composite Structures **102**, 217–225 (2013). DOI 10.1016/j.compstruct.2013.02.013

[14] Bendsøe, M.P., Sigmund, O.: Material interpolation schemes in topology optimization. Archive of Applied Mechanics **69**(9-10), 635–654 (1999). DOI 10.1007/s004190050248

[15] Bojanowski, C., Kulak, R.F.: Multi-objective optimisation and sensitivity analysis of a paratransit bus structure for rollover and side impact tests. International Journal of Crashworthiness **16**(6), 665–676 (2011). DOI 10.1080/13588265.2011.616118

[16] Borg, R., Nilsson, L., Simonsson, K.: Simulation of delamination in fiber composites with a discrete cohesive failure model. Composites Science and Technology **61**(5), 667–677 (2001). DOI 10.1016/S0266-3538(00)00245-1

[17] Bruggi, M., Duysinx, P.: Topology optimization for minimum weight with compliance and stress constraints. Structural and Multidisciplinary Optimization **46**(3), 369–384 (2012). DOI 10.1007/s00158-012-0759-7

[18] Bujny, M.: Level set topology optimization for crashworthiness using evolutionary algorithms and machine learning. Ph.D. thesis, Technische Universität Munich, Germany (2020)

[19] Bujny, M., Aulig, N., Olhofer, M., Duddeck, F.: Identification of optimal topologies for crashworthiness with the evolutionary level set method. International Journal of Crashworthiness **23**(4), 395–416 (2017). DOI 10.1080/13588265.2017.1331493

[20] Cacuci, D.G.: Sensitivity & Uncertainty Analysis, Volume 1: Theory. Chapman and Hall/CRC (2003)

[21] Carruthers, J.J., Kettle, A.P., Robinson, A.M.: Energy Absorption Capability and Crashworthiness of Composite Material Structures: A Review. Applied Mechanics Reviews **51**(10), 635 (1998). DOI 10.1115/1.3100758

[22] Castro, J.M.P.B.C., Fontana, M., Araujo, A.L., Madeira, J.F.A.: Optimization of a composite impact attenuator for a formula student car. Mechanics of Advanced Materials and Structures pp. 1–11 (2020). DOI 10.1080/15376494.2020.1712627

[23] Challis, V.J.: A discrete level-set topology optimization code written in Matlab. Structural and Multidisciplinary Optimization **41**(3), 453–464 (2010). DOI 10.1007/s00158-009-0430-0

[24] De Ruiter, M., van Keulen, F.: Topology optimization: approaching the material distribution problem using a topological function description. In: International conference on engineering computational technology (Leuven, 6-8 September 2000), pp. 111–119 (2000)

[25] De Ruiter, M.J., van Keulen, F.: Topology optimization using a topology description function. Structural and Multidisciplinary Optimization **26**(6), 406–416 (2004). DOI 10.1007/s00158-003-0375-7

[26] dHondt, G., Wittig, K.: CalculiX Users Guide. MTU (2016)

[27] Duan, S., Tao, Y., Han, X., Yang, X., Hou, S., Hu, Z.: Investigation on structure optimization of crashworthiness of fiber reinforced polymers materials. Composites Part B: Engineering **60**, 471–478 (2014). DOI 10.1016/j.compositesb.2013.12.062

[28] Duddeck, F., Hunkeler, S., Lozano, P., Wehrle, E., Zeng, D.: Topology optimization for crashworthiness of thin-walled structures under axial impact using hybrid cellular automata. Structural and Multidisciplinary Optimization **54**(3), 415–428 (2016). DOI 10.1007/s00158-016-1445-y

[29] Duddeck, F., Zimmer, H.: New achievements on implicit parameterization techniques for combined shape and topology optimization for crashworthiness based on SFE CONCEPT. In: Proc ICRASH Conf, Milano, Italy (2012)

[30] Duysinx, P., Bendsøe, M.P.: Topology optimization of continuum structures with local stress constraints. International journal for numerical methods in engineering **43**(8), 1453–1478 (1998). DOI 10.1002/(sici)1097-0207(19981230)43:8<1453::aid-nme480>3.0.co;2-2

[31] Eschenauer, H.A., Kobelev, V.V., Schumacher, A.: Bubble method for topology and shape optimization of structures. Structural Optimization **8**(1), 42–51 (1994). DOI 10.1007/BF01742933

[32] Fang, J., Sun, G., Qiu, N., Kim, N.H., Li, Q.: On design optimization for structural crashworthiness and its state of the art. Structural and Multidisciplinary Optimization **55**(3), 1091–1119 (2016). DOI 10.1007/s00158-016-1579-y

[33] Farley, G.L.: Energy Absorption of Composite Materials. Journal of Composite Materials **17**(3), 267–279 (1983). DOI 10.1177/002199838301700307

[34] Fender, J., Duddeck, F., Zimmermann, M.: On the calibration of simplified vehicle crash models. Structural and Multidisciplinary Optimization **49**(3), 455–469 (2014). DOI 10.1007/s00158-013-0977-7

[35] Fontana, M., Araujo, A., Madeira, J.: Optimization of a thin-walled composite crash absorber. Thin-Walled Structures **155**, 106,826 (2020). DOI 10.1016/j.tws.2020.106826

[36] Forrester, A.I.J., Sóbester, A., Keane, A.J.: Engineering Design via Surrogate Modelling. Wiley (2008). DOI 10.1002/9780470770801

[37] Forsberg, J., Nilsson, L.: Evaluation of response surface methodologies used in crashworthiness optimization. International Journal of Impact Engineering **32**(5), 759–777 (2006). DOI 10.1016/j.ijimpeng.2005.01.007

[38] Graff, L.: A stochastic algorithm for the identification of solution spaces in high-dimensional design spaces. Ph.D. thesis, Universität Basel, Basel, Switzerland (2013)

[39] Graff, L.S., Harbrecht, H., Zimmermann, M.: On the computation of solution spaces for robust design and sensitivity analysis. Preprint SPP1253-138, DFG Priority Program 1253, University of Erlangen, Erlangen, Germany (November) (2012)

[40] Gu, L., Yang, R., Tho, C., Makowskit, M., Faruquet, O., Li, Y.: Optimisation and robustness for crashworthiness of side impact. International Journal of Vehicle Design **26**(4), 348 (2001). DOI 10.1504/ijvd.2001.005210

[41] Haftka, R., Gürdal, Z.: Elements of Structural Optimization. Solid Mechanics and Its Applications. Springer Netherlands (2012)

[42] Hahn, H.T., Tsai, S.W.: Introduction to composite materials. CRC Press (1980)

[43] Han, J., Yamazaki, K.: Crashworthiness optimisation of S-shape square tubes. International Journal of Vehicle Design **31**(1), 72 (2003). DOI 10.1504/IJVD.2003.002048

[44] Hashin, Z.: Fatigue Failure Criteria for Unidirectional Fiber Composites. Journal of Applied Mechanics **48**(June 1980), 846 (1981). DOI 10.1115/1.3157744

[45] Hesse, S.H., Leidinger, L.F., Kremheller, J., Lukaszewicz, D., Duddeck, F.: Shape optimization with the level-set-method using local volume constraints. Structural and Multidisciplinary Optimization **57**(1), 115–130 (2017). DOI 10.1007/s00158-017-1741-1

[46] Hesse, S.H., Lukaszewicz, D.H.J.A., Duddeck, F.: A method to reduce design complexity of automotive composite structures with respect to crashworthiness. Composite Structures **129**, 236–249 (2015). DOI 10.1016/j.compstruct.2015.02.086

[47] Homma, T., Saltelli, A.: Importance measures in global sensitivity analysis of nonlinear models. Reliability Engineering & System Safety **52**(1), 1–17 (1996). DOI 10.1016/0951-8320(96)00002-6

[48] Hou, S., Han, X., Sun, G., Long, S., Li, W., Yang, X., Li, Q.: Multiobjective optimization for tapered circular tubes. Thin-Walled Structures **49**(7), 855–863 (2011). DOI 10.1016/j.tws.2011.02.010

[49] Hull, D.: A unified approach to progressive crushing of fibre-reinforced composite tubes. Composites Science and Technology **40**(4), 377–421 (1991). DOI 10.1016/0266-3538(91)90031-j

[50] Hunkeler, S.: Topology optimisation in crashworthiness design via hybrid cellular automata for thin walled structures. Ph.D. thesis, Queen Mary University of London, London, UK (2013)

[51] IJsselmuiden, S.: Optimal Design of Variable Stiffness Composite Structures Using Lamination Parameters. Ph.D. thesis, Technical University of Delft, Delft, The Netherlands (2011)

[52] Israr, H., Rivallant, S., Zeng, H., Barrau, J.: Finite element modelling of CFRP plates under crushing. In: ICCM 18-18th International Conference on Composite Materials, Jeju Island, Korea, 21-26 August (2011)

[53] Jacob, G.C., Fellers, J.F., Simunovic, S., Starbuck, J.M.: Energy absorption in polymer composites for automotive crashworthiness. Journal of composite materials **36**(7), 813–850 (2002). DOI 10.1106/002199802023164

[54] James, K.A., Lee, E., Martins, J.R.R.A.: Stress-based topology optimization using an isoparametric level set method. Finite Elements in Analysis and Design **58**, 20–30 (2012). DOI 10.1016/j.finel.2012.03.012

[55] Jiang, Y., Tay, T.E., Chen, L., Sun, X.S.: An edge-based smoothed XFEM for fracture in composite materials. International Journal of Fracture **179**(1-2), 179–199 (2013). DOI 10.1007/s10704-012-9786-z

[56] Johnson, A.F.: Modelling fabric reinforced composites under impact loads. Composites - Part A: Applied Science and Manufacturing **32**(9), 1197–1206 (2001). DOI 10.1016/S1359-835X(00)00186-X

[57] Johnson, A.F., David, M.: Failure mechanisms in energy-absorbing composite structures. Philosophical Magazine **90**(31-32), 4245–4261 (2010). DOI 10.1080/14786435.2010.497471

[58] Kang, B.S., Choi, W.S., Park, G.J.: Structural optimization under equivalent static loads transformed from dynamic loads based on displacement. Computers and Structures **79**, 145–154 (2001). DOI 10.1016/S0045-7949(00)00127-9

[59] Kang, B.S., Park, G.J., Arora, J.S.: A review of optimization of structures subjected to transient loads. Structural and Multidisciplinary Optimization **31**(2), 81–95 (2006). DOI 10.1007/s00158-005-0575-4

[60] Kawamoto, A., Matsumori, T., Yamasaki, S., Nomura, T., Kondoh, T., Nishiwaki, S.: Heaviside projection based topology optimization by a PDE-filtered scalar function. Structural and Multidisciplinary Optimization **44**(1), 19–24 (2011). DOI 10.1007/s00158-010-0562-2

[61] Kim, Y.I., Park, G.J.: Nonlinear dynamic response structural optimization using equivalent static loads. Computer Methods in Applied Mechanics and Engineering **199**(9-12), 660–676 (2010). DOI 10.1016/j.cma.2009.10.014

[62] Kohavi, R.: A Study of Cross-Validation and Bootstrap for Accuracy Estimation and Model Selection. International Joint Conference on Artificial Intelligence **14**, 1137–1143 (1995). DOI 10.1067/mod.2000.109031

[63] Kreissl, S., Maute, K.: Levelset based fluid topology optimization using the extended finite element method. Structural and Multidisciplinary Optimization **46**(3), 311–326 (2012). DOI 10.1007/s00158-012-0782-8

[64] Krueger, R.: The Virtual Crack Closure Technique: History, Approach and Applications. Applied Mechanics Reviews **57**(2), 109 (2002). DOI 10.1115/1.1595677

[65] Kurtaran, H., Eskandarian, A., Marzougui, D., Bedewi, N.E.: Crashworthiness design optimization using successive response surface approximations. Computational Mechanics **29**(4-5), 409–421 (2002). DOI 10.1007/s00466-002-0351-x

[66] Lanzi, L., Castelletti, L.M.L., Anghileri, M.: Multi-objective optimisation of composite absorber shape under crashworthiness requirements. Composite Structures **65**(3-4), 433–441 (2004). DOI 10.1016/j.compstruct.2003.12.005

[67] Le, C., Norato, J., Bruns, T., Ha, C., Tortorelli, D.: Stress-based topology optimization for continua. Structural and Multidisciplinary Optimization **41**(4), 605–620 (2010). DOI 10.1007/s00158-009-0440-y

[68] Lescheticky, J., Barnes, G., Schrank, M.: System Level Design Simulation to Predict Passive Safety Performance for CFRP Automotive Structures. SAE Technical Paper (2013). DOI 10.4271/2013-01-0663

[69] Lukaszewicz, D.H.J.A.: Automotive Composite Structures for Crashworthiness. In: Advanced Composite Materials for Automotive Applications: Structural Integrity and Crashworthiness, pp. 99–127 (2014)

[70] Luo, Z., Wang, M.Y., Wang, S., Wei, P.: A level set-based parameterization method for structural shape and topology optimization. International Journal for Numerical Methods in Engineering **76**(1), 1–26 (2008). DOI 10.1002/nme.2092

[71] Mamalis, A., Robinson, M., Manolakos, D., Demosthenous, G., Ioannidis, M., Carruthers, J.: Crashworthy capability of composite material structures. Composite Structures **37**(2), 109–134 (1997). DOI 10.1016/S0263-8223(97)80005-0

[72] Mayer, R.R., Kikuchi, N., Scott, R.A.: Application of Topological Optimization Techniques to Structural Crashworthiness. International Journal for Numerical Methods in Engineering **39**(8), 1383–1403 (1996). DOI 10.1002/(SICI)1097-0207(19960430)39:8<1383::AID-NME909>3.0.CO;2-3

[73] Mcgregor, C., Zobeiry, N., Vaziri, R., Poursartip, A.: A constitutive model for progressive compressive failure of composites. Journal of Composite Materials **42**(25), 2687–2716 (2008). DOI 10.1177/0021998308096330

[74] van der Meer, F.P., Sluys, L.J., Hallett, S.R., Wisnom, M.R.: Computational modeling of complex failure mechanisms in laminates. Journal of Composite Materials **46**(5), 603–623 (2012). DOI 10.1177/0021998311410473

[75] Miki, M.: Material design of composite laminates with required in-plane elastic properties. Progress in Science of Engineering Composites **ICCM-IV**, 1725–1731 (1982)

[76] Nixon, S., Barnes, G.: Effective crushing simulation for composite structures. In: ICCM-17, Edinburgh, UK (2009)

[77] Ortmann, C., Schumacher, A.: Graph and heuristic based topology optimization of crash loaded structures. Structural and Multidisciplinary Optimization **47**(6), 839–854 (2013). DOI 10.1007/s00158-012-0872-7

[78] Osher, S., Sethian, J.A.: Fronts Propagating with Curvature-Dependent Speed: Algorithms Based on Hamilton-Jacobi Formulations. Journal of Computational Physics **79**, 12–49 (1988). DOI 10.1016/0021-9991(88)90002-2

[79] Osher, S.J., Santosa, F.: Level Set Methods for Optimization Problems Involving Geometry and Constraints: I. Frequencies of a Two-Density Inhomogeneous Drum. Journal of Computational Physics **171**(1), 272–288 (2001). DOI 10.1006/jcph.2001.6789

[80] Otomori, M., Yamada, T., Izui, K., Nishiwaki, S.: Topology Optimization Based on the Level Set Method Using Mathematical Programming. Transactions of the Japan society of mechanical engineers series C **77**, 4001–4014 (2011). DOI 10.1299/kikaic.77.4001

[81] Otomori, M., Yamada, T., Izui, K., Nishiwaki, S.: Matlab code for a level set-based topology optimization method using a reaction diffusion equation. Structural and Multidisciplinary Optimization **51**(5), 1159–1172 (2014). DOI 10.1007/s00158-014-1190-z

[82] Palanivelu, S., Van Paepegem, W., Degrieck, J., Van Ackeren, J., Kakogiannis, D., Wastiels, J., Van Hemelrijck, D., Vantomme, J.: Parametric study of crushing parameters and failure patterns of pultruded composite tubes using cohesive elements and seam: Part II - Multiple delaminations and initial geometric imperfections. Polym. Test. **29**(7), 803–814 (2010). DOI 10.1016/j.polymertesting.2010.07.005

[83] Paris, J., Navarrina, F., Colominas, I., Casteleiro, M.: Topology optimization of continuum structures with local and global stress constraints. Structural and Multidisciplinary Optimization **39**(4), 419–437 (2009). DOI 10.1007/s00158-008-0336-2

[84] Patel, N.M.: Crashworthiness Design using Topology Optimization. Ph.D. thesis, Notre Dame University, Notre Dame, Indiana, USA (2007)

[85] Patel, N.M., Kang, B.S., Renaud, J.E., Tovar, A.: Crashworthiness design using topology optimization. Journal of Mechanical Design **131**(6) (2009). DOI 10.1115/1.3116256

[86] Pedersen, C.: Topology optimization design of crushed 2d-frames for desired energy absorption history. Structural and Multidisciplinary Optimization **25**(5-6), 368–382 (2003). DOI 10.1007/s00158-003-0282-y

[87] Pedersen, C.B.: Crashworthiness design of transient frame structures using topology optimization. Computer Methods in Applied Mechanics and Engineering **193**(6-8), 653–678 (2004). DOI 10.1016/j.cma.2003.11.001

[88] Pedersen, C.B.W.: Topology optimization for crashworthiness of frame structures. International Journal of Crashworthiness **8**(1), 29–39 (2003). DOI 10.1533/ijcr.2003.0218

[89] Puck, A., Schürmann, H.: Failure analysis of FRP laminates by means of physically based phenomenological models. Composites Science and Technology **62**(96), 1633–1662 (2002). DOI 10.1016/S0266-3538(01)00208-1

[90] Raponi, E., Bujny, M., Olhofer, M., Aulig, N., Boria, S., Duddeck, F.: Kriging-assisted topology optimization of crash structures. Computer Methods in Applied Mechanics and Engineering **348**, 730–752 (2019). DOI 10.1016/j.cma.2019.02.002

[91] Reuter, U., Liebscher, M.: Global sensitivity analysis in view of nonlinear structural behavior. In: LS-Dyna Users Conference, vol. 56, pp. 903–915 (2008). DOI 10.1016/0045-7949(94)00580-V

[92] Ryu, Y., Haririan, M., Wu, C., Arora, J.: Structural design sensitivity analysis of nonlinear response. Computers & Structures **21**(1), 245 – 255 (1985). DOI 10.1016/0045-7949(85)90247-0

[93] Schumacher, A.: Topologieoptimierung von Bauteilstrukturen unter Verwendung von Lochpositionierungskriterien. Ph.D. thesis, Universität-Gesamthochschule-Siegen, Siegen, Germany (1996)

[94] Sethian, J.A., Wiegmann, A.: Structural Boundary Design via Level Set and Immersed Interface Methods. Journal of Computational Physics **163**(2), 489–528 (2000). DOI 10.1006/jcph.2000.6581

[95] SFE GmbH: SFE CONCEPT Ver 4.4.0.6, Reference Manual. Berlin, Germany (2014)

[96] Sigmund, O.: A 99 line topology optimization code written in MATLAB. Structural and Multidisciplinary Optimization **21**(2), 120–127 (2001). DOI 10.1007/s001580050176

[97] Sobol, I.M.: Global sensitivity indices for nonlinear mathematical models and their Monte Carlo estimates. Mathematics and Computers in Simulation **55**(1-3), 271–280 (2001). DOI 10.1016/S0378-4754(00)00270-6

[98] Stander, N., Burger, M., Zhu, X., Maker, B.: Springback Compensation in Sheet Metal Forming Using a Successive Response Surface Method. In: 9th AIAA/ISSMO Symposium on Multidisciplinary Analysis and Optimization, pp. 1–10. American Institute of Aeronautics and Astronautics, Reston, Virginia, USA (2002). DOI 10.2514/6.2002-5539

[99] Stocki, R., Tauzowski, P., Knabel, J.: Reliability analysis of a crashed thin-walled s-rail accounting for random spot weld failures. International Journal of Crashworthiness **13**(6), 693–706 (2008). DOI 10.1080/13588260802055213

[100] Storn, R., Price, K.: Minimizing the real functions of the ICEC'96 contest by differential evolution. In: Proceedings of IEEE International Conference on Evolutionary Computation. IEEE (1996). DOI 10.1109/icec.1996.542711

[101] Storn, R., Price, K.: Differential evolution - a simple and efficient heuristic for global optimization over continuous spaces. Journal of global optimization **11**(4), 341–359 (1997). DOI 10.1023/A:1008202821328

[102] Sudret, B.: Global sensitivity analysis using polynomial chaos expansions. Reliability Engineering & System Safety **93**(7), 964–979 (2008). DOI 10.1016/j.ress.2007.04.002

[103] Távara, L., Mantiĉ, V., Graciani, E., Pars, F.: BEM analysis of crack onset and propagation along fiber-matrix interface under transverse tension using a linear elastic-brittle interface model. Engineering Analysis with Boundary Elements **35**(2), 207–222 (2011). DOI 10.1016/j.enganabound.2010.08.006

[104] Tsai, S.W., Pagano, N.J.: Invariant properties of composite materials. Tech. rep., Air force materials lab Writh-Patterson AFB OH Wright-Patterson AFB (1968)

[105] Tsai, S.W., Wu, E.M.: A General Theory of Strength for Anisotropic Materials. Journal of Composite Materials **5**(1), 58–80 (1971). DOI 10.1177/002199837100500106

[106] van Dijk, N., Langelaar, M., van Keulen, F.: Explicit level-set-based topology optimization using an exact Heaviside function and consistent sensitivity analysis. International Journal for Numerical Methods in Engineering **91**(1), 67–97 (2012). DOI 10.1002/nme.4258

[107] Van Dijk, N.P., Maute, K., Langelaar, M., Van Keulen, F.: Level-set methods for structural topology optimization: A review. Structural and Multidisciplinary Optimization **48**(3), 437–472 (2013). DOI 10.1007/s00158-013-0912-y

[108] Van Miegroet, L., Duysinx, P.: Stress concentration minimization of 2D filets using X-FEM and level set description. Structural and Multidisciplinary Optimization **33**(4-5), 425–438 (2007). DOI 10.1007/s00158-006-0091-1

[109] Wang, M.Y., Wang, X., Guo, D.: A level set method for structural topology optimization. Computer Methods in Applied Mechanics and Engineering **192**(1-2), 227–246 (2003). DOI 10.1016/S0045-7825(02)00559-5

[110] Wang, S., Wang, M.Y.: Radial basis functions and level set method for structural topology optimization. International Journal for Numerical Methods in Engineering **65**(12), 2060–2090 (2006). DOI 10.1002/nme.1536

[111] Wei, P., Wang, M.Y., Xing, X.: A study on X-FEM in continuum structural optimization using a level set model. Computer-Aided Design **42**(8), 708–719 (2010). DOI 10.1016/j.cad.2009.12.001

[112] Wen, J., Zhao, D., Zhang, C.: An overview of electricity powered vehicles: Lithium-ion battery energy storage density and energy conversion efficiency. Renewable Energy **162**, 1629–1648 (2020). DOI 10.1016/j.renene.2020.09.055

[113] Wu, H., Xin, Y.: Optimal design of the S-Rail for crashworthiness analysis. In: Proceedings of the 2009 International Joint Conference on Computational Sciences and Optimization, CSO 2009, vol. 2, pp. 735–738. IEEE (2009). DOI 10.1109/CSO.2009.80

[114] Yamasaki, S., Nishiwaki, S., Yamada, T., Izui, K., Yoshimura, M.: A structural optimization method based on the level set method using a new geometry-based re-initialization scheme. International Journal for Numerical Methods in Engineering **83**(12), 1580–1624 (2010). DOI 10.1002/nme.2874

[115] Yamasaki, S., Nomura, T., Kawamoto, A., Sato, K., Nishiwaki, S.: A level set-based topology optimization method targeting metallic waveguide design problems. International Journal for Numerical Methods in Engineering **87**(9), 844–868 (2011). DOI 10.1002/nme.3135

[116] Yang, Q., Cox, B.: Cohesive models for damage evolution in laminated composites. International Journal of Fracture **133**(2), 107–137 (2005). DOI 10.1007/s10704-005-4729-6

[117] Yang, R.J., Chen, C.J.: Stress-based topology optimization. Structural and Multidisciplinary Optimization **12**(2), 98–105 (1996). DOI 10.1007/bf01196941

[118] Yang, R.J., Gu, L., Soto, C., Li, G., Tyan, T.: Developments and applications of structural optimization and robustness methods in vehicle impacts. In: Transportation and Environment. ASMEDC (2004). DOI 10.1115/imece2004-61977

[119] Yousaf, M.S., Bujny, M., Zurbrugg, N., Detwiler, D., Duddeck, F.: Similarity control in topology optimization under static and crash loading scenarios. Engineering Optimization pp. 1–16 (2020). DOI 10.1080/0305215x.2020.1806257

[120] Zarei, H., Kröger, M., Albertsen, H.: An experimental and numerical crashworthiness investigation of thermoplastic composite crash boxes. Composite Structures **85**(3), 245–257 (2008). DOI 10.1016/j.compstruct.2007.10.028

[121] Zeng, D.: Enhanced hybrid cellular automata method for crashworthiness topology optimization of thin-walled structures. Ph.D. thesis, Technische Universität München, Munich, Germany (2019)

[122] Zeng, D., Duddeck, F.: Improved hybrid cellular automata for crashworthiness optimization of thin-walled structures. Structural and Multidisciplinary Optimization **56**(1), 101–115 (2017). DOI 10.1007/s00158-017-1650-3